Technical University of Denmark

DTU

Processability, Microstruc ture and Impact Properties of Injectionmoulded Poly(oxymethylene)

Laursen, Jens Lolle; Vigild, Martin Etchells; Christoffersen, Lasse Wengel; Brøndsted, Povl; Horsewell, Andy; Sivebæk, Ion Marius

DTU Library
Technical Information Center of Denmark

PROCESSABILITY, MICROSTRUCTURE AND IMPACT PROPERTIES OF INJECTIONMOULDED POLY(OXYMETHYLENE)

$$f(x+\Delta x)=\sum_{i=0}^{\infty}\frac{(\Delta x)^i}{i!}f^{(i)}(x)$$

Jens Lolle Laursen
Ph.D. Thesis
2009

DTU Chemical Engineering
Department of Chemical and Biochemical Engineering

PROCESSABILITY, MICROSTRUCTURE AND IMPACT PROPERTIES OF INJECTION MOULDED POLY(OXYMETHYLENE)

-

EXPERIMENTAL INVESTIGATIONS IN AN INDUSTRIAL CONTEXT

Novo Nordisk A/S
&
Danish Polymer Center,
Technical University of Denmark

Jens Lolle Laursen

Supervisors, DTU:
Martin E. Vigild (DPC)
Povl Brøndsted (Risø)
Andy Horsewell (MEK)

Supervisors, Novo Nordisk:
Lasse W. Christoffersen
Ion M. Sivebæk
Mogens Papsøe

PREFACE

The present thesis constitutes the written documentation of the work I have carried out during my Industrial PhD project in the department of Materials & Device Characterisation at Novo Nordisk A/S (NNAS). Over the three-year course of the project it evolved from a loosely-defined project description, through a series of exploratory studies shedding light on different potential aspects of my investigations, into the final focus of the thesis at hand: Process-dependence of impact behaviour of injection moulded poly(oxymethylene). This final focus is a result of my realisation of the complexity of experimental characterisation within this field, but also of the importance of such knowledge and understanding within the department in NNAS.

Most of my project has been carried out at the research facilities at NNAS. The largest part of the project has been the establishment and qualification of the experimental facilities needed for my investigations. In large, this has consisted of the procurement of an injection moulding setup and an impact testing setup. Techniques for the characterisation of microstructure and morphology of injection moulded polymers have also been a major practical task of the project, though this part primarily has been to learn and utilise methods well-described in the literature. Moreover, for this part NNAS had already a strong expertise, and this work has therefore consisted of both induction training in the department, further gathering of knowledge within the techniques and the actual employment on my model system.

During the first months of my project I had the fortunate opportunity of visiting Prof. Krystyn Van Vliet of the Laboratory for Material Chemomechanics at the Massachusetts Institute of Technology, USA. A subsequent three-month stay in her group allowed me to get a basic training within nanoindentation and to explore the opportunities of this technique for local mechanical characterisation of my injection moulded test specimens. I am indebted to Prof. Van Vliet for giving me this opportunity for a fruitful stay abroad. I direct special thanks to PhD student in the Van Vliet group Zeynep Ilke Kalcioglu for our collaboration on nanoindentation of polymers and for her immense helpfulness during my visit and the final part of my project.

I would like to thank all my colleagues at Novo Nordisk A/S for all their social and academic input, and my six supervisors for their invaluable critics and guidance throughout the project. I have particularly had great benefit of my two main supervisors, Principal Scientist Lasse W. Christoffersen and Prof. Martin E. Vigild, who I have learned immensely from. I acknowledge funding from the Danish Ministry of Science, Technology and Innovation, VTU, and the department of Corporate Research Affairs at NNAS. Moreover, I owe special thanks to my manager at NNAS, Director of Materials & Device Characterisation Niels Bjerrum Thomsen, PhD, for his kind engagement in my project and my further education. Special thanks are also due to laboratory technician Charlotte Anker for her help with various experimental characterisations, which has been beyond reasonable limits.

In gratitude of her endless support and understanding throughout the great personal challenge this PhD work has been, I dedicate this thesis to my fiancée, Sisse.

Kgs. Lyngby, January 2009

Jens Lolle Laursen

CONTENTS

SYNOPSIS

The present project deals with the process dependence of impact properties of injection moulded poly(oxymethylene). The aim has been to provide Device R&D in Novo Nordisk A/S (NNAS) with methods and means for characterisation of such behaviour, and to use these to elucidate the underlying mechanisms through a model system. An injection mould for procuring test specimens were made and materials were moulded under varying process conditions. The microstructure and morphology of the mouldings were investigated and characteristic features were coupled with the processing conditions used. Impact properties were determined based on two fundamentally different approaches. Nanoindentation (depth-sensing indentation) was used to probe the mechanical properties of the outermost layers of the mouldings. The properties and extent of these layers were compared to the impact properties, in an attempt to explain the mechanisms behind the observed process dependence and anisotropy of these measures. Process dependent effects of the admixture of two tribological additives have also been investigated, both in terms of coefficient of friction and impact properties. The effect of such additives on the mechanical properties of the base material was the offset for this project.

The interrelation between processing conditions and mechanical properties of plastics have been intensively investigated by many research groups. Studies of microstructure and morphology have been widely used to explain the cause of process dependence in properties. When it comes to the behaviour of injection moulded plastics under impact loading, however, the available literature is rather sparse. The majority of reported studies in the field of impact and fracture mechanics of polymers take offset in relatively thick compression mouldings. Studies of the material under such conditions are used to yield conservative estimates of fracture performance. Several recent studies have indicated, however, that testing on specimens of realistic wall-thickness is needed for evaluation of process dependence and anisotropy of thin-walled injection mouldings. Such studies for a copolymer poly(oxymethylene) form the basis of this project.

An essential part of the project has been to develop a test specimen geometry and an injection mould, which provides for tests on material processed under conditions similar to large-scale production in Novo Nordisk A/S (NNAS). A new injection mould was made and 1.5 mm thick test plates with a unidirectional filling pattern have been used to investigate process dependence of both frictional and mechanical properties.

The standard fracture mechanical approach to impact testing is based on measurements of pre-cracked specimens. An ideally sharp pre-crack provides a worst case in terms of stress state at the site of fracture initiation. The cutting of a pre-crack, however, penetrates the outer microstructural layers of the moulding and this method may therefore not provide an accurate assessment of the influence of these layers. In addition to impact testing using pre-cracked specimens tests have also been made in this project on specimens containing a moulded-in notch as stress raiser. Comparison of data from the two approaches reveals a potential for different conclusions regarding process dependence and anisotropy. This latter approach is believed to better resemble the conditions under which a real component would fail and therefore comes out as the preferred method for these kinds of investigations.

Characterisation of the microstructure and morphology of the injection mouldings supports that the outer microstructural layers constitute the main link between process conditions and impact properties. This conclusion is further strengthened by the nanoindentation studies.

1. INTRODUCTION AND BACKGROUND

The present project took offset in a whish from Novo Nordisk A/S (NNAS) to gain a further understanding of how additives and processing can affect the mechanical properties of plastics. The additives in question were of a kind used to reduce friction between plastic components sliding against each other ('tribological additives'). Their potential use for plastic components in devices from NNAS had come about by the work of tribologist Ion M. Sivebæk, who during his post.doc in the department had qualified their tribological performance under relevant conditions. His work had indicated a great potential within development of grades tailored specifically for the use in NNAS, but had also shown that the nature and desired concentrations of some of the additives could lead to marked reductions in the mechanical integrity of the base polymer. It quickly became evident that a qualification of new grades developed in-house would require a thorough understanding of the interaction between the additives, the injection moulding processing conditions and the mechanical behaviour of the moulded material. This project was undertaken in attempt to enhance the qualifications of NNAS for this task, which may be seen as the long-scope aim of the project. On the shorter track, i.e. in the duration of my PhD project, the aim has been to procure and qualify an experimental setup for the required investigations, based on literature studies and participation in conferences and seminars within this field of applied mechanical/polymer research. This main part of the project may be divided into the following elements: Injection moulding, tribological testing, microstructure and morphology characterisation, fracture mechanical characterisation and micro/nano-scale mechanical characterisation. Their interrelation with respect to this project and the practical work flow is illustrated in Figure 1.1. The part to the right of the gray vertical line represents the primary work areas of this project. The part to the left represents the context of tribological testing, which was already well-established in NNAS at project start-up. Tribological testing of the moulded material according to the internal protocol of NNAS has also been performed in this project, but primarily with the aim of qualifying the extra accessories needed for such measurements on the procured test blanks. Procurement of the injection mould for making test blanks ended up constituting a disproportionably large workload, but this basis was found essential for the relevance of further investigations within the process dependence of mechanical properties. Among the other three areas of experimental investigation, the impact testing has been of main focus in this project. Characterisation of the microstructure and morphology of the moulded specimens has been included to elucidate the underlying mechanisms behind the observed process dependence in impact properties. Mechanical characterisation by indentation was included as an exploratory investigation to further strengthen this link to the underlying mechanisms. In large, this outlines what will be treated in the rest of this thesis.

It may well be asked; why the choice of impact testing as a means of mechanical characterisation? There were several considerations behind that choice. First of all, it is reported in several references that the influence of the microstructure and morphology on the mechanical properties of injection moulded semi-crystalline polymers is increased at high strain rates [1-3]. Secondly, the risk of ductile failure can be evaluated through conventional methods with a tensile testing machine, which was already a well-established competency at NNAS when the project was commenced. The risk of brittle fracture of moulded components as promoted by impact loading was found of great importance to the Device R&D organisation, but procedures and testing facilities for such evaluation was not established, nor had this call of competency been directly addressed. Last but not least, had preceding investigations shown a high increase in risk of processing induced flaws in some injection moulded plastics with tribological additives; a material deficiency known to potentially cause brittle fracture under impact loading.
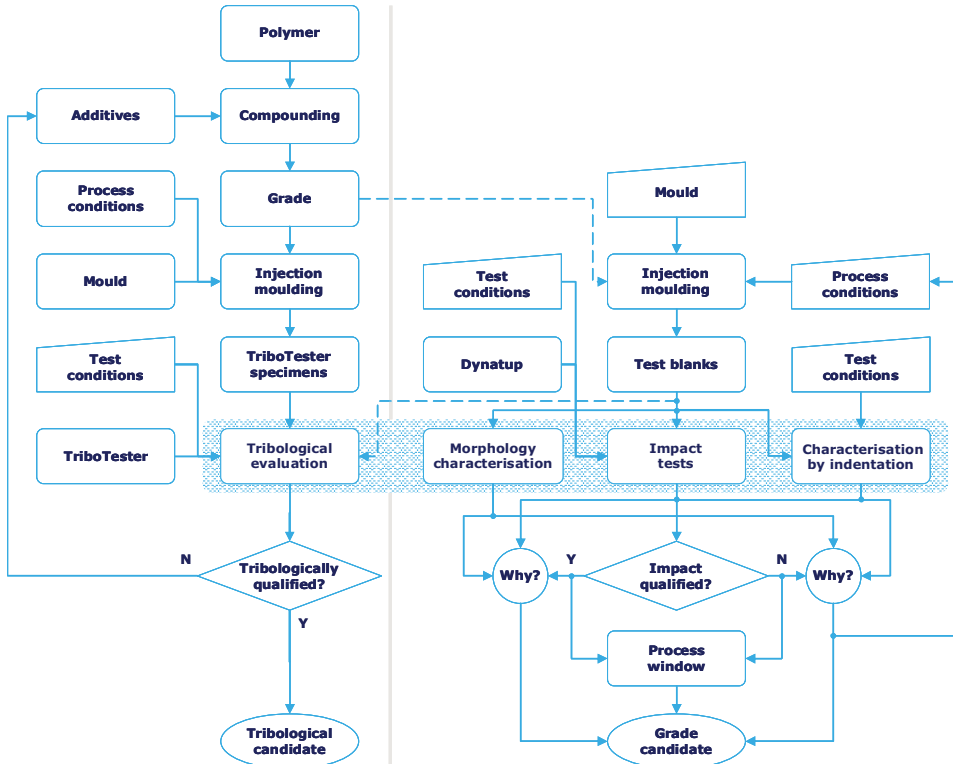
Figure 1.1: Project framework. The TriboTester and Dynatup are the apparatus at NNAS for friction and impact testing, respectively.

In addition to the mechanical properties of injection moulded components, account must of course be taken of the dimensional stability and any cosmetic requirements there may be to the part. Evaluation of these issues lie beyond the scope of this project, yet have they been considered during the choice of injection moulding setup, and the procured solution is readily applicable for use in such studies as well.

1.1. Readers guide

The main experimental investigations in this project have been divided into two separate studies. The second study was commenced after finishing of the first and could therefore be based on the findings and conclusions from this study. In this thesis the two studies will be dealt with in parallel, though the description in chapters that are relevant to both studies will follow the actual chronology of the conducted work.

The nomenclature used throughout this thesis has taken offset in the ISO 17281 standard on which most of the impact testing work has been based. Nomenclature in the nanoindentation chapter (6), however, has been based on the common use of symbols within this particular field [4]. Because of overlap in the common definition of symbols within fracture mechanics and indentation, some

quantities are referred to by more than one symbol ($F = P$ = force or load) and other are referred to by symbols not taken from these references (e.g. b as specimen thickness). The symbols are defined when they are used the first time and are furthermore given in chapter 9.

1.1.1. Introduction to the Additives & Impact Study

The aim of the first study was to address the question of process dependence of POM with tribological additives, both in terms of friction and impact properties. The following approach was used in this endeavour:

a) Compounding of base material with relevant tribological additives
b) Injection moulding of modified grades into a relevant testing geometry using various processing conditions
c) Tribological testing for evaluation of frictional properties
d) Impact testing for evaluation of a relevant measure of resistance towards brittle fracture

The techniques used and results from items b), c) and d) are treated in chapters 2, 3 and 5, respectively. The results of this study have been presented at the ANTEC 2008 conference[A] in Milwaukee, USA, and at the NordTrib 2008 conference in Tampere, Finland. The proceeding for the latter has been further reworked into a manuscript that has been accepted for publication in the ISI journal *Wear* (Elsevier).

1.1.2. Introduction to the Impact & Indentation Study

The aim of the second study was to investigate the cause of the process dependence of impact properties of POM without additives. The following approaches were used in this endeavour:

a) Injection moulding of POM grade into a relevant testing geometry using various processing conditions
b) Characterisation of microstructure and morphology
c) Impact testing for evaluation of a relevant measure of resistance towards brittle fracture
d) Micromechanical characterisation of outer microstructural layers

The techniques used and results from items a), b), c) and d) are treated in chapters 2, 4, 5 and 6, respectively. The results of this study remains to be reworked into a manuscript and has therefore not yet been submitted for publication.

1.2. Novo Nordisk A/S

Novo Nordisk A/S (NNAS) is the world leader in diabetes care. Besides pharmaceuticals, the product portfolio includes also advanced products within the area of drug delivery systems. The largest class of devices in this area is prefilled pen-devices, which are comprised primarily of injection moulded plastic components. The department I have been affiliated with during my PhD project, Materials & Device Characterisation, are responsible for providing material-related competencies throughout the Device R&D organisation in the company.

[A] ANTEC is the annual technical conference of the Society of Plastics Engineers (SPE).

2.   INJECTION MOULDING OF TEST BLANKS

It is well known that the properties of plastics in general depend on how they have been processed. Even within the boundaries of the injection moulding process a wide range of properties may result from different settings of the machine controls. The many different objectives against which a process may be optimised leads to potential shortcomings in some properties, while other are sought improved. In a production setup, for instance, the general agenda is increased productivity while still meeting the documented part requirements. A thorough understanding of the interrelation between processing conditions and material deficiencies is therefore required as countermeasure in order to obtain a balanced optimisation of the process. Such will provide mouldings with little probability of premature failure at the right production cost, and is therefore of high relevance for any company injection moulding plastics. Within the area of drug delivery devices this is even more the case, since failure of moulded components may have severe consequences for the patient.

The required processing-related material knowledge may be acquired through experimental studies on model systems. Through the use of simplified test geometries more generic information may be obtained, providing for utilisation across various components and materials.

2.1.   The injection moulding process

The injection moulding process is well described in the literature and will not be thoroughly accounted for here. Instead the reader is referred to references like those of Whelan and Whelan & Goff [5;6]. The microstructure and morphology resulting from the injection mouldings of this project are described in chapter 4. The link to the process dependence of mechanical properties are dealt with in chapters 5-7.

2.2.   Injection mould for test blanks

An injection mould for making test blanks was procured as part of the project. The test blanks provide for test specimens for evaluation of processability, tribological and mechanical performance of injection moulded plastics. The following briefly describes the requirements imposed by each of these areas of characterisation.

2.2.1. Introductory considerations

Evaluation of processability may be seen as an evaluation of the process window by which the material can be moulded without the component suffering significant deterioration of properties. The benchmark in this regard may be a component moulded according to the recommendations of the material manufacturer. For injection moulded plastics this will often refer to the ISO mould conditions (ISO 294) found in many data sheets[A]. Further to the properties of the component, however, an evaluation of processability should also cover phenomena related to the moulding process itself. This may for instance be requirements imposed by the melt viscosity, the maximum allowable shear rate or the tendency to form mould deposits. Such aspects have also been considered in this project, but are not part of the reported work in this thesis.

It lies intrinsically in the elastic term processability that the evaluation easily becomes subjective and biased by both choice of moulding setup and testing setup. ISO (and similarly ASTM) seeks to

---

[A] ISO 294 describes the geometry and moulding of test specimens for property evaluation according to most other ISO standards for plastics. Axxiconn (The Netherlands) manufactures ISO moulds for such use under the name 'AIM'.

counteract this through standardisation of geometry and moulding conditions for test specimens. These conditions, which for POM are described in ISO 9988-2, makes it easy to produce test specimens of a high and consistent quality. This is good for the material manufacturer, since the costumer can verify for himself that the material performs as promised. The problem for the costumer is that when the material does not behave as expected, e.g. when POM unexpectedly fails in a brittle manner, it will often be because the idealised ISO moulding conditions were not met for the real moulding. Hence, the ISO moulding approach makes less sense when trying to link process-dependent material behaviour to the performance of actual components. In this case, offset should be taken in the expected use (or misuse) of the material rather than in conditions where the manufacturer vouches for the material behaviour. In other words, evaluating processability in this wide term, or any property potentially dependent on processing, shall best be done through a test specimen setup that mimics the setup used in production. In NNAS this is far from the cold runner-based ISO moulds of benign runner dimensions, and the idea of using such as basis for this project was therefore early discarded.

The use of numerical process simulation tools like Moldflow Plastics Insight (MPI, Moldflow Corporation) has greatly enhanced the possibility of evaluating process dependence of properties based on characteristic process conditions. Viana *et al.* describes processing indices which are meant to quantify the interrelation between the phenomena governing the process dependence [7-9]. Though such indices holds the potential of predictive modelling of the component behaviour, the current state of the art and the extent of this project have not allowed for such a fundamental approach. In simple geometries hand calculations will often suffice in providing e.g. the wall shear rate in a critical cross-section. The link to the moulding of real components will, however, often require numerical process simulations. With the tools for such at hand the link from component design, material and processing conditions to the performance of the component may be formed on the based of a suitable test specimen geometry. Figure 2.1 illustrates how a generic test specimen geometry may provide this link in conjunction with process simulation software. This idea has been the basis for the procurement of the test specimen mould in this project.
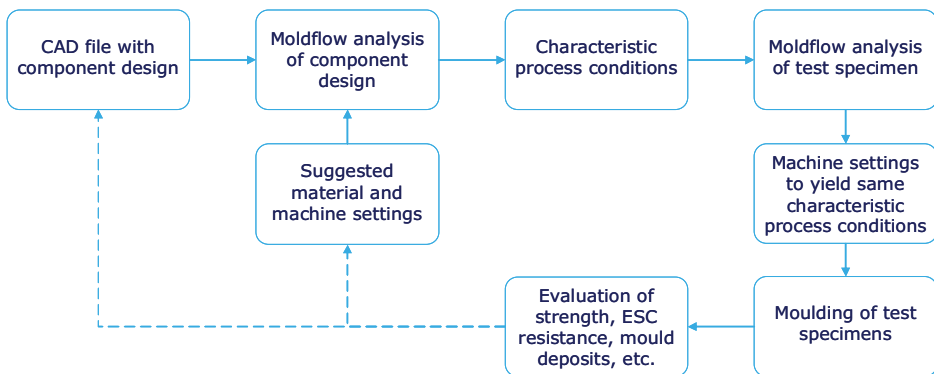
Figure 2.1: Example of the potential use of a test specimen mould in Device R&D.

The choice of test that the moulded material is evaluated against will of course be decisive for the resulting process window. For this project the two primary evaluation tests have been the aforementioned tribological testing and impact testing. The nanoindentation tests in this project

were not taken into consideration at this stage. A setup allowing for evaluation of both frictional and impact mechanical performance on the same specimens, which have been moulded under well-defined and relevant conditions, was seen as a prerequisite for a potential qualification of a new grade. Moreover, it was found to be a valuable tool for investigations into the underlying phenomena causing the process dependence of any of the properties related to frictional and mechanical behaviour. The test specimen mould seen as such also provides for e.g. more generic injection moulding optimisations, assessment of resistance towards environmental stress cracking (ESC) or general evaluations of mechanical properties. The potential use of the mould thus extends far beyond the agenda of this project itself, a point that is reflected in the chosen solutions treated below.

A tribology testing apparatus, called the TriboTester, had been developed at NNAS by Ruby, Herslund and Sivebæk prior to the commencement of the project [10]. The tester is made according to the ring-on-disc principle and could by small modifications be made to accommodate testing on any flat geometry as the disc-part of the friction pairing. The friction testing thus imposed little restriction to the choice of test blank geometry in the project.

A key consideration in the choice of test geometry was the possibility for evaluation of mechanical anisotropy. This advocated for a side-gated square plate geometry, rather than e.g. a centre-gated circular disc. A simple thin plate of unidirectional flow pattern would also be of great value for other characterisations of the kind mentioned above. A survey was made in the department regarding which tests a test plate of this kind would be of interest with respect to. This was done to ensure that this massive investment in a test specimen mould would fulfil as many potential needs as possible. The resulting list is shown in appendix 11.1. The development of a concept and design for a plate blank and mould to fulfil the identified desires in Device R&D was undertaken in cooperation with the chosen mould maker (Tecpart A/S, Denmark).

2.2.2. Concept and design of test blank and mould

A quadratic test plate of 60×60 mm^2 was decided on as basic geometry. A thickness of 1.5 mm was chosen as a compromise between the thickness being relevant to device components and suitable for mechanical testing in praxis. A thickness just below 1 mm is more common in components for injection devices, but limits the impact testing possibilities to tensile loading scenarios. The chosen 1.5 mm was deemed the lowest thickness not immediately restricting the experimental possibilities of the plate. Seven variations over this basic plate geometry was made to fulfil the aforementioned requirements for test specimens. All configurations are briefly described in appendix 11.1, but here only the two used for the studies of this thesis will be described.

The mould is modularly build as a mould base with interchangeable inserts; three inserts in each mould half. An overview image from the CAD model can be found in appendix 11.1. The hot runner system (Husky Injection Moulding Systems, Canada) is equipped with 1.5 mm needle-valve nozzles with pneumatic actuation. This is the standard solution used in large-scale production moulds at NNAS and thus constitutes a realistic runner system for the test specimen mould. Configuration 1 is the basis plate blank, where the cavity inserts in both mould halves are polished with diamond paste 7 μm[A]. Configuration 3 contains a moulded-in notch in both the end edge and one of the side edges. An example of this geometry can be seen in Figure 2.2. Specimens from this configuration are used in the Impact & Indentation Study.

[A] R_a and R_z values for the polished surfaces were measured to be 9 and 90 nm, respectively (ISO 4287).

The desired studies of anisotropy in properties required test specimens cut in both flow and transverse directions from moulded plate blanks with a predominantly unidirectional filling pattern. In practice this means that the flow front should be straight and remain perpendicular to the overall length direction of the blank throughout the plate section. The traditional way of bringing this about is to use a 'fan' or 'coat hanger'-type inlet in combination with a flow-restricting gate. A better result may be achieved by differentiating the gate thickness across the width of the gate. With the largest flow restriction closest to the point of injection, this approach can be optimised to give reasonable results even with fairly compact inlet geometries. The disadvantage is, however, that the optimised cross-section function for the gate depends on the shear-thinning behaviour of the melt for which it is designed. This renders the approach less suitable for a test specimen mould, which shall cope with many different polymers and process settings. Both the traditional modified fan inlets and coat hanger-types also have the disadvantage of not providing a constant shear-history across the plate width, another point rendering such solution less desired for this purpose.

The chosen approach towards obtaining a straight flow front was inspired by a test plate mould made by Delaunay *et al.* [11;12]. A straight flow front is obtained by means of double-curved profiling of a fan-shaped inlet geometry, leading the melt from the hot runner nozzle via an ejector pin zone to the plate part of the blank – see Figure 2.2.
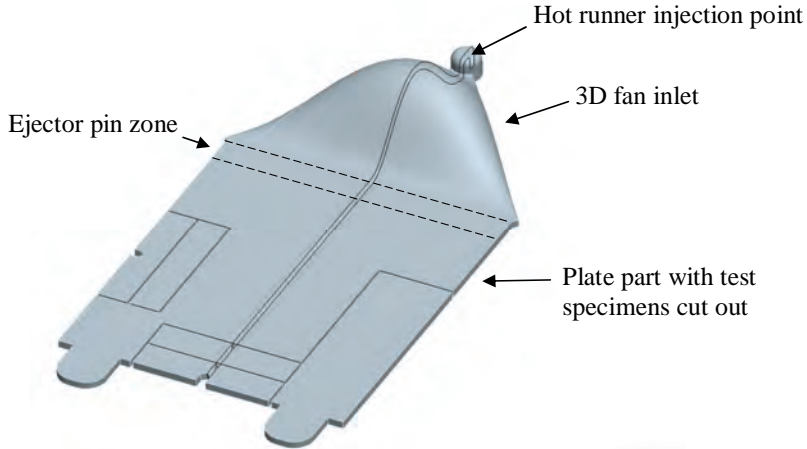
Figure 2.2: Test blank of configuration 3, with test specimens machined out.

The thickness remains constant and equal to that of the plate (1.5 mm) throughout the three-dimensional fan inlet. The midplane surface was modelled by a 4th order polynomial in a cylindrical coordinate system, with origo in the point of injection:

$$z(r) = \psi r^2 \left(r^2 - 2r + 1 \right)$$
<div align="right">Equation 1</div>

The midplane surface was defined in the CAD software (Pro/Engineer Wildfire 2) through ten trajectories with different values of the angular coordinate and the scaling parameter ψ. The latter was determined for each trajectory numerically, so as to keep the curve length s constant and equal to that at the maximum angle (corresponding to the plate width) with $\psi = 0$, where

$$s = \int_0^1 \sqrt{1 + \left(dz/dr \right)^2} \, dr$$

and r1 is the distance from the injection point to the ejector pin zone. The result is ideally a flow-path independent pressure drop throughout the inlet system, and a predominantly unidirectional flow in the plate. Two factors contribute to the lack of perfect straightness however. The cooling condition in the out-of-plane direction is asymmetric and the offset of the modelled midplane to form the mould surfaces of the inlet leads to undercuts in the geometry near the edges. The latter could be solved by minor manual adjustments of the geometry, but the former may not easily be counteracted. In theory it should be possible to obtain a thermally and rheologically balanced system, but such a solution would require coupled modelling of geometry and moulding process and was not attempted for this mould. Rather, the simple geometrical optimisation was paired with an adjusted cooling line layout based on preliminary Moldflow simulations of the filling stage[A]. The result obtained in this way was found to yield the desired fill pattern, with a slightly convex flow front preventing entrapment of air when used for making test blanks with a central weld line (configuration 4 – has not been used for the reported studies). A simulation of the fill pattern of configuration 1 is shown in Figure 2.3.
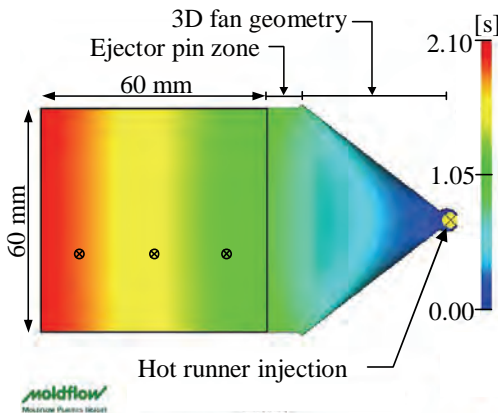
Figure 2.3: Fill time simulation in Moldflow software with the pure POM grade as model material (see chapter 2.3). The three circles show the position of the p&T-transducers (see main text below).

The mould has been equipped with three combined cavity pressure and temperature transducers (Ø2.5 mm) along the flow path (Kistler Nordic Danmark). The transducers make it possible to monitor these two important realized process conditions throughout the moulding cycle. Data from the transducers were used for process run-in for the moulding of test blanks for the Impact & Indentation Study. The data may also be used for comparison against injection moulding simulation software.

Figure 2.4 shows the cooling line layout of the mould. This final layout was the result of some iterations, where Moldflow simulations had shown that the initial solution lead to too much heat transfer from the hot runner nozzle to the sculptured fan inlet. With the chosen solution, the filling stage simulations showed that the temperature rise in this part of the blank could be kept within a few degrees.

[A] Injection moulding simulations in this project has been made by supervisor Mogens Papsøe from the department of Device Simulation at NNAS.
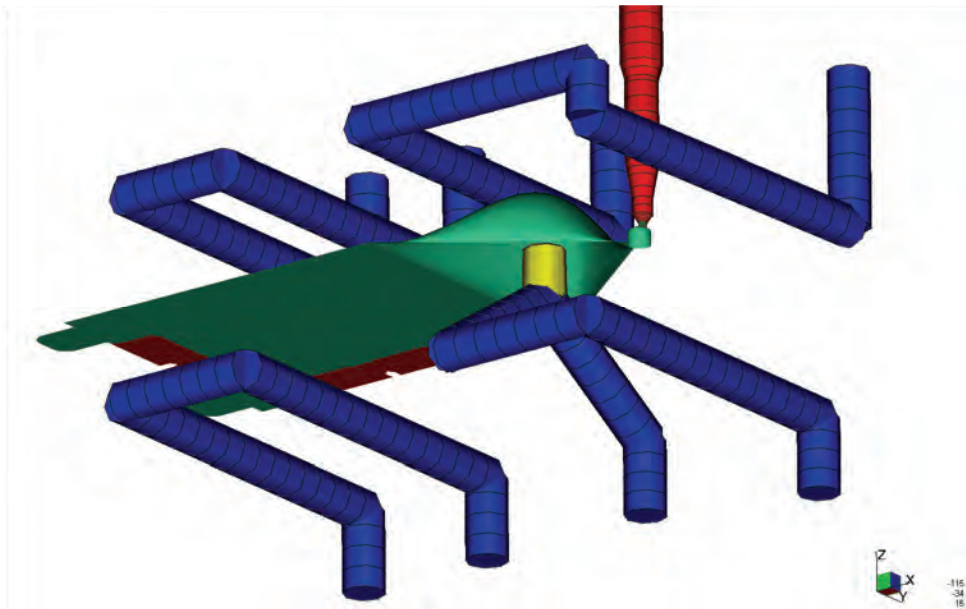
Figure 2.4: Cooling line layout in test blank mould.

The mould venting was made so as to accommodate vacuum evacuation of the cavity (described in appendix 11.1. This calls for tightly mating surfaces in the parting line, and short film vents with large venting channels behind to avoid excessive build-up of counter pressure during fast filling of the mould (when not using vacuum evacuation). To avoid the formation of flash when moulding low-viscosity polymers, the film vents must be kept relatively thin. Several iterations were made in cooperation with the mould maker before a satisfactory venting solution was reached.

Some key specifications of the final mould are listed in Table 1. An overview image of the CAD design of the mould can be found in appendix 11.1.

Table 1: Key mould specifications.

Hot runners	Husky U750 VG HR
Steel for inserts	Uddeholm Stavax
Mould instrumentation	Kistler, combined p&T, type 6189A
Build height	477 mm
Smallest distance between tie bars	346 mm
Interface to cylinder	Std. R40

2.2.3. Experimental qualification of moulding setup

The experimental qualification of the mould was based on mouldings of a low viscosity polyamide (PA), a high viscosity polycarbonate (PC) and the standard flow POM used throughout the project. The PA mouldings were used to test the mould for tightness and tendency to form flash in the parting line. The PC mouldings were used to ensure adequate mould stability under high injection and packing pressures. Several months of adjustments of the mould design and realised production tolerances had to be made before the mould could finally be qualified in spring 2008. Series of short

shots were used to qualify the realised sculptured fan inlet cf. the argumentation in chapter 2.2.2 – see Figure 2.5.
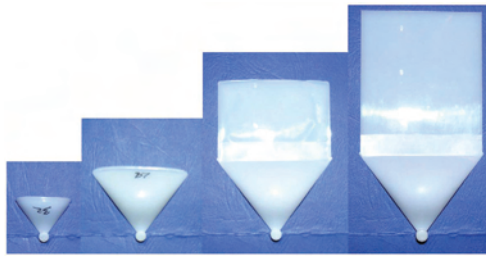
Figure 2.5: Short shots of PA in configuration 1, ending with a fully moulded test blank (right).

2.3.   The plastic grades for these studies

The reported studies of my project have all taken offset in the standard-flow copolymer POM Hostaform C9021 from Ticona. The grade is copolymerized from trioxane and dioxylane, giving it higher thermal stability compared to homopolymer POM. It is characterized by a solid density of 1.41 g/cm^3 (ISO 1183) and a melt volume rate (MVR) of 8 cm^3/10 min. (190°C, 2.16 kg) (ISO 1133). Molecular weight has not been determined and no references stating this characteristic have been found. The grade is one of the most widely used standard copolymer POM grades across the injection moulding industry and has been studied by several research groups. It therefore constitutes an attractive model material. Furthermore, it may be seen as a reference grade for the POM grades used in NNAS. The grade is in the following referred to as 'pure POM'.

The base plastic for the Additives and Impact study was the pure POM grade described above, but containing also additives for laser-engraving. The grade is used in the industry for components that require marking of numbers or other indications. The laser additive is based on TiO$_2$ and carbon black, and is of black colour, whereas the pure POM in itself is opaque white. The grade containing laser additive is in the following referred to as 'neat POM'.

The effect of the admixture of two tribological additives were tested in the Additives and Impact study: poly(dimethylsiloxane) (PDMS) and poly(tetrafluoroethylene) (PTFE). The PDMS additive was supplied as masterbatch based on a POM carrier (Process Master 755, Add Master UK Ltd.). The masterbatch is characterized by a 50-60 wt% concentration of PDMS, with an approximate weight-average molecular weight and polydispersity index of 447.000 and 1.97, respectively. Molecular weights were determined by gel permeation chromatography (GPC) on tetrahydrofuran (THF) extracts at Risø DTU. The PTFE additive was supplied as a low molecular weight powder (Zonyl MP1300, Du Pont De Nemours B.V.). It is characterized by a specific surface area of 1.5-3 m^2/g (ASTM 4567) and an average particle size of 12 μm (ASTM 4464), with 10th and 90th percentiles of 3 μm and 25 μm, respectively. The composition factors in the experiments of this study were the presence or not of the two additives in certain concentrations. An earlier internal study in NNAS had shown that 2 and 5 wt% of the PDMS masterbatch and PTFE additive, respectively, were sufficient for reducing friction of POM sliding against poly(propylene) (PP) (I.M. Sivebæk, *private communication*). These concentrations were used as high level for the composition factors. Compounding of additives and neat POM was done by twin screw extrusion with subsequent water bath cooling, pelletising and centrifugal drying (Melitek, Denmark). Three modified grades were tested in the Additives and Impact study: the neat grade modified by PDMS, by PTFE and by both PDMS and PTFE.

2.4. Moulding of test blanks

Various test blanks have been moulded for the experimental investigations, with various combinations of additives and process conditions. The process conditions are varied to reveal potential changes in processing window for the blended grades.

2.4.1. Injection moulding setup at NNAS

All injection mouldings for the studies in this project have been performed on a 90 tonnes servo-hydraulic injection moulding machine (S90 SR18/22, Husky Injection Moulding Systems) with an 18 mm general purpose screw. The mould temperature is controlled through a water-based cooling aggregate (Wittmann), providing nominal coolant temperatures in the range 10-90°C. Most of the qualification mouldings were also performed on this setup.

2.4.2. Test blanks for the Additives & Impact Study

The test blanks for the Additives & Impact Study were moulded in configuration 1, i.e. into 1.5 mm thick plates with low surface roughness (polished mould cavity). All the four grades (neat, +PDMS, +PTFE, +PDMS&PTFE) were dried at 120°C for 3 hours prior to injection moulding.

The two main elements of the Additives & Impact Study, friction testing and impact testing, were both run as randomised 2^4 factorial experiments with two grade composition factors and two processing factors. The processing factors were the mould temperature and injection melt flow. The process levels were nominal values, i.e. set-point for mould coolant temperature and machine injection ram speed. The low level injection melt flow was chosen based on a process optimization run in Moldflow MPI 6.1 simulation software. The high level melt flow was chosen to give the same shear rate in the hot runner nozzle (the point of highest shear rate) as reached during moulding of a component in a particular device, made of a similar POM resin (~18,000 s^{-1}). The corresponding fill time and power-law-corrected shear rate in the plate section of the blanks were 2 s and ~400 s^{-1}, respectively. The nominal melt front velocities are 67 and 122 mm/s for low and high melt flow, respectively. The low and high settings for the nominal mould temperatures were 50°C and 90°C, respectively. The high level confers to the recommendation from the material manufacturer. The low level is well below the recommendations, yet it is known to be used in production of certain less critical components in POM. Such low values are chosen in production to reduce cycle time or counteract shrinkage when desired in order to meet certain tolerance requirements (injection moulder from NNE Pharmaplan, *private communication*). The designations for the four process conditions are slow&cold (S&C), slow&warm (S&W), fast&cold (F&C) and fast&warm (F&W), with e.g. the latter referring to fast melt injection into a warm mould – see Table 2.

Table 2: Experimental factors and levels for the Additives & Impact Study.

Factor	Low level	High level
PDMS MB concentration	0 wt%	2 wt%
PTFE concentration	0 wt%	5 wt%
Mould coolant temperature	50°C (Cold)	90°C (Warm)
Injection melt flow	6 cm^3/s (Slow)	11 cm^3/s (Fast)

Note that the PDMS concentration is given as masterbatch concentration, corresponding to approx. 1 wt% for the high level.

The key non-variable machine settings used for the mouldings for the Additives & Impact Study are given in Table 3. The process run-in was done by injection moulder H. Vallem (NNE Pharmaplan) based on his common praxis. The mould instrumentation was not used[A]. The realised melt temperature at the machine nozzle was measured to 192-193°C based on purge shots using a contact thermocouple. The realised plate thickness was measured to 1.48-1.49 mm irrespective of factor levels.

Table 3: Key non-variable machine settings for the injection moulding.

Machine settings	Values
Barrel temperature profile	190 / 190 / 190 / 190 / 180 / 45 °C
Hot runner temperature profile	210 / 200 / 200 °C
Specific holding pressure	70 MPa
Holding time	3.2 s
Total cooling time	13 s
Cycle time	21 s

2.4.3. Test blanks for the Impact & Indentation Study

The test blanks for the Impact & Indentation Study were moulded in configuration 3, i.e. into 1.5 mm thick plates with moulded-in notches. The POM grade used for this study was the pure grade without any additives. The process factors were the same as in the Additives & Impact Study, i.e. the set-point for the mould coolant temperature and the nominal injection melt flow. The factors were also changed in two levels, but for this study it was decided to use more extreme processing conditions in order for potential deterioration phenomena to be investigated in a more pronounced state. The levels for both factors are given in Table 4. They are designated as VerySlow&VeryCold (VS&VC), VerySlow&Warm (VS&W), VeryFast&VeryCold (VF&VC) and VeryFast&Warm (VF&W). Note that the high nominal mould temperature is the same as in the Additives & Impact Study, since it constitutes the upper limit of the mould tempering aggregate used.

Table 4: Experimental factors and levels for the Impact & Indentation Study.

Factor	Low level	High level
Mould coolant temperature	25°C (Very Cold)	90°C (Warm)
Injection melt flow	3.3 cm^3/s (Very slow)	16.8 cm^3/s (Very Fast)

The shear rate at the melt-mould wall interface may be estimated by the expression for shear flow of a shear-thinning fluid through a rectangular channel:

$$\dot{\gamma}_{wall} = \frac{(2n+1)}{n} \frac{2Q}{Wb^2} \qquad \text{Equation 2}$$

where Q is the melt flow, W is the channel width, b the channel height and n is the power law exponent characterising the shear thinning of the melt. For the present grade n equals 0.2075 according to the Moldflow materials database. Using this equation results in characteristic wall-shear rates in the plates of ~330 and ~1700 s^{-1} for the two melt flows, respectively. The similar values for the shear rate in the hot runner nozzle were estimated to be ~15×10^3 and ~76×10^3 s^{-1}, respectively. The former is well below the maximum value recommended by Moldflow for this

---

[A] An error handling of the instrumentation equipment by the mould maker had rendered it out of order at the time of these mouldings.

grade, 45×10^3 s^{-1}, but the latter is above. Though these recommendations are only meant as guidance (Stefan Kuhne, Moldflow GmbH, *private communication*), this does illustrate that the very-high level melt flow may be regarded as an extreme processing condition.

Key non-variable machine settings for the injection moulding are given in Table 5. The process run-in took offset in the recommendations from Whelan & Goff [6], and was based on the pressure curves from the mould instrumentation. A nine-step injection speed profile was calculated based on Moldflow data to keep the flow front velocity throughout the filling stage as steady as allowed by the machine controls (supports only step profiling). Holding times were 4 and 8 s for the low and high mould temperature, respectively. Injection moulding tables describing the machine settings for each of the four processes, including the injection profiles, can found in Appendix 11.3. The realized plate thickness of the mouldings were measured to 1.48-1.51 mm depending on the factor levels. Key variable processing conditions are given in Table 6. Pressure curves from each of the processes can be seen in Figure 2.6.

Table 5: Key non-variable machine settings for the injection moulding.

Machine settings	Values
Rotational speed during plasticization	212 RPM (0-85%), 180 RPM (85-100%)
Back pressure during plasticization	4 MPa
Barrel temperature profile	200 / 200 / 195 / 185 / 175 / 50 ℃
Hot runner temperature profile	200 / 200 / 200 ℃
Specific holding pressure	80 MPa
Cooling stage time	6.5 s

Table 6: Key variable processing conditions for the injection moulding.

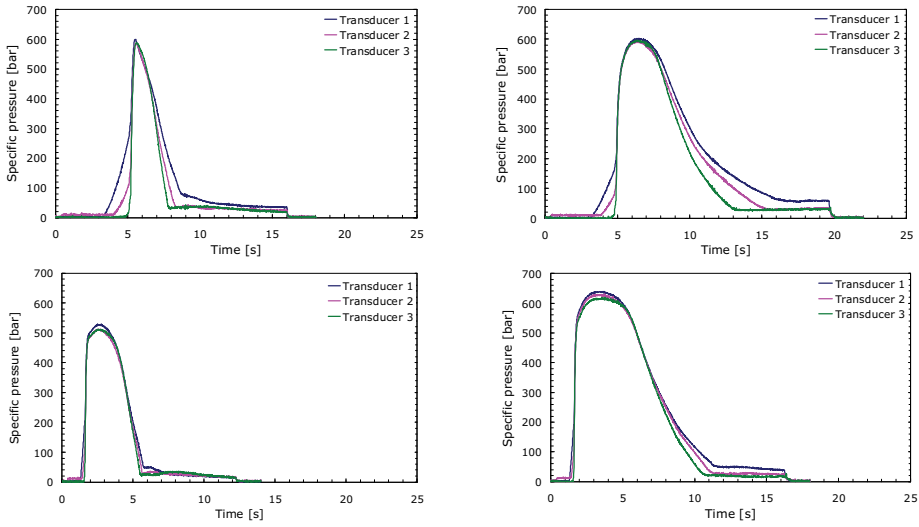| Condition \ Group	VS&VC	VS&W	VF&VC	VF&W
Injection fill time [s]	4.7	4.3	0.9	0.9
Max. specific fill pressure [MPa]	142	103	184	174
Holding time [s]	4	8	4	8
Cycle time [s]	18.9	22.5	15.2	19.2

Figure 2.6: Cavity pressure profiles from injection moulding of test blanks for the Impact & Indentation Study. Upper left: VS&VC. Upper right: VS&W. Lower left: VF&VC. Lower right: VF&W.

3. FRICTION BETWEEN PLASTICS

As it was mentioned in chapter 1 were the offset for this project a wish to investigate how tribological additives may affect the processability and mechanical properties of injection moulded plastics. A first requirement for the evaluation setup for such investigations was that the same test blanks should provide test specimens for both tribological and mechanical testing. It was therefore decided to conduct a study (first part of the Additives & Impact Study) to confirm the suitability of the plate blanks for use in combination with the tribology testing facility at NNAS, using a POM grade with tribological additives. This chapter reports on this investigation.

3.1. Introduction to polymer tribology

Most work reported in the literature on the tribological performance of plastics takes offset in conditions relevant in civil engineering, the automotive industry or the conventional machinery industries. Typical applications are bushings, gears and bearings. For this reason, the vast majority of published articles on this subject deal with plastics sliding against steel [13-27]. Fewer authors report work on polymer-polymer friction. Studies that deal with this subject include the work of Jain and Bahadur [28], Erhard [29], Czichos [30], Yamada [31], Hu [32], Apichartpattanasiri and co-workers [13] and Mergler and co-workers [23]. Jain and Bahadur [28] investigated the formation of transfer films in sliding between among others polyethylene (PE) films and polypropylene (PP) and PTFE discs. Particularly low values of both static and dynamic coefficients of friction (CoF) were reported for the PE-PTFE constellation under certain conditions, 0.05-0.06 and <0.04, respectively. These conditions were found to coincide with a thick and coherent transfer layer of PTFE on the PE films. Erhard [29] compared the frictional properties of various polymer constellations with the work of adhesion between the two material surfaces. The good correlation found strengthened the adhesion-shearing theory originally proposed by Bowden and Tabor, described in detail by e.g. Yamaguchi [33]. The theory states that dry friction between neat polymeric materials is dominated by local adhesion between asperities and subsequent shear yield or rupture of the material with lowest shear strength under the local conditions. The work of several others, summarized in e.g. [33], has also underpinned this theory. Czichos [30] found adhesion also to be the dominating factor in tests with PTFE, POM and PP pins on discs of various amorphous polymers. Yamada [31] studied sliding between high density polyethylene (HDPE), PTFE, PP, polyamide (PA, nylon) and POM, and concluded that friction between polymers in general depends largely on both materials in the contact. The only exception found was PTFE for which earlier findings of thin transfer layers formed on the counterpart surface was confirmed. PTFE gave in all combinations a lowest CoF of approx. 0.1-0.12 after typically at least 50 m of running-in. The constellation PP against POM gave a CoF of 0.19-0.22. Hu [32] investigated friction between a nylon ring and blocks of neat POM, a POM-PTFE blend and a polyurethane-blended POM with PTFE and silicone oil additives. He found the latter to decrease friction more than the PTFE additive alone. As many others, he also found that increasing the normal load led to a decrease in CoF. The underlying mechanisms for this are theoretically explained by Hertz' contact theories or Meyer's theory of indentation, and are thoroughly described in e.g. [33]. Mergler *et al.* [23] have reported on friction studies of a co-polymer POM slid against it self in a pin-on-disc setup. A CoF around 0.5 was measured.

The plastic test specimens used in the reported studies are most often machined from semi-finished extrudates or castings, or made by roller compacting or compression moulding. Relatively few studies are reported on the effect of injection moulding on tribological properties. Exceptions are the work by Yamaguchi [33], Apichartpattanasiri and co-workers [13], and by Jeng and co-workers

[21]. Yamaguchi [33] shows how the degree of crystallinity of polyethyleneterephthalate (PETE) is increased from 30% to 45% by increasing mould temperature 60°C to 140°C. The author correlates this with an observed decrease the kinetic CoF against steel from 0.33 to 0.26. The same correlation with crystallinity is found for PE and PTFE. Apichartpattanasiri *et al.* [13] dealt with the tribological behaviour of a PA66 injection moulded under varying mould temperatures and slid against it self. The skin-core morphology was found to depend strongly on the mould temperature. For technical reasons, the skin layer was machined off the specimens prior to friction testing. The results obtained thus represent the frictional properties of the core material when moulded under different mould temperatures, rather than that of the specimens as-moulded. Little effect on friction was found from changing mould temperatures between 30°C and 90°C. Jeng *et al.* [21] looked into how the tribological properties of a fibre-reinforced polybutyleneterephthalate (PBT) are affected by varying fill time, melt temperature, mould temperature and packing pressure. The composite was tested against a steel ball in directions both parallel and perpendicular to the local flow direction. Generally, the CoF in the two directions showed opposite trends when varying the process parameters, and settings promoting low friction was found for both directions. Regarding mould temperature, lower friction was found in the direction parallel to the flow, but only minor changes was seen going from 60 to 120°C. Filling time, inversely proportional to the realized injection melt flow, showed a global minimum in friction between slowest and fastest filling for the direction parallel to melt flow. Interactions between process parameters were not investigated.

Several authors report on friction studies of POM with various tribological additives, including PTFE [14;20;24;32], PDMS [14;32], linear low-density polyethylene (LLDPE)[27], graphite and MoS$_2$ [22]. The additives are in all cases found to significantly decrease the CoF. Benabdallah [14] found that the CoF for neat POM against galvanized steel of approx. 0.35 decreased to approx. 0.30, 0.20 and 0.22 when adding PTFE powder, PTFE fibres and high viscosity PDMS, respectively. He also found for these blends, that the CoF decreased with increasing normal load. Odiowei & Schipper [24] report that blending a copolymer POM with 15 wt% PTFE had no significant effect on the hardness of the material (measurement technique not stated). Moreover, they found that the blend was much less influenced by the surface preparation of the counter part than the neat POM specimens. The result was consistent with an observed transfer layer from the blends and no transfer from the neat POM.

Focus in the above-mentioned work have primarily been on friction and wear properties after sliding distances longer than encountered in prefilled medical devices. In a particular insulin pen, sliding of a POM part against a PP surface is characterized by a nominal surface pressure of 3 MPa, a sliding velocity of 0.02 m/s and an accumulated operating time of 20 s. None of the referenced investigations deal with friction under such conditions, where wear may be considered irrelevant and where a given need for running-in is unmet. For this reason NNAS has made their own apparatus and protocol for measuring tribological properties of plastics under conditions relevant for the use in medical devices. The apparatus is called the TriboTester and is described below.

3.2. The TriboTester setup

The TriboTester [10] was developed by T. Ruby and T.J. Herslund during their BSc project at NNAS. The project was supervised by I.M. Sivebæk, who also has been supervisor within tribology on this project. The principle of the TriboTester can be seen in Figure 3.1, together with a close-up of the specimens in place, as used in this project. The test plates were machined from the injection

moulded blanks. The apparatus had to be modified slightly to accommodate plates[A]. The TriboTester is made with a ring-on-disc setup. It works by rotating a lower disc specimen against an upper, stationary ring specimen. A normal force between the specimens is generated by means of a numerically-positioned deadweight on a lever. The torque between the upper specimen and its fixation is measured during the test and the CoF is calculated from this value. All actions are programmed through a PC interface. The plate specimens were fixed to the rotor disc by means of thin double-sided tape under the entire surface. The contact between the specimens is characterized by a mean diameter of 27 mm and a nominal contact area 129 mm[2].
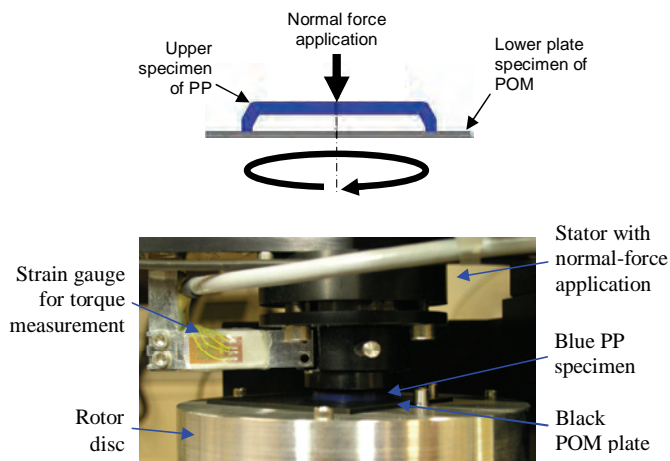
Figure 3.1: Principle sketch of TriboTester specimens in cross-section (upper) and close-up of specimens in TriboTester apparatus (lower).

3.3.   The Additives & Impact Study – friction testing
3.3.1. Introduction
The friction testing part of the Additives & Impact Study addresses how the frictional performance of the moulded neat POM is affected by the two tribological additives, PDMS and PTFE, and the two injection moulding parameters, mould temperature and melt injection flow. Friction is evaluated under conditions simulating sliding against the PP counter surface in the injection device mentioned in chapter 3.1, using the TriboTester apparatus. Injection moulded POM and PP are both widely used in prefilled drug delivery devices. In some injection pens for insulin administration these two materials engage in sliding contact and the frictional properties of this constellation is thus of interest to NNAS.

3.3.2. Experimental
All friction testing was performed under a sliding velocity of 0.02 m/s and a normal force between the two specimens of 387 N, corresponding to a nominal surface pressure of 3 MPa. The tests were

---

[A] The geometry of the standard specimens were updated in the beginning of the project as part of the initial investigations, to mitigate some inexpediencies that had been encountered with their original design.

run for 20 seconds at ambient conditions of 23±2°C and 45±10% RH. Both the static and kinetic CoF are reported, the latter taken as the mean value during the last 19 seconds of test.

The counter surface material for the friction tests (upper specimens in TriboTester) was a block copolymer PP with 1 wt% Zn-stereate as mould release agent and 6 wt% blue colour masterbatch. The grade is characterized by a solid density of 0.905 g/cm^3 and a melt flow rate (MFR) of 15 g/10 min (230°C, 2.16 kg). The PP specimens had been moulded externally in a cold runner steel mould with polished cavity (C. Christensen Aps, Denmark). The moulding conditions used were based on recommendations from the material vendor, though with a nominal mould temperature of 50°C.

3.3.3. Results and Discussion

Examples of the friction testing data are shown in Figure 3.2. The graphs exemplify data from the four grades. The minor periodic oscillations are artefacts of the experimental setup. A slightly increasing CoF is seen for the PDMS containing grades. With the present evaluation technique (20 s continuous measurement) it may not be determined whether this trend results from heat build-up or beginning running-in of the mating surfaces. In the former case the trend may be regarded as an experimental artefact. In the latter case, though the effect may be of technical interest, a quantitative characterisation would have to be made on a system more similar to the actual pen components for an evaluation of the practical relevance of such seemingly weak trend.

The initial peak in the curves for the neat and PTFE-containing grades indicates that these grades are prone to 'stick-slip' – a phenomenon that is highly limiting for their use in such constellation. The POM grades with PDMS on the other hand would operate smoothly against the PP and could thus also be used for components where stick-slip is critical (typically displacement-controlled sliding). The data presented in this study pin-points PDMS as an effective way of reducing the stick-slip tendency of the POM-PP constellation. Further conclusions from Figure 3.2 are discussed below.
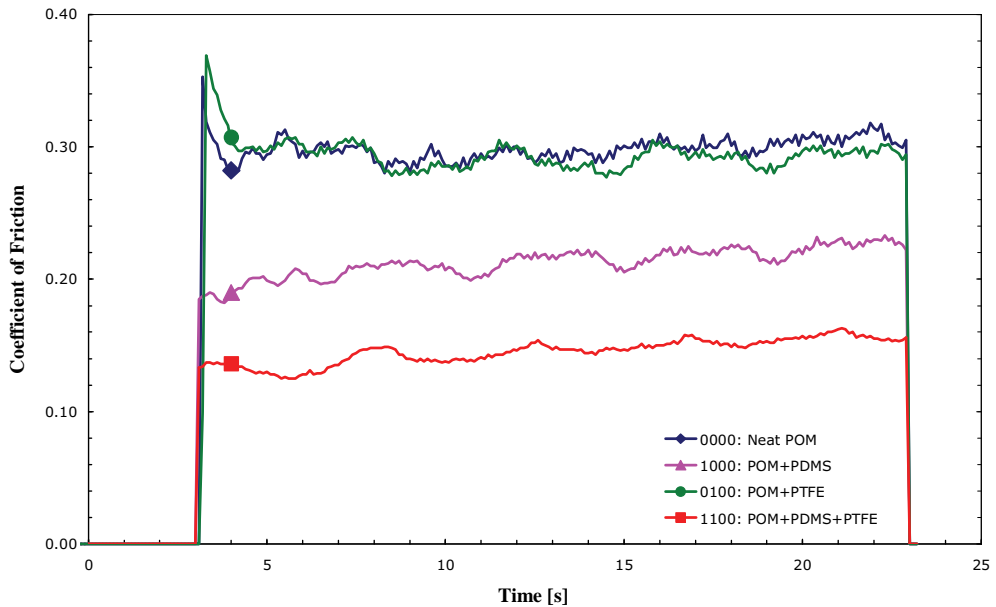
Figure 3.2: Example of friction testing data for the four grades with both process factors low (slow injection into a cold mould).

Variability charts of the response variables are shown in Figure 3.4. Box plots illustrate median, lower and upper quartiles. Group means are shown as green horizontal lines. No significant reduction in friction is seen from the admixture of PTFE alone, whereas PDMS alone results in a dramatic reduction of both static and dynamic CoF. The larger friction reducing effect of the PDMS additive is consistent with the findings of Benabdallah [14]. An interaction is seen from the combination of PDMS and PTFE, in which case the PTFE leads to a further and significant reduction in both response variables. This noteworthy synergistic effect has earlier been described by I.M. Sivebaek (non-published work), yet remains phenomenologically unexplained to our knowledge. The lack of reduction in CoF from the PTFE additive alone may presumably be ascribed to the relatively low concentration of 5 wt% (many commercial grades contains 10 or 18 wt%), low true surface pressure (limited by the low yield stress of the PP counterpart) and low sliding distance. All these conditions may effectively hinder the formation of an oriented PTFE transfer film and thus preclude its friction-reducing effect. Ruby *et al.* [10] suggests that pressure-induced conformational changes in PTFE may be a prerequisite for its low friction properties. Such changes may be hindered in the present grade by the high stiffness of the surrounding POM matrix. This could explain how the PDMS additive may change the effectiveness of the PTFE additive through a reduction in the contact stiffness. Same reasoning can explain an effect at higher PTFE concentrations without PDMS, suggesting a highly nonlinear correlation with the concentration. Further investigations would be required to confirm or deny this hypothesis.
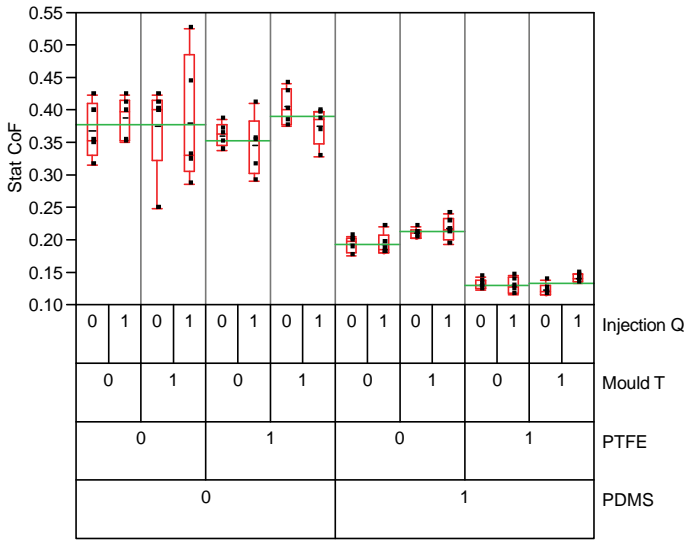
Figure 3.3: Variability chart for static coefficient of friction.
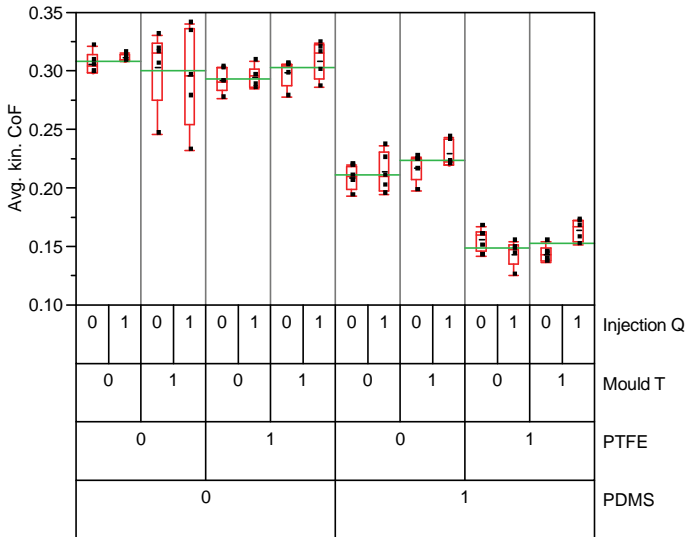
Figure 3.4: Variability chart for average kinetic coefficient of friction (right).

Figure 3.5 illustrates the results of a statistic effect screening on 5% level of significance (statistic software: SAS JMP 6.0.2). Non-significant effects and interactions were successively removed from the original 2nd-degree factorial model. The effect of the significant variables are given as relative change in the two response variables, when changing level from low (0) to high (1), while keeping the other factors and interactions at the intermediate level (0.5). The stated values for the interaction represent only the synergistic part of the low-high change of the constituents. Probability values ('p-

values') from Student's t-tests indicate the strength of each factor and interaction. The figure illustrates the overall impression from the variability charts, namely that no overall significant effects or interactions from the processing factors were observed. The DOE with only four repetitions was deemed too uncertain for a statistic effect screening on group level among the samples of same grade but different processing history. The level of processing-induced changes indicated in Figure 3.4 suggests that this effect would be of little technical relevance anyhow with the chosen process variations.
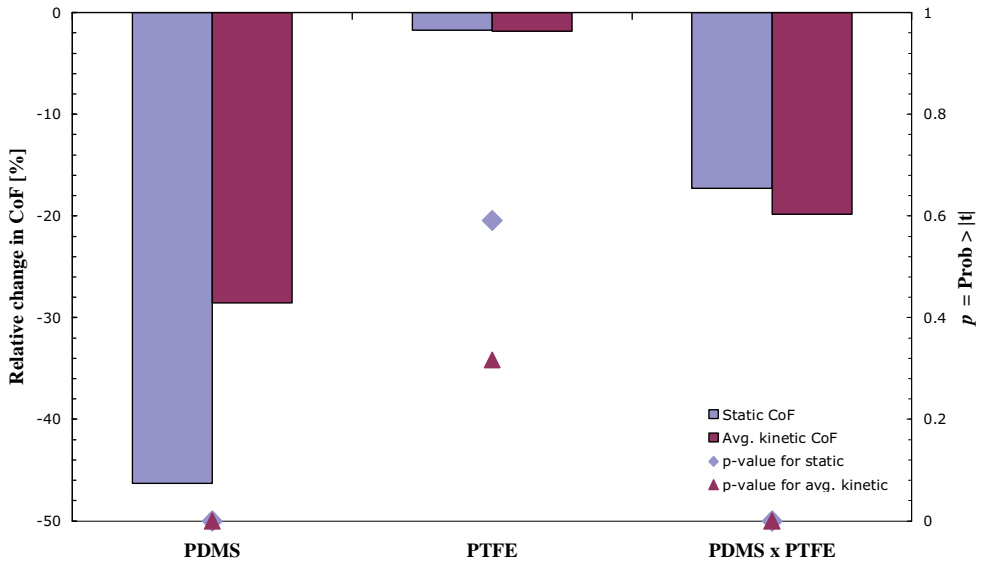
Figure 3.5: Statistic effect screening for factor change low (0) to high (1). Only significant effects are included in the model for each response variable.

The static CoF values for the neat POM measured in this study compare well with those referenced in the introduction (0.38 on average vs. 0.38 found by Yamada [31]) despite a relatively large difference in apparent surface pressure (3 vs. 0.18 MPa). These results thus agree with Coulomb's law whereby the static CoF is independent of the apparent contact area. The kinetic CoF data found for the neat grade in this study are similar to those measured in earlier studies in NNAS on this grade constellation[A], but are some two-thirds higher than those referenced by Yamada (0.30 on average vs. 0.18). The difference in apparent surface pressure for the two setups compared is high (3 vs. 0.08 MPa), but Hertz's and Meyer's laws (where kinetic CoF $\propto p^m$ with $-\frac{1}{3} \leq m \leq 0$) [31] predicts a lower kinetic CoF in our study. The opposite observation may be due to differences in process history, sliding speed (2 vs. 6 cm/s) and sliding distance. The latter is for literature data usually much longer than the 40 cm accumulated length used in this test setup and may well promote lower kinetic CoF due to e.g. heat build-up.

[A] 0.28-0.31 had been found using an earlier yet largely similar setup on the TriboTester (I.M. Sivebæk, *private communication*).

3.3.4. Main conclusions

The following main conclusions may be drawn from the presented investigation:

- Friction is significantly reduced by the PDMS additive in 2 wt% masterbatch concentration. Friction of neat POM is not affected by the admixture of 5 wt% PTFE additive tested under the presented conditions.

- Friction of POM with PDMS additive can furthermore be significantly reduced by the admixture of 5 wt% PTFE additive.

- Consistent effects of the varied processing conditions have not been observed across the four grades tested. From these results it may therefore be concluded that the varied processing conditions do not significantly affect the coefficient of friction. Further investigations are needed for evaluation of the effect of process conditions on a grade level. Such investigation is outside the scope of this project.

- The suitability of the plate blanks for use in combination with the TriboTester has been confirmed.

4. MICROSTRUCTURE AND MORPHOLOGY OF TEST SPECIMENS

This chapter provides a characterisation of the microstructure and morphology of the injection moulded test blanks of the Impact & Indentation Study, described in chapter 2.4.3. It describes how microstructure may be assessed in terms of characterisation techniques, applied to the test material of the mentioned study. Same exercise have not been carried out on blanks from the Additives & Indentation Study, partly because the laser additive of the neat POM grade makes it less convenient for investigations of this kind.

4.1. Microtomy and polarised light microscopy

The microstructure and morphology of the moulded plates of the Impact & Indentation Study were examined by polarised light microscopy (PLM) (described in detail in [34]). Thin sections of plate cross-sections were prepared from the position shown in Figure 4.1. A Jung Supercut 2065 microtome (Leica) was used to cut sections of both 2 and 10 µm thickness. Each section was sandwiched between a glass slide and cover slip, submerged in a drop of Canada Balsam (liquid resin of same refractive index as glass). The sections were studied between crossed plane-polarisers using a DMI5000M microscope (Leica), with the melt flow direction (FD) approx. 45° off the polarisation angles. Micrographs at 50X and 200X were used in characterisation of the layered microtructure, based on the framework of Bowman [35]. Low magnification PLM micrographs of the 2 µm thin sections from the four process conditions are shown in Figure 4.2.
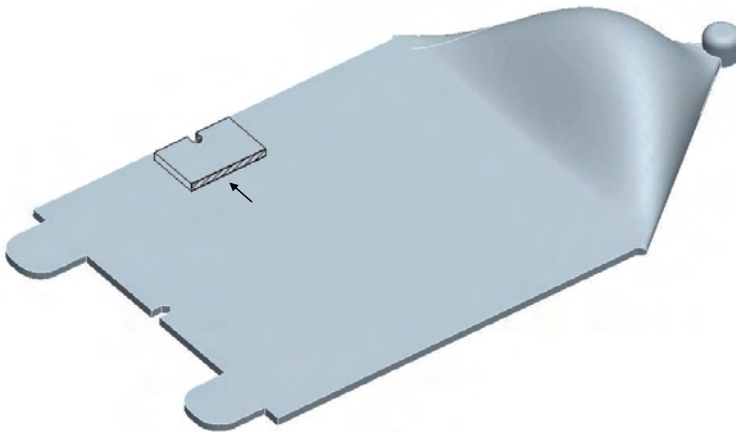
Figure 4.1: Position of cross-section for PLM micrographs.

The microstructure and morphology of injection moulded POM can be characterized in terms of a symmetric sandwich structure of five characteristic layers [35]. Layer 1 is the outermost surface layer. Observed in polarized light it is featureless and highly birefringent. According to Bowman this layer is not amorphous, but consist of a stacked lamella structure. Layer 2 contains oriented spherulites ('comet' spherulites) growing in direction away from the mould wall. The interspherulitic material is highly birefringent. Layer 3, referred to as the 'shear layer', consists of material that has deposited directly from the core flowing melt. It has not been exposed to the elongational flow at the flow front and its crystallization is dominated by shear-induced nucleation into an oriented crystalline structure of sheared lamella. It may possibly contain extended-chain lamella (known as 'shish-kebabs'), yielding a high degree of molecular orientation. In the

terminology of the common three-ply skin-core model [9;36-38] the layers 1, 2 and 3 represent the skin layer. In this five-layer description of the microstructure the term 'δ-layer' will be used instead [39], the term 'skin' referring to layer 1. Layer 2 is often denoted the transition layer. Layer 4 has little preferred orientation and is mainly distinguished from the isotropic spherulitic layer 5 in the core by a smaller size of spherulites possibly of the comet spherulite type.

VS&VC   VS&W

VF&VC   VF&W
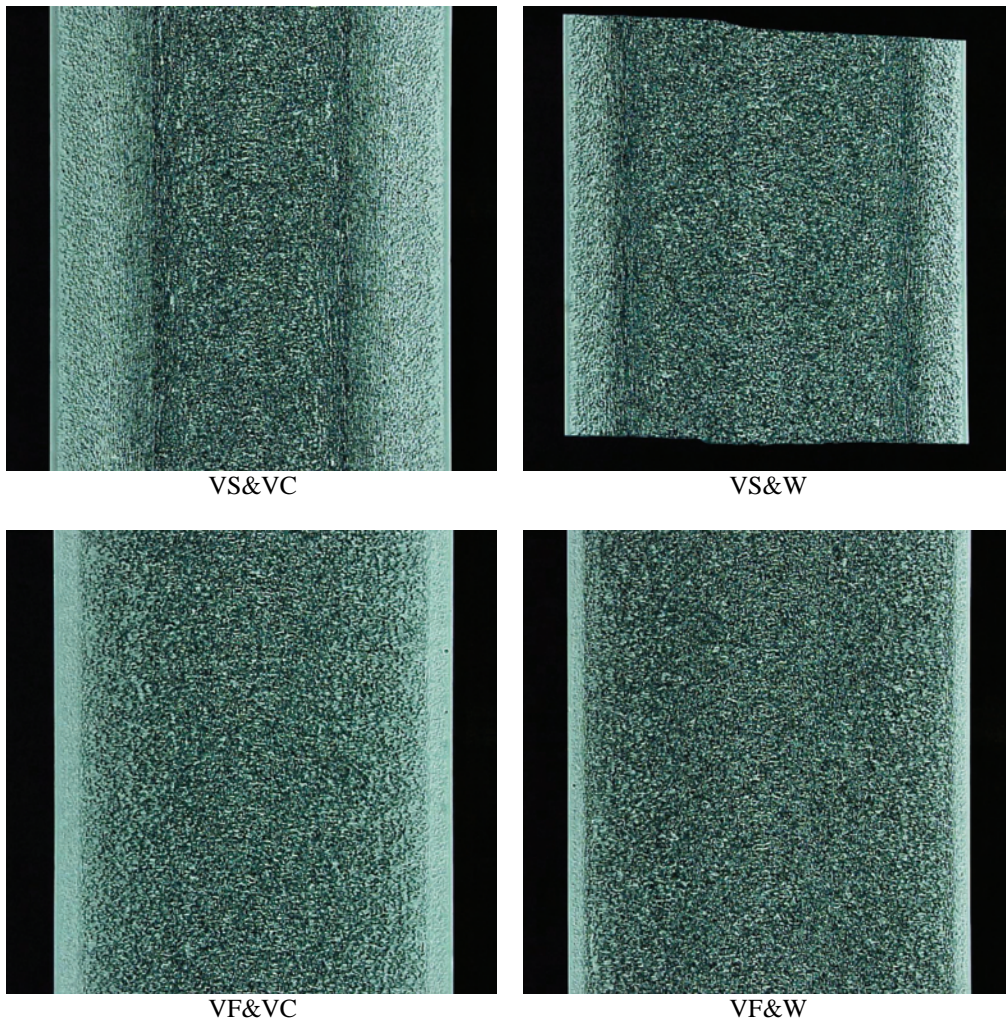
Figure 4.2: Low magnification PLM micrographs of the 2 µm thin sections from the Impact & Indentation Study. The sample width is approx. 1.5 mm.

The microstructure of the mouldings can be seen in detail in the high magnification micrographs shown in Figure 4.3, alongside an indication of the approximate extent of the layers 1-5 for the four different process conditions.
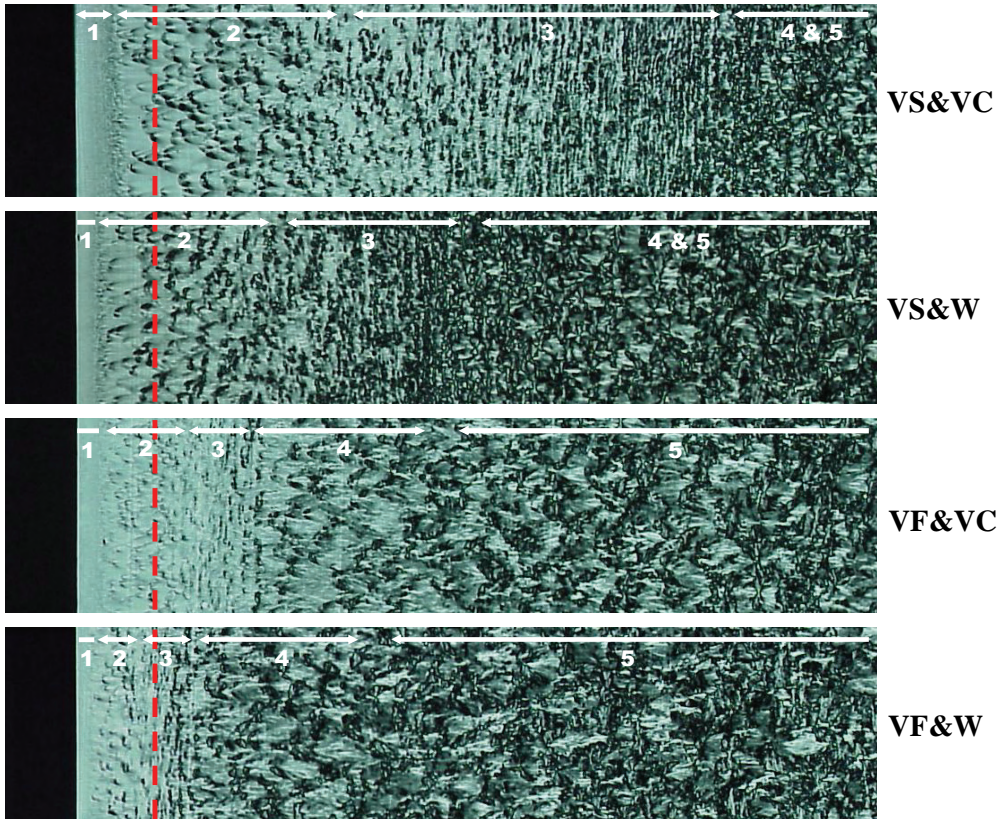
Figure 4.3: High magnification PLM micrographs of 2 µm thin sections from the four process conditions of the Impact & Indentation Study, with indications of the approximate extent of the five layers of the microstructure cf. Bowman [35]. The injection melt flow direction is vertical and the crossed polarisers are angled at ±45° hereto. The dashed red lines indicate a depth of 50 µm below the free surface.

By comparison the following may be added to the conclusions of Bowman [35]: Layers 1, 2 and 3 decrease in extend with increasing mould temperature and/or injection melt flow. The latter is in agreement with the findings of Scrauwen *et al.* [40] for injection moulded polypropylene and polyethylene. Increasing the injection velocity decreases the size of the comet spherulites in layer 2. Bowman [35] report the opposite effect when increasing the barrel temperature and the effect therefore indicates an increased rate of nucleation, since the increased shear heat contribution has the opposite effect. The slight increase in size from VF&VC to VF&W supports this conclusion. Layer 3 is very pronounced for the VS&VC process condition, but Bowman shows its extent to be highly dependent on the position of the sample relative to the flow length. We may therefore expect a far less extent of this layer in the TD specimens, the properties of which will therefore represent differences in both orientation and microstructure compared to the FD specimens. The implications of this is further discussed in chapter 7.
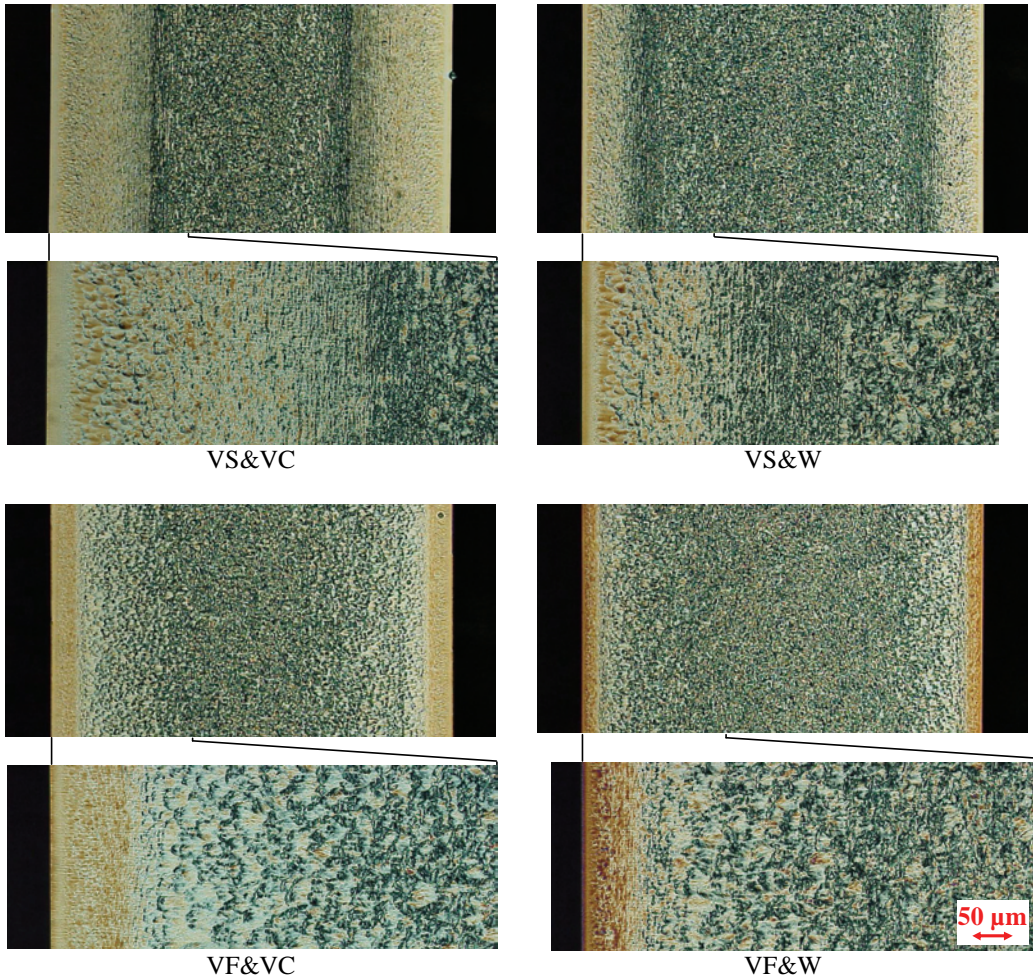
Figure 4.4: Low and high magnification PLM micrographs of 10 µm thin sections from the Impact & Indentation Study. The total width of the samples are approx. 1.5 mm. A scale bar for the close-ups is shown in the lower right corner.

The birefringence in the samples is seen to be too little to make the differences in retardation of the transmitted light discernible at a section thickness of 2 µm. This is not the case at 10 µm thickness, as shown in Figure 4.4, where the differences in optical anisotropy is clearly seen as differences in colour and brightness. Such differences in injection moulded plastics may result from differences in either degree of molecular orientation or residual stresses, the two origins not being distinguishable. A comparison with a Michel-Lévy chart [41] yields a maximum birefringence in the skin layers (layer 1) of the VS&VC and VF&W samples of approx. 0.040 and 0.055, respectively. For the former process condition, however, the maximum birefringence is found not in the skin layer, but in the interspherulitic material in the transition layer (layer 2). The value there is also clearly below the birefringence in the skin of the VF&W sample though, but the differences among the transition

layers are clearly less pronounced. The birefringence of the skin layer is found to be affected by both injection melt flow and mould temperature.

From the presented micrographs the influence of the two varied process conditions may be summarised as follows. High mould temperature leads to reduced thickness of layers 1-3 (the δ-layer). Fast injection has the same effect, but furthermore leads to finer comet spherulites in layer 2 and increased thickness of layer 4. Thicker δ-layer is reported by Bowman [35] to increase the yield stress of POM both parallel and transverse to the flow direction, i.e. highest yield stress may be expected for the VS&VC process condition.

4.2.   Thermal analysis

Differential scanning calorimetry (DSC) has been used to evaluate the homogeneity in degree of crystallinity of a moulded plate of neat POM from the Additives & Impact Study, by running temperature sweeps on samples from the positions shown in Figure 4.5 (left). A DSC Q2000 V23.12 from TA Instruments was used to heat the samples at 10°C/min from -70°C to +230°C in a Nitrogen atmosphere. The specific heat of the melting endotherms from the first heating are shown in Figure 4.5 (right). Taking the heat of fusion for 100% crystalline Hostaform C9021 as 249.36 J/g [42] the specific heat measures corresponds to 56.0-59.4% crystallinity. Highest crystallinity is seen for sampling position D. This is consistent with the melt forming this sample having been encapsulated by melt on both sides and between the two insulating frozen layers during flow. The same is the case for sample C, but less shear heating has been generated in this material during flow, leading a lower melt temperature at this point at end of filling. Sample B resembles sample C in shear heat input, but the faster cooling due to the proximity of the mould wall leads to lower crystallinity. Sample A is cooled fastest of all because of heat loss to the mould wall from four sides. The mould furthermore sees the least heat input from the melt at this position, providing a potential for a locally lower mould temperature.
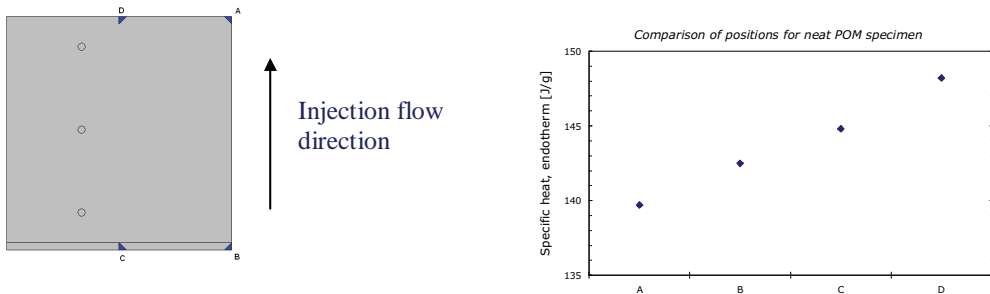
Figure 4.5: Sampling positions on moulded plate (left) and specific heat from melting in DSC (right).

DSC traces were also recorded on samples of the pure POM plates from the Impact and Indentation Study. Samples were taken containing either the total cross-section or only the outer approx. 0.2 mm of the microstructure. The latter samples were obtained by milling away the rest of the material and stacking 5 layers of the remaining sections in the pan. Care was taken to ensure that the stack had an even surface of contact with the pan and remained upright during encapsulation and transport to the instrument. The sampling positions are shown in Figure 4.6. Heating, cooling and

reheating traces were obtained at a rate of only 5°C/min to better allow for a homogenous temperature throughout the stacked samples. The resulting curves are shown in Figure 4.7. All samples of total cross-section shows a certain hump in the traces at a temperature lower than the peak temperature. The samples of the outer layer in general do not show this hump, indicating a correlation with the spherulitic morphology in the core. This is contrary to what would be expected from the higher crystallisation temperature in the core [43]. These samples, however, all show a distinct peak in heat flow. Only for the VF&VC process condition this peak correlates with the hump for the total cross-section sample, which also is largest for this process condition. The other of these samples shows the peak at higher temperatures, highest when the mould temperature is high, consistent with slow crystallisation favouring lamella thickening. The characteristics of the curves are given in Figure 4.8. The specific heat endotherms corresponds to degrees of crystallinity of 59-61% and 57-60% for the two sampling types, respectively, assuming the same heat of fusion for 100% crystallinity as above. The outer layer samples all show lower crystallinity than the average of the total cross-section, as would be expected from the faster cooling of the skin. The difference is most pronounced for the VS&VC process condition, indicating that the δ-layer constitutes the largest proportion for this process condition, as also found in the PLM investigation. The degree of crystallinity is highest for the process conditions with high mould temperature, as would be expected. High injection melt flow is seen also to provide a higher degree of crystallinity when the mould temperature is low, the potential mechanisms being both a reduced cooling rate due to shear heating and shear-induced crystallisation. The lack of this effect at high mould temperature suggest the former mechanism as the primary, but the difference in extent of the shear layer could lead to erroneous conclusions in this regard.
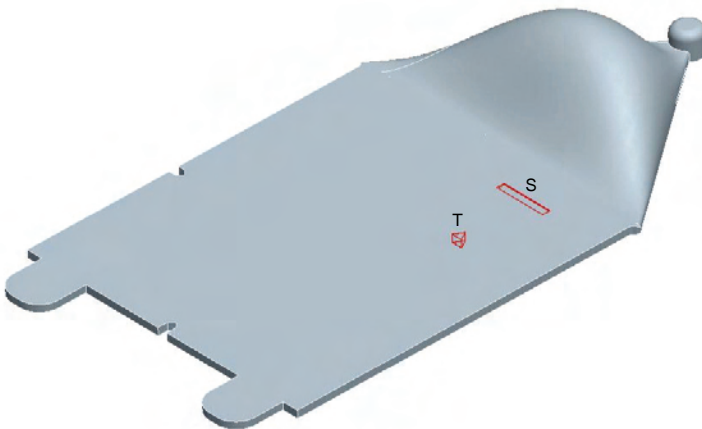
Figure 4.6: Positions of DSC samples of total cross-section ('T') and outer 0.2 mm only ('S'). The donor plates were also used for preparing the tensile testing specimens described in chapter 7.2, hence the alternative sampling positions.
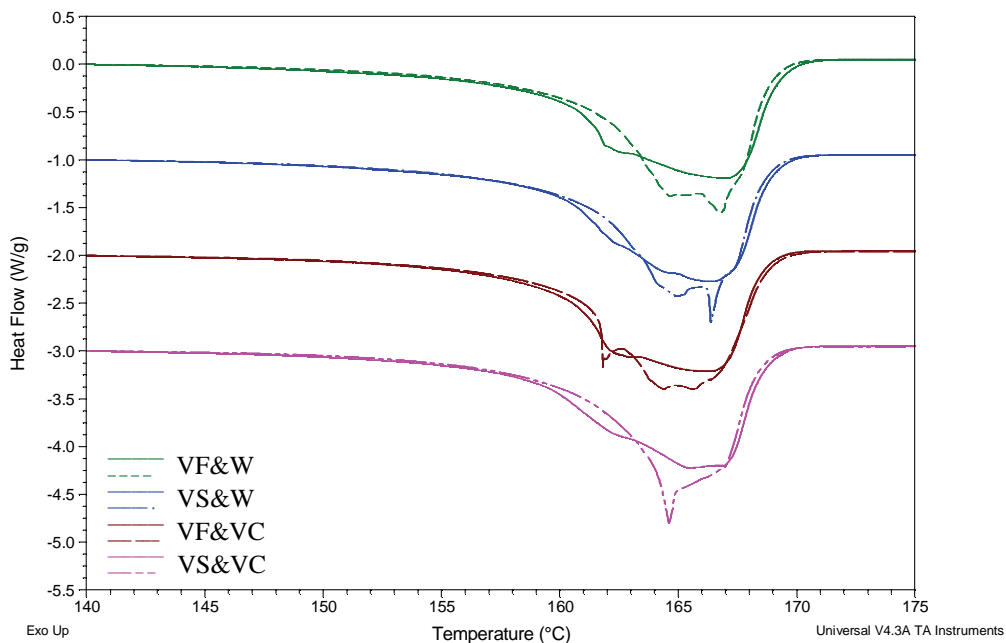
Figure 4.7: Comparison of DSC traces for samples of total cross-section and outer layers only, shown as full and dashed lines, respectively. The curves are shifted vertically by -1 W/g for each process condition to ease their separation (note that the series order is different than otherwise used in this thesis).
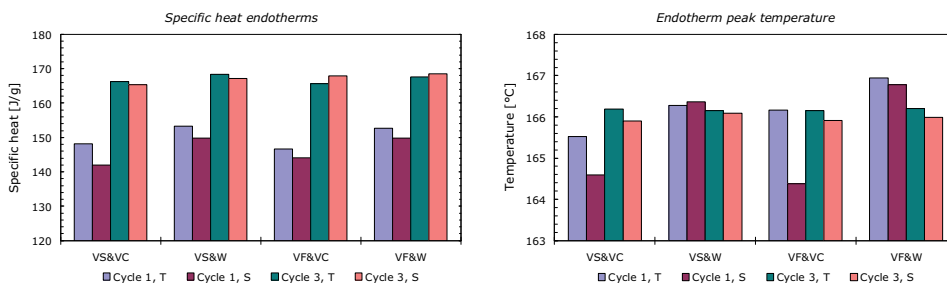
Figure 4.8: Characteristics of DSC heating curves. Cycle 1 is first heating, cycle 3 is second heating. 'T' and 'S' denotes samples of total cross-section and only the outer 0.2 mm, respectively.

4.3. X-ray scattering

In the last stage of the project it was decided to attempt to characterise the texture in the plates from the Impact & Indentation Study by means of X-ray scattering. The scattering pattern of spherulites consists of several complete concentric rings, known as Debye-Scherrer rings. In the case of wide angle x-ray scattering (WAXS), each ring corresponds to different sets of planes in the unit cell. Provided that the oriented outer layers constitutes an adequately high product of extent and crystalline orientation these layers should lead to intensity spots on the rings, when the

29

measurement is made by transmission of the X-ray beam though the thickness of the plate. The technique holds the potential of quantifying the extent of molecular orientation without the need for the tedious, time-extensive and destructive sample preparation required with the PLM technique. With the full plate thickness being irradiated at once the scattering pattern will of course be an integrated measure of the layered microstructure as a whole, meaning that a thin but highly oriented skin layer all other same will yield the same scattering pattern as a thicker but less oriented layer. Moreover, the signal-to-noise ratio of the orientation will depend on the relative amount of the spherulitic core (containing lamellae of all orientations), which forms the underlying Debye-Scherrer rings. These inexpediencies could have been circumvented by irradiating through microtomed thin sections of the plate cross-section, allowing thereby measurements of the individual layers of the microstructure. Such an approach requires, however, a microfocus X-ray beam for good spatial resolution, meaning that the measurements would have to be made at a synchrotron beam line (e.g. the European Synchrotron Radiation Facility in Grenoble, France). This was out of the question at this stage in the project. The chosen more simple approach, using a rotating anode with Cu-target as X-ray source, may also be seen as being more relevant to NNAS, since such instruments are commercially available and thus potentially could be acquired for fast and non-destructive material analysis of this kind in the department.

Both wide and small-angle X-ray scattering (WAXS and SAXS, respectively) were obtained from the position shown in Figure 4.9, at the Polymer X-ray facility at Risø DTU in Roskilde, Denmark. Senior Scientist at the facility, Jens Wenzel Andreasen, operated the instruments, and helped with the data reduction and interpretation, together with Professor Kell Mortensen from the Biophysics Group at the Faculty of Life Sciences, University of Copenhagen. Because X-ray analysis was included in the project at such a late stage the experiments and data analysis have not been brought to end at the time of writing of this thesis. Further work is planned before a final evaluation of the technique for this use, but the results and discussion presented here does reveal how it may provide for a fast quantification of orientation and characteristics of crystalline features, which is of great relevance and interest to the department in NNAS.
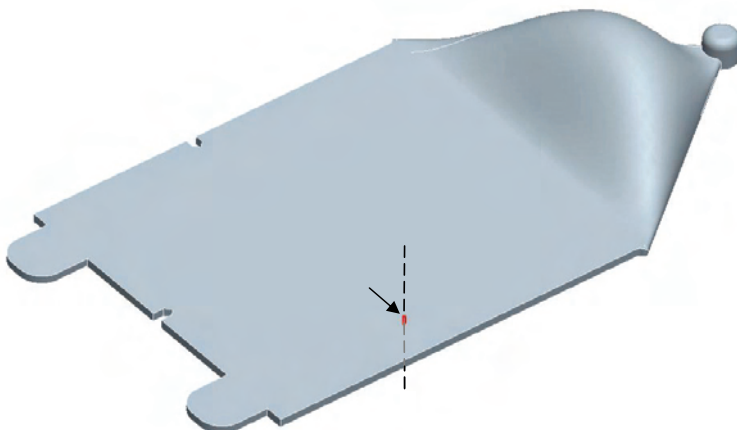

Figure 4.9: Approximate position of X-ray irradiation of test blanks.

4.3.1. Wide angle X-ray scattering

WAXS provides information on the most highly scattering structural features, i.e. those with smallest length scale. In POM these are the characteristics of a hexagonal unit cell [35].

The WAXS X-ray source was operated at 50 kV, 200 mA and provides a CuK$_\alpha$-filtered (1.5418 Å) X-ray beam of 0.4×0.4 mm^2 focus. The sample to detector distance was 122 mm. The samples were oriented with the flow direction (FD) vertical and measurements were made with exposure times between 46-112 minutes. Examples from VS&VC and VF&W process conditions are shown in Figure 4.10 (both of ~46 min. exposure time). No clear differences in the positions of the Debye-Scherrer rings are seen, implying that the crystalline unit cell is largely unaffected by the varied process conditions.
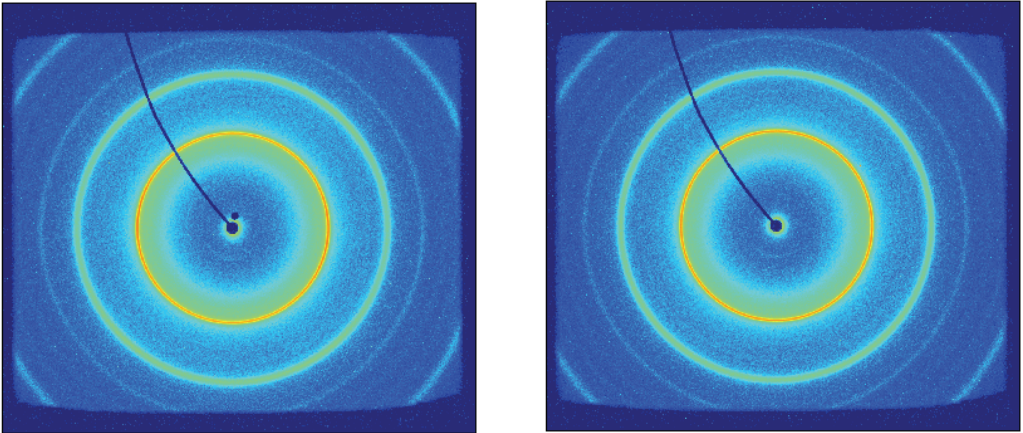
Figure 4.10: WAXS images from the VS&VC (left) and VF&W (right) process conditions. The melt flow direction of the plate is oriented vertically. The extra dark spot in the left image near the centre is related to the image plate used for that specimen, not to the specimen itself.

The scattering angle 2θ of the two inner rings (yellow and thick light blue ring) were measured to be 23° and 34°, respectively. The corresponding interplanar spacing d of the unit cell may be calculated from the Bragg equation for scattering of the first order:

$$\lambda = 2d \sin \theta \qquad \qquad \text{Equation 3}$$

where λ is the wave length of the X-rays. The corresponding d-spacings are 3.9 and 2.6 Å, respectively. According to Kawaguchi [44] the former refers to the (100) planes of the hexagonal unit cell[A]. Scattering spots at this spacing may be used to quantify the crystalline orientation of the outer layers [35;44]. The shorter spacing have not been checked against the databases but could possibly be from (105) planes, a plane direction that intersects with the backbone direction **c**. Figure 4.11 show the exposure time-normalised intensity of the inner ring (3.9 Å) against the azimuth angle (the tangential coordinate) for the four process conditions. The intensity as acquired with the image plates have been integrated radially to encompass the broadness of the ring. Unit cell orientation is clearly seen for all process conditions as peaks around ±90°, corresponding to alignment of the **c**-axis helix direction with the flow direction. Process conditions VS&VC clearly has the highest degree of accumulated orientation, in agreement with the very thick δ-layer found in

---

[A] (100) in Miller notation, used by Kawaguchi, is equivalent (10$\underline{1}$0) in Miller-Bravais notation, used by Bowman.

the PLM investigation in chapter 4.1. The high birefringence of the thin skin layer of the VF&W specimen is not manifested in this through-thickness averaged orientation measure. A hump is seen in this curve between the two primary peaks. The implications of this feature has not yet been accounted for. The azimuthal intensity distribution of the Debye-Scherrer ring corresponding to $d = 2.6$ Å is shown in Figure 4.13, revealing also scattering spots from this lower spacing. Again, highest intensity is seen for the VS&VC process condition. Under the assumption that this spacing corresponds to a plane that intersects the **c**-axis, maxima angles for $d = 2.6$ Å is expected elsewhere than the maxima angles for $d = 3.8$ Å, in agreement with the observation.
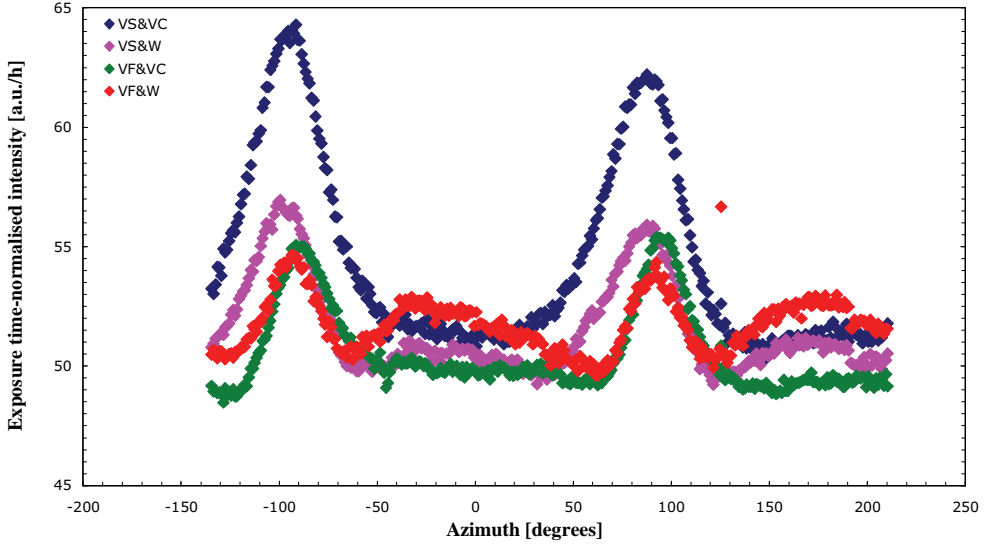
Figure 4.11: Azimuthal plot of WAXS intensity for scattering at $d = 3.9$Å for the four process conditions.

The orientation may be quantified by a single measure through the Herman orientation function [45] and the second-order orientation factor [46]. The former is given by

$$f_H = \frac{3\langle \cos^2 \phi \rangle - 1}{2}$$

Equation 4

where

$$\langle \cos^2 \phi \rangle = \frac{\int_0^\pi I(\phi) \cos^2 \phi \sin \phi \, d\phi}{\int_0^\pi I(\phi) \sin \phi \, d\phi}$$

Equation 5

and $I(\phi)$ is the intensity at the first-order peak position (here $d = 3.9$Å) as function of the azimuthal angle. For $\pm 90°$ orientation the second-order orientation factor may simply be found as

$$F_2 = -2 \cdot f_H .$$

Equation 6

The factor evaluates to unity if all lamellae are oriented with the normal parallel to the reference direction.

Figure 4.12 shows the second-order orientation factor for the four process settings. The data were evaluated relative to the individual peak orientation angles, i.e. with the reference direction adjusted to account for the slight differences in azimuthal peak positions (as described in 4.3.2). The accumulated orientation is found to be more than a factor of 11 higher in the VS&VC sample than in the VF&W sample. This ratio is expected to be reflected in the amount of mechanical anisotropy to some extent. The very slow injection into a warm mould is seen to yield roughly the same amount of accumulated orientation in the flow direction as the very fast injection into a cold mould.
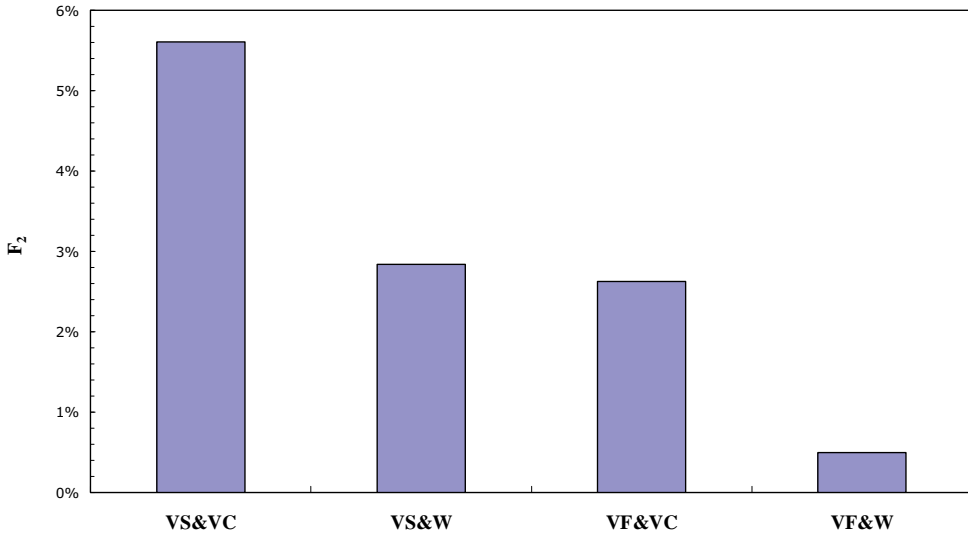
Figure 4.12: Second-order orientation factor for the four process settings.

4.3.2. Small angle X-ray scattering

Where WAXS measured scattering related to the length scale of the unit cell, SAXS measures scattering from repeat distances of up to ~150 nm. SAXS may therefore be used to measure both lamellar orientation and interlamellar spacing in semi-crystalline polymers.

The SAXS X-ray source was operated at 60 kV, 60 mA and provides a CuK_α-filtered (1.5418 Å) X-ray beam of 1×1 mm^2 focus. The sample to detector distance was 1509 mm. The samples were oriented with the flow direction (FD) horizontal (i.e. rotated 90° compared to the WAXS measurements) and irradiated for one hour each. Examples from the VS&VC and VF&W process conditions are shown in Figure 4.14. The more pronounced scattering spots of the former specimen implies a higher extent of orientation, as also found from the WAXS measurements. The horizontal positions of the spots indicates a spacing in the flow direction of the plate. This is consistent with the interlamellar spacing in a stacked lamellar structure with the lamella normal parallel to the flow direction. The absence of a streak in the vertical direction suggests little or no amount of shish-kebab-like structure [47].
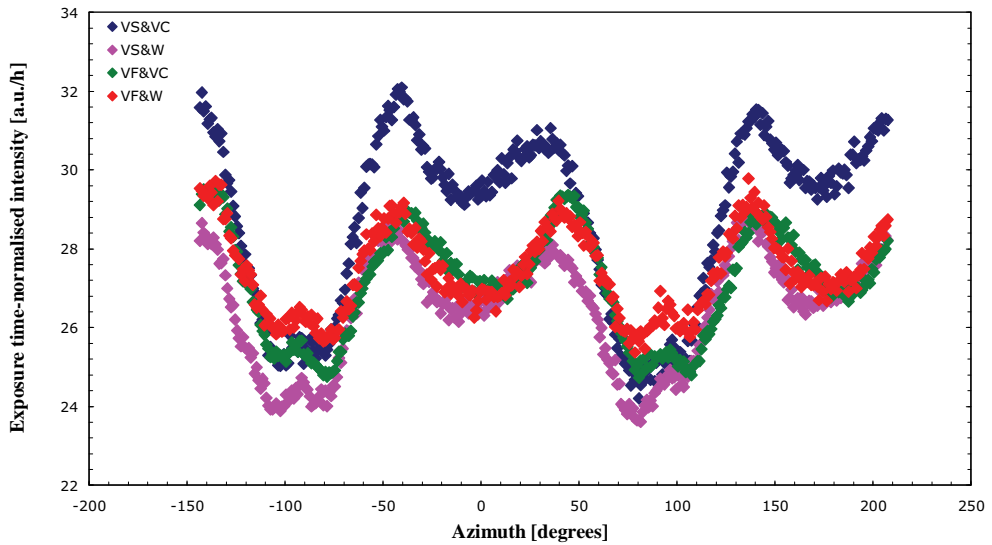
Figure 4.13: Azimuthal plot of WAXS intensity for scattering at $d = 2.6$ Å for the four process conditions.
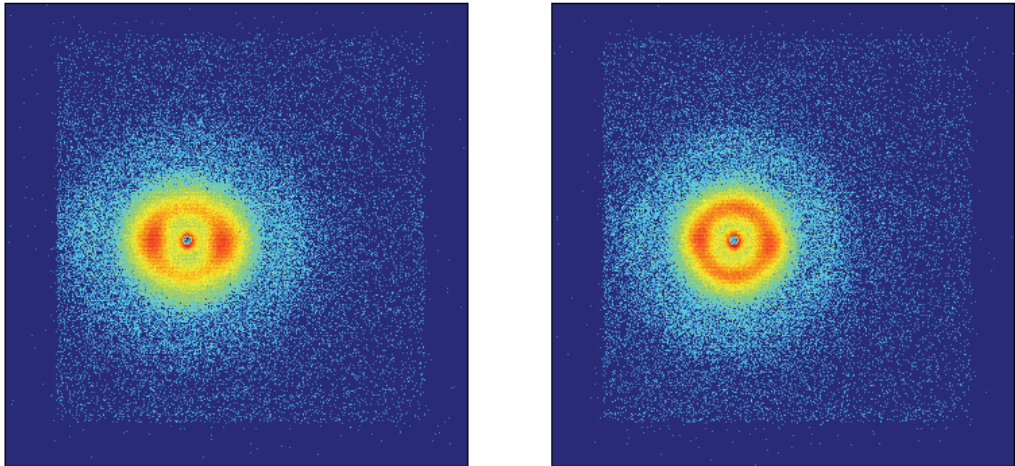
Figure 4.14: SAXS images showing log intensity from the VS&VC (left) and VF&W (right) process conditions. The melt flow direction of the plate is oriented horizontally.

Figure 4.15 shows the intensity integrated over the full azimuthal range (0-360°) vs. the reciprocal spacing q defined as:

$$q = \frac{2\pi}{d}$$

Equation 7

The peak around $q \approx 0.5$ nm^{-1} corresponds to scattering from a d-spacing of 14.3 nm, which presumably is the periodic spacing of the lamellae in the spherulites in the core. This is consistent

with highest and lowest peak intensities found for process conditions VF&W and VS&VC, respectively, since these two were found in the PLM investigation to represent lowest and highest thicknesses of the skin and δ-layers. At lower *d*-spacings (higher *q* values) a pronounced difference is seen between the process conditions of low and high mould temperature. The high mould temperature clearly leads to lamella thickening in the δ-layer, as would be expected. The hump in the curves around $q = 1.1\text{-}1.4$ nm^{-1} might represent a primary lamellar thickness in this layer.
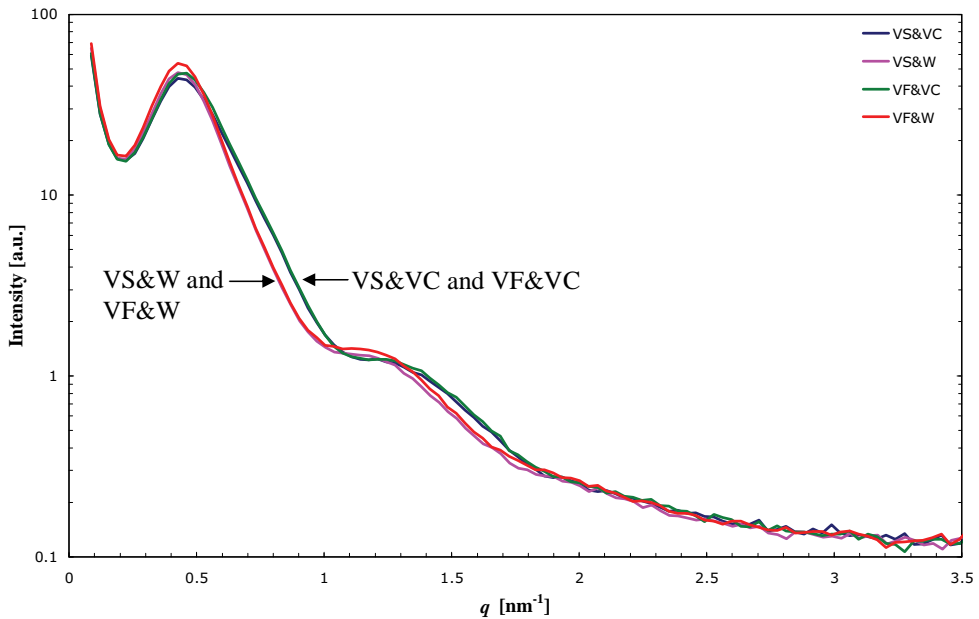
Figure 4.15: Azimuthally integrated intensity of SAXS measurements vs. *q*.

A plot of intensity vs. the azimuthal angle is shown in Figure 4.16, revealing a highest extent of lamellar orientation for the VS&VC process condition. The peak positions are seen to shift approx. ±5° for the different process conditions. The lack of coincidence with the melt flow direction of the specimen (0 and 180°) may be seen as an indication of a lack of perfect straightness of the flow front at this position in the plate of this order of magnitude. If so, this effect is seen to be process dependent as might be expected. Small humps are seen in the curves for the VS&W and VF&W process conditions around ±90° to the primary peaks. Their implications have not yet been accounted for.
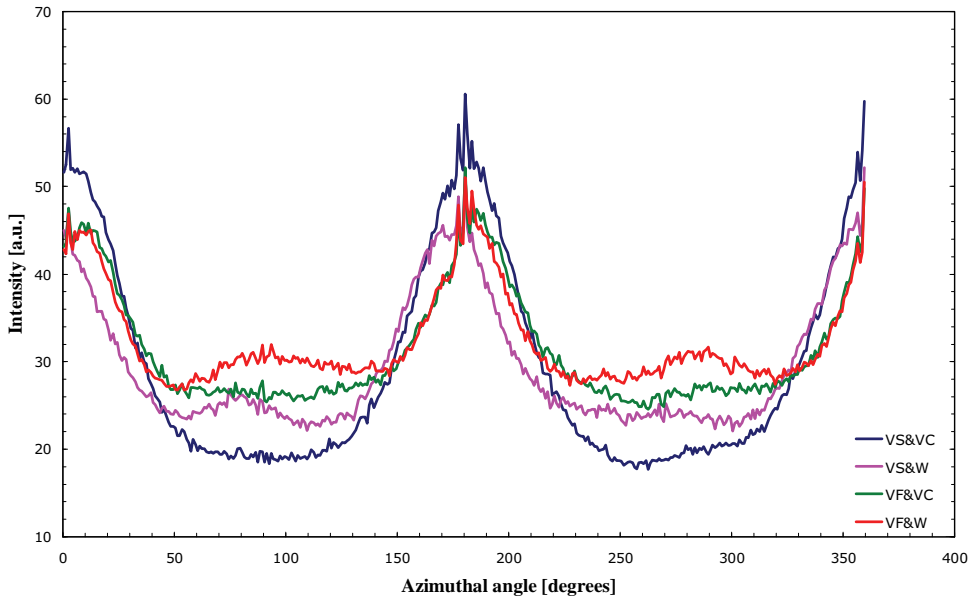
Figure 4.16: Azimuthal plot of SAXS intensity for scattering at d = 14.3 nm, for the four process conditions.

5. IMPACT PROPERTIES OF PLASTICS

This chapter deals with the characterisation of impact behaviour of the injection moulded specimens of both the Additives & Impact Study and the Impact and & Indentation Study. Impact testing represents an extreme loading condition and is used to reveal possible weak structures and zones of reduced coherence in the grades, as caused by the tribological additives and/or varied processing conditions. The chapter takes offset in a description of the theoretical framework related to the testing of performance under impact loading conditions.

5.1. Introduction

A few definitions are required in order to discuss the impact properties of plastics. Fracture may be divided into four categories: Ductile, brittle-ductile, ductile-brittle and brittle. Examples of characteristic force displacement curves are shown in Figure 5.1. Ductile and brittle-ductile fracture (appreciable energy dissipation after onset of crack growth) are outside the scope of this project, since they are irrelevant to the impact behaviour of the grades in focus. In the terminology presented here, the term brittle refers to a linear force-deflection relationship followed by an abrupt drop in force upon onset of unstable crack growth. In the ductile-brittle case the crack growth is preceded by nonlinear behaviour. In general the nonlinearity may stem from nonlinear elasticity, viscoelasticity, slow (sub-critical) crack growth or yielding. Under impact conditions only yielding and nonlinear elasticity are expected to be of relevance. Furthermore, for the POM polymer of this project only yielding is relevant. Assuming small deflections to break under impact flexure (geometrically linear cf. Timoshenko beam theory) we may therefore expect brittle behaviour under such loading in the absence of yielding.
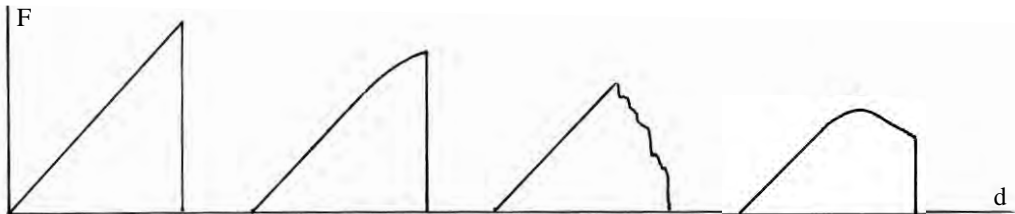
Figure 5.1: Examples of different categories of fracture. Brittle (far left), ductile-brittle (centre left), brittle-ductile (centre right) and ductile (far right).

There are three main factors affecting the degree of yielding: temperature, strain rate and stress state. The effect of temperature will not be discussed here since all experiments have been performed at room temperature where POM is not particularly temperature-sensitive in response[A]. The local strain rate, however, has a major influence on the realised extent of yielding. A high strain rate will lead to a high yield stress and consequently promotes brittle fracture. Both the temperature and strain rate dependence of POM have been thoroughly investigated [49]. The effect of the stress state on fracture behaviour is twofold, with increasing constraint leading to increasing yield stress, but also to a potential transition from shear yielding to craze yielding[B]. Both mechanisms are

---

[A] Hashemi & Williams [48] show the temperature dependence of the yield stress of POM to be balanced by a similar dependence of the brittle fracture parameter K_c (described in chapter 5.4.1).

[B] Crazing in POM is much coarser than in amorphous polymers (below T_g), since the cavitation takes place in an amorphous phase in its rubbery state. Consequently, some references use the term 'microvoiding' rather than crazing for such polymers. In this thesis I have not distinguished between the two terms and use the term crazing also for POM.

relevant to POM and are described in detail in e.g. [50]. The tensile component of hydrostatic stress imposed by typical fracture testing methodologies promotes craze yielding, but both yielding mechanism may well be in play. Depending on the extent of crazing a ductile-brittle or brittle fracture results upon craze breakdown when a certain crack or craze zone size is reached. High constraint and dilatational stress states thus promote brittle fracture. The influence of the yield stress increase on brittle fracture characterisation is described in chapter 5.4.

High impact energies are used in impact testing and the loading of the specimen will effectively be through a prescribed displacement rate and, hence, strain rate evolution. Notched or pre-cracked test specimens are generally used to provide a localisation of the strain through a lowering of the compliance of the ligament (the material behind the notch) compared to the rest of the specimen. The effective strain rate will therefore be much higher than if an unnotched specimen was tested, promoting brittle rather than ductile behaviour as described above. The notch or pre-crack also leads to a higher degree of plastic constraint and thus also promotes brittle fracture through this mechanism.

5.2.   Solutions from elasticity and plasticity theory

The onset of yielding is characterised in terms of the elastic stress field solutions and a yielding criterion – typically the Mohr-Coulomb or modified von Mises criteria for shear yielding. Similar criteria have been proposed for craze yielding, but remains less generally accepted [50]. Also, the complexity of the craze initiation process renders a merely stress or strain-based description less probable for use with general geometries across different microstructural states [39].

The elastic solution to the maximum normal stress for a simple beam in pure three-point bending is (constant elastic modulus over the cross-sectional height w):

$$\sigma_{\max,e} = \frac{3FL}{2bw^2}$$
Equation 8

where F is a central line load, L is the span and b is the specimen thickness. Assuming elastic perfectly-plastic behaviour, then the load at plastic collapse F_{max} (where the ligament is fully yielded) may be found through:

$$\sigma_y = \frac{F_{\max}L}{bw^2}$$
Equation 9

where σ_y is the tensile yield stress. Inserting this into equation 5 shows that the maximum force under these assumptions is 1.5 times the force to cause initial yielding. This relationship is used by Hashemi [51] as a simple means of quantifying the deviation from elastic perfectly-plastic behaviour as caused by e.g. strain hardening.

If a test specimen is notched with a blunt notch then equation 5 may be used in conjunction with the stress concentration factor of the notch to give the normal stress in the notch root at fracture initiation[A]. Stress concentration factors for standard geometries are given in the literature, but may be estimated by approximating the notch to an ellipse using the Neuber-Inglis solution[B]:

[A] Finite element modelling is generally used for the more complex geometries of real components.
[B] Note that this solution relates the max. stress to the gross stress away from the crack. Some references relate the stress concentration factor to the net stress, i.e. with *(w-a)* instead of *w* in equation 5.

$$\sigma_{\max} = \sigma_{gross}\left[1 + 2\sqrt{a/\rho}\right]$$
<div align="right">Equation 10</div>

where a and ρ are the depth and tip radius of the notch, respectively. This is the general engineering approach to describe the onset of ductile failure. The characterisation of behaviour under impact conditions will, however, generally lie beyond the limits of this approach, and consequently have been dealt with through different frameworks; either the traditional impact strength measures or the concept of fracture mechanics.

5.3.   Traditional impact testing methods: Charpy, Izod and Gardner tests

Traditionally, impact testing of polymers (and other materials in general) have been by means of either beam flexure, like Charpy and Izod testing, or falling dart plate perforation tests. In their original, non-instrumented forms the Charpy and Izod tests are a measure of the total amount of energy removed from a swinging pendulum during fracture of a bluntly notched beam specimen (unnotched specimens may also be used). The energy is normalised by the ligament cross-section to provide the Charpy or Izod impact strength. The Charpy method uses a beam in three-point bending, whereas the Izod method is based on a cantilever beam. For materials failing by brittle or ductile-brittle fracture (cf. chapter 5.1) the total energy measure will relate to the onset of crack growth. For a ductile or brittle-ductile failure, however, the total energy will not be directly related to this loss of mechanical integrity, which is often what is sought. For uninstrumented testing an examination of the characteristics of the fracture surface ("fractography") was therefore needed to determine what type of fracture the impact strength was a measure of. Instrumentation of impact testers have obviated this need by providing direct measurement of the force vs. time response, from which the failure point and type of failure can be determined. Modern standardised fracture mechanical impact testing (described in chapter 5.5.1) is often based on the Charpy setup [52].

Falling dart impact testing with perforation of a plate specimen has also been widely used. The original form (the Gardner impact test) is based on a statistical evaluation of the probability of fracture (Weibull statistics), rather than a characterisation of the condition leading thereto. Modern plate puncture impact testing is based on instrumentation of the falling dart, but friction between striker and plate may lead to less generic information about the material than can be derived from beam flexure or tensile impact tests. The falling dart impact test furthermore does not allow for the assessment of mechanical anisotropy, since the measured behaviour is a combined result of the properties in both directions of the plate. The biaxial tensile stress state may however be highly relevant for certain applications like packaging foils, sheets and some shell structures. Some components in the injection devices made at NNAS are indeed shell structures, but unexpected brittle fractures are generally not seen in these components. To my knowledge from the failure cases I have been presented to during my last three years of affiliation with the company, brittle fracture of components in devices under development occur primarily under high rate beam bending. Therefore, although it would be clear-cut to impact test the injection moulded plate specimens by falling dart impact in this project, it was decided not to use this testing approach. Instead, an instrumented Charpy-type setup have been used, as it complies with the methodology of fracture mechanics described in the following.

5.4. Fracture Mechanics in relation to plastics

The stress concentration resulting from a notch was given in 5.2. From this expression follows that a stress singularity results from a notch tip radius of zero. The severity of a sharp crack may therefore not be described merely in terms of a stress concentration and the concept of fracture mechanics must be invoked to handle this case.

5.4.1. Linear elastic fracture mechanics

Two fracture property measures from linear elastic fracture mechanics (LEFM) are of interest: The critical strain energy release rate G_c and the critical stress intensity factor K_c. The former relates to the energy to cause crack growth initiation, the latter to the force required for same event.

The strain energy release rate G is defined as the rate of energy released by crack growth:

$$G \equiv \frac{dU}{b \cdot da} \qquad \text{Equation 11}$$

where b is the specimen thickness, a is the crack length and U is the difference between the work by external forces and the elastically bound strain energy. The critical strain energy release rate G_c of a material may in praxis be found from the measured (or derived) energy through:

$$G_c = \frac{U}{bw\varphi(a/w)} \qquad \text{Equation 12}$$

where U is the energy leading to fracture initiation, w is the specimen width and φ is an energy calibration factor depending on how the compliance C changes with the relative crack length a/w:

$$\varphi(a/w) = \frac{1}{C}\frac{dC}{d(a/w)} \qquad \text{Equation 13}$$

The stress intensity factor K can be seen as a measure of the stress gradient at the singularity of an ideal crack. From the elastic stress field at the crack tip, K is defined as:

$$K \equiv \lim_{r \to 0} \sigma(r)\sqrt{2\pi r} \qquad \text{Equation 14}$$

where σ is the normal stress perpendicular to the crack face at a distance r from the crack tip. The critical stress intensity factor K_c of a material is evaluated from the measured force at crack growth initiation F via:

$$K_c = f(a/w)\frac{F}{b\sqrt{w}} \qquad \text{Equation 15}$$

where $f(a/w)$ is a geometry calibration factor, accounting for the finite dimensions of the specimen. The expression for the geometry calibration factor for the SENB geometry is given by e.g. Williams [52], together with the expression for the energy calibration factor for G_c determination.

The value of G_c or K_c determined in a fracture test depends on the effective stress state at the crack tip of the specimen. In a thin specimen, or at the surface of a thick specimen, the stress state will be one of plane stress. In the centre of a thick specimen the stress state will be plane strain. Plane stress leads to a low yield stress, resulting in a large plastic zone. The higher constraint of plane strain leads to a higher yield stress and a smaller plastic zone at the crack tip. The measured fracture parameter will consequently be high for a thin specimen and decrease as the thickness increases. If the specimen is adequately thick the determined value will represent the lower-bound plain strain value of the material, denoted G_{Ic} and K_{Ic}, respectively. The size requirement to ensure this is:

$$\left.\begin{array}{l} b \\ a \\ (w-a) \end{array}\right] > 2.5\left(\frac{K_{Ic}}{\sigma_y}\right)^2 \qquad\qquad \text{Equation 16}$$

When b does not fulfil this inequality, the value obtained will depend on the geometry of the specimen, whereas the plain strain value is a true material parameter. The test of the crack length a and the ligament width $(w-a)$ against the same requirement ensures that the occurrence of crack tip yielding does not affect the elastic stress field distribution, i.e. that only small-scale yielding occurs [53].

K and G are for the elastic case related through:

$$G_c = \frac{K_c^{\ 2}}{E'} \qquad\qquad \text{Equation 17}$$

where E' is the modulus of elasticity determined under similar conditions as K and G, both in terms of loading time and stress state. For the case of plain stress E' is therefore simply the elastic modulus E from unidirectional tensile testing at a similar strain rate, but for plane strain E must be adjusted for the increased constraint through:

$$E' = \frac{E}{1-v^2} \qquad\qquad \text{Equation 18}$$

where v is Poisson's ratio. E' is related to the stiffness S of the tested specimen through:

$$E' = \frac{2f^2\varphi S}{b} \qquad\qquad \text{Equation 19}$$

by which a cross-check on G and K may be made.

From the definition of K_c follows that there is a lower limit on the flaw size from which brittle fracture can occur in a material behaving linear elastically up to fracture initiation:

$$a_c = \frac{1}{\pi}\left(\frac{K_c}{\sigma_y}\right)^2 \qquad\qquad \text{Equation 20}$$

When the thickness requirement is not fulfilled by the tested specimen the plasticity at the crack tip may not be negligible and the elastic stress field solution will not alone determine the point of crack growth initiation. For such cases, which are relevant for many polymers under realistic thicknesses, elastic-plastic fracture mechanics will be needed.

5.4.2. Elastic-plastic fracture mechanics

In LEFM all the energy put into the specimen was assumed to be available for crack growth. When more extensive plastic deformation takes place the analysis needs to account for the dissipated energy. Two approaches to elastic-plastic fracture mechanics are widely used for plastics: the *J*-integral approach and the concept of the essential work of fracture [54]. The latter is used for thin films under full plastic yielding and is not relevant to impact fracture testing.

The *J*-integral fracture parameter is a measure of energy per unit cross-sectional area of the ligament. The definition of *J* as a path-independent contour integral is given by e.g. Williams *et al.* [54] and compares to the strain energy release rate *G* for a non-linear elastic solid under monotonic loading. Plati & Williams [55] give an expression for the critical *J*-integral value *J*$_c$ that is applicable for all degrees of plasticity:

$$J_c = \sigma_y \cdot CTOD \hspace{10cm} \text{Equation 21}$$

where *CTOD* is the crack tip opening displacement at crack growth initiation. *CTOD* at crack growth initiation is, however, not easily determined (especially not under impact conditions) and J_c is in praxis found from energy-based expressions derived under different assumptions. The simplest is that of Rice, Paris & Merkle [56]:

$$J_c = \eta \frac{U_{tot,cor}}{B(W-a)} \hspace{10cm} \text{Equation 22}$$

where η is a calibration factor and $U_{tot,cor}$ is the total flexure energy of the specimen. For SENB specimens with $a/w \approx 0.5$ the calibration factor η is 2. The expression has been derived assuming full-ligament yielding of an elastic-perfectly plastic solid. Strictly speaking it is therefore only appropriate for ductile-brittle fractures. Equation 19 has been widely used regardless of this to characterise also brittle fractures where the LEFM size requirements may not be met for valid G_{Ic} determination [57-59]. In such cases the *J*-value may simply be seen as a normalised measure of the energy absorbed at crack growth initiation. Other *J* expressions divide the energy into elastic and plastic contributions (e.g. the expression of Sumpter & Turner [60]), but the formula given here remains widely used due to its simplicity and robustness [61]. For the linear elastic case $J_c = G_c$.

As in the case of LEFM a size criteria needs to be met for the obtained value of J_c to represent the lower bound of plane strain. The validity criteria for the specimen thickness is given in [52] to be:

$$b > 25 \frac{J_c}{\sigma_y} \hspace{10cm} \text{Equation 23}$$

which is about a factor of five less strict than the LEFM criterion.

5.4.3. Test specimen geometry

Many different test specimen geometries have been used in fracture mechanical testing of plastics [50]. The single-edge notched beam (SENB) and compact tension (CT) geometries are widely used for fracture mechanical impact testing of plastics (excluding laminated composites, which are typically evaluated through the double cantilever beam geometry). Both are supported by the LEFM standards from ASTM and ISO. The SENB geometry is used with falling weight or pendulum impact testers, typically in a three-point bending setup similar to that of Charpy impact testing. The CT geometry is used with tensile testing machines (the single and double edge notched tensile geometry, SENT and DENT, respectively, are also frequently used for such setups). I chose the SENB geometry for this project, because a falling weight impact tester came at my disposal early in the project. The tester is described in appendix 11.2. In combination with three-point bending of specimens machined from the injection moulded test blanks, this setup provided impact mechanical characterisation on the same mouldings as used for the tribological evaluation.

5.4.4. Standardised quasi-static LEFM testing – ISO 13586

Several standards for LEFM testing of plastics under quasi-static conditions have been developed. ASTM D5045 and ISO 13586 are in large identical and describe the practical procedures for obtaining G_{Ic} and K_{Ic} under displacement rates where dynamic effects are negligible. Certain geometrical proportions for the specimens are given in the standards, which ensure that all size requirements are met if the thickness is found adequate for plain strain to prevail (equation 13). ISO 13586 forms the basis for the ISO 17281 standard, which was used for the impact testing made in this project – see chapter 5.5.1.

5.4.5. TC4 protocol for J-integral determination

There is no standardised procedure for *J*-integral testing of plastics under impact conditions, but the Technical Committee 4 (TC4 - Polymers, Adhesives and Composites) under the European Structural Integrity Society (ESIS) has made a protocol based on the *J*-R-curve concept (R referring to crack growth resistance). This approach is required for ductile and brittle-ductile fractures, where appreciable energy is dissipated during crack growth and hence renders a clear determination of the onset of crack growth difficult. The procedure involves the loading of specimens to different amounts of crack growth and subsequent measurement of the crack extension via fractography. *J* is calculated for each specimen through equation 19 and plotted against the corresponding extension of the crack, i.e. as $J(\Delta a)$. A power-law fit of the data is made and the initiation toughness J_c is defined from the arbitrary crack extension $\Delta a = 0.2$ mm. For the case of ductile-brittle fracture J_c may simply be found from equation 19.

5.5. Impact fracture mechanical testing

It is generally agreed that above impact velocities of 1 m/s the load signal contains too large inertial components for a direct evaluation of the crack growth initiation to be possible [52]. For testing rates up to 1 m/s the dynamic effects may be controlled and special procedures of data analysis allow for determination of the critical values of *G* and *K*. For the time being only ISO has a standard describing such measurements and analyses for plastics – ISO 17281.

TC4 under ESIS have also made a protocol for *J*-fracture toughness testing under impact conditions [52]. The protocol is based on the same basic procedure as the protocol for slow rate testing but is still in the state of a draft.

5.5.1. The standardised approach to LEFM impact testing – ISO 17281

ISO 17281 is the standardisation of a protocol developed by TC4. The purpose of the standard is to determine G_{Ic} and/or K_{Ic} for plastics under moderately high impact velocities – up to 1 m/s. The standard supports the SENB geometry under certain aspect ratios, tested in three-point bending (the Charpy setup). The test is based on specimens where a milled sharp notch has been sharpened further into a pre-crack by means of a razor blade. Five specimens with total crack lengths *a* (notch and pre-crack) in the range of $a/w = 0.45\text{-}0.55$ are used to determine K_{Ic}. G_{Ic} may be determined through tests of additionally six specimens with $a/w = 0.20\text{-}0.45$ and four specimens with $a/w = 0.55\text{-}0.70$. The specimens are fractured under a prescribed displacement rate of up to 1 m/s with recording of force, time and (derived) energy. Force oscillations from the initial contact may be dampened by means of a soft pad placed where the striker hits the specimen. The measured force trace is curve fitted according to a special procedure and checked for linearity (contained oscillations – see Figure 5.2). A certain definition is used to characterise the force at crack growth initiation F_Q from this curve and a provisional value of the critical stress intensity factor is found using equation 12. If the size requirement of equation 13 is fulfilled, the value is regarded as the lower-limit plain strain value K_{Ic}. Note that the evaluation of the size requirement involves an assessment of the yield stress under a similar time-to-yield as the time-to-fracture of the impact tests. High speed tensile testing may be used, but extrapolation from slow-rate data is also permitted by the standard.
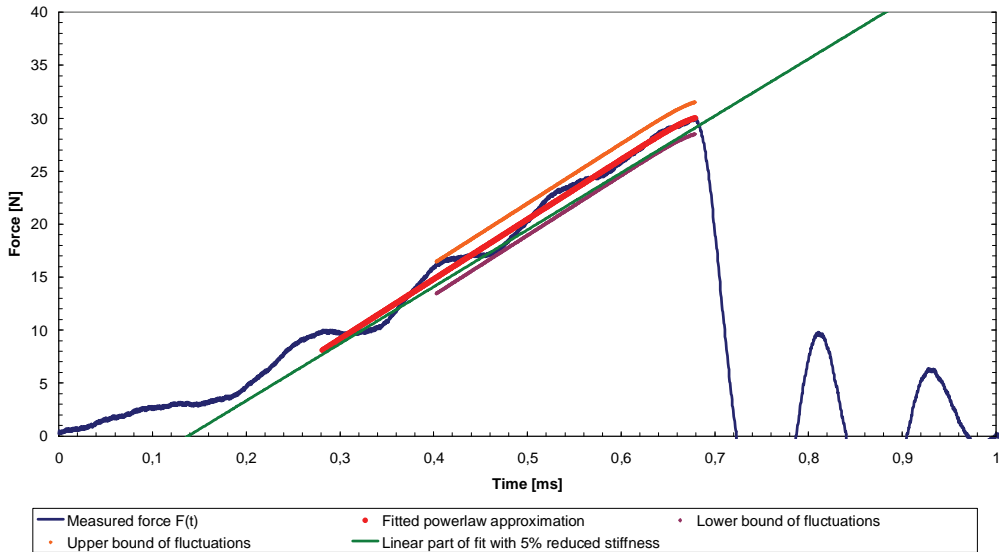
Figure 5.2: Example of curve fit and limits of permissible force fluctuations (data from VS&VC-FD specimen with pre-crack).

The direct determination of G_{Ic} (i.e. without using equation 14) requires a correction of the derived energy data, which are in excess of the deflection from damping pad compression, indentation of support and striker into the specimen, and kinetic and inertial loads. F_Q is determined for each of the specimens with the K_{Ic} evaluation procedure described above. The energy absorbed up to F_Q is corrected through a separate energy correction test (ECT), giving the contributions from damping pad and indentation. The ECT consists of an impact test on an unnotched specimen (including damper) with closely positioned supports using a special test rig. The ECT energy at F_Q for each specimen is subtracted from that of the fracture test and the value is plotted against the product $bw\varphi$ as in equation 9. The slope of a linear regression of the at least fifteen points yields G_{Ic}.

5.6. Literature data
5.6.1. Fracture properties of POM

Two main authors have reported on the fracture properties of the copolymer POM grade used in this project: S. Hashemi from School of Polymer Technology at the University of North London, England, and K.L. Lam from the Engineering Campus at Universiti Sains Malaysia. Both have investigated the fracture properties of structural composites based on POM, but also report on the unfilled grade itself. Their findings are summarised in Table 7 and were taken as point of departure for my investigations.

The effect of notch radius is clearly reflected in the K_c data from Hashemi *et al.* [62]. In this reference data is also reported on the strain rate dependence of the tensile yield strength, indicating a minimum specimen thickness b for valid plain strain testing of 9 mm in the case of quasi-static loading. Crudely estimating the rate effect from the two tests with 0.25 mm notch radius, a K_c value of around 3.3 MPa√m may be expected for the present 1.5 mm specimens under a loading rate of 1 m/s. The impact rate G_c value reported in Hashemi *et al.* [63] may not directly be compared to the

K_c values, since it was obtained without ECT correction and thus refers to the total absorbed energy. The true value may therefore be expected to be somewhat lower. Estimating a G_c value based on the K_c of 3.3 MPa√m, the slow rate modulus of elasticity from the same reference and equation 14 yields $G_c = 4.8$ kJ/m^2 (Plummer et al. [49] finds E to be insensitive to strain rate around room temperature). This is similar to the values of G_c and J_c for other copolymer POM grades reported by Chang & Yang [64] and Kumar et al. [65], respectively – see Table 8. The remarkable rate dependence of K_c reported by Lam et al. [66] is not consistent with the results from the other references and may well be a result of the microstructure of their compression moulded specimens.

Table 7: Referenced fracture properties for Ticona Hostaform C9021 at room temperature.

Reference	Moulding method*	Geometry	b [mm]	Notch radius [mm]	Speed [mm/s]	K_c [MPa√m]	G_c / Charpy / Izod [kJ/m^2]
Hashemi et al. [62]	IM	SENB	4	Razor sharp	0.083	4.22	
	IM	SENB	4	0.25	0.083	5.27	
	IM	SENB	4	1	0.083	5.80	
	IM	SENT	1.5	Razor sharp	0.083	3.75	
	IM	SENB	4	0.25	0.83×10^3	4.9	
Hashemi et al. [51]	IM	SENB	4	Razor sharp	0.083	4.28	
	IM	beam	4	N/A	3×10^3		121 (UN Charpy[†])
Hashemi et al. [63]	IM	SENB	4	Razor sharp	0.083	4.31	
	IM	SENB	4	Razor sharp	3×10^3		14.4 (G_c)
Lam et al. [42]	IM	SENB	3.175	0.254	3×10^3		16.5 (Izod[‡])
	CM	SENT	3	Razor sharp	0.017	6.5	
Lam et al. [66]	CM	SENT	3	Razor sharp	1.7	5.7	
	CM	SENT	3	Razor sharp	8.3	1.6	
Ticona	IM	SENB	4	0.25	3×10^3		6.5 (Charpy[§])
	IM	beam	4	N/A	3×10^3		180 (UN Charpy[†])

* IM = injection moulding, CM = compression moulding. [†] Unnotched Charpy test on 4×10 mm^2 cross-section cf. ISO 179. [‡] Notched Izod on 3.175×12.7 mm^2 cross-section cf. ASTM D256. [§] Notched Charpy cf. ISO 179.

Table 8: Referenced fracture properties for other copolymer POM grades at room temperature.

Reference	Grade	Moulding method*	b [mm]	Notch radius [mm]	Speed [mm/s]	K_c [MPa√m]	G_c / J_c Charpy / Izod
Chang & Yang [64]	Celcon M90*	IM	3.175	0.127	3×10^3		5.2 kJ/m^2 (G_c)
	Celcon M90*	IM	3.175	0.254	3×10^3		73 J/m (Izod)
Kumar et al. [65]	Celcon M140*	IM	5	Razor sharp	0.083		4.8 kJ/m^2 (J_c)
Lazzeri et al. [67]	Nyltech M2[†]	IM	6	Razor sharp		4.86	
	Nyltech M5[†]	IM	6	Razor sharp		4.05	
Mehrabzadeh & Rezaie [68]	Lucel N109-02[‡]	CM	3.175	0.254	(3×10^3)		26 J/m (Izod)
Uthaman et al. [69;70]	Celcon M90*	IM	3.175	0.254	(3×10^3)		70 J/m (Izod)
Kawaguchi & Tajima [71]	N/A	IM	4	0.25	(3×10^3)		6 kJ/m^2 (Charpy)

* Celcon is the old trade name for copolymer POM from Celanese. Celcon is now distributed through Ticona, formerly Hoechst AG, alongside Hostaform, which is still used as trade name despite that Celanese now owns Ticona. According to their data sheets, Celcon M90 and Hostaform C9021 has the same mechanical properties. Celcon M140 is a grade with improved melt flow.
[†] Nyltech M2 and M5 – these grades are unknown to me. Their weight average molecular weights are found in the reference to be 143,500 and 61,200 g/mol, respectively.
[‡] Lucel is the POM-C tradename from LG Chemicals. Grade N109-02 is a general purpose grade with MFI comparable to Hostaform C9021.

5.6.2. Processing effects and anisotropy

Chapter 4 showed how the processing conditions may affect the microstructure, morphology and molecular orientation of injection moulded plastic. The corresponding influence on the fracture and impact properties of POM have been addressed by Wright *et al.* and Viana for homopolymer grades.

Wright *et al.* [36] describe a dramatic increase in falling dart impact strength (maximum force and total energy uptake) from using a combination of low melt temperature and a very high mould temperature (130°C). Very little information is given about the experimental setup, but the degree of crystallinity as estimated through DSC measurements was found not to directly correlate with the change in impact strength. The spherulite size and skin layer thickness (supposedly the δ-thickness cf. chapter 4.1) were both found to be lowest for the strongest specimen, but the design of experiment is too sparse for a general conclusion to be drawn.

Viana [9] describes the change in slow-rate K_c of a 1.5 mm thick POM plate processed under two different melt temperatures and injection rates. The mould temperature is kept constant and low (40°C). Highest fracture toughness is found for a high melt temperature and slow injection rate. This conclusion is found irrespective of the loading direction, the effect of which is found to depend on the process conditions. A strong increase in anisotropy is found with increasing injection melt flow. Values of K_c in the range of 4.4-13.2 MPa√m are reported, depending on the process conditions and loading direction, the largest effect being of the former. Viana expects K_c to correlate positively with degree of crystallinity, δ-layer thickness and level of molecular orientation.

Bowman [35] finds increasing barrel temperature to decrease the yield stress, contrary to what would be expected from the increasing crystallinity and lamella thickness. The effect is attributed to the lower δ-thickness. The yield stress in the flow direction is found to be lower than in the transverse direction, and a change in fracture initiation site from the core of the moulding, to the skin layer when loaded transverse to the flow direction is also reported. The fracture surfaces from the latter case are also found to be much smoother.

The δ-layer may potentially have a large influence on the mechanical properties of the moulding, as suggested by the characteristics found in chapter 4. This is especially so for thin injection mouldings, where the outer microstructural layers may constitute a large relative amount of the specimen thickness. An effect of processing conditions may not be seen at all if the thickness of the test specimen moulding is high. This is made clear by comparing the study on injection moulded plates of PP of Cunha & Pouzada [38] with the similar study of Karger-Kocsis *et al.* [72]. Cunha & Pouzada reports a significant process dependence of falling dart impact strength for plates of 1.5 mm thickness. The impact performance is found to correlate with the relative extent of the δ-layer. Karger-Kocsis *et al.* finds only marginal effects of the δ-layer from impacting of plates of 4 mm thickness. This highlights the need for impact mechanical evaluation on test specimens of component-realistic thickness. The influence of the flow-oriented layers is also reported by Schrauwen *et al.* [73], as varied by varying the thickness of the moulding.

Chiang & Lo [74] investigated a compression moulded copolymer POM and reported less than 25% increase in notched Izod impact strength when increasing the cooling rate by a factor of 70. Compression moulding being a shear-less process, this result suggests impact strength to be rather insensitive to the mere temperature gradient-induced changes in skin layer thickness, spherulite size and degree of crystallinity. This is in agreement with the conclusion from Wright *et al.* [36]. As

indicated before, however, the processing effects in injection moulded plastics include also flow-induced changes like degree of skin layer orientation and shear-induced crystallisation. This underlines the importance of using test specimens processed under conditions similar to the manufacturing process of the real components for which the material is to be used.

In conclusion, we may expect the thick skin layer of specimen from process setting VS&VC to provide the highest impact strength and toughness among the specimens, when loaded in the flow direction.

5.7. The Additives & Impact Study – impact testing
5.7.1. Introduction

The impact testing part of the Additives & Impact Study was conducted in an attempt to shed light on the extent of deterioration in impact fracture performance from the admixture of the two additives, PDMS and PTFE, under the varied mould temperature and injection melt flow. The impact testing setup is described in appendix 11.2 and is based on three-point bending of SENB specimens (an instrumented Charpy setup). A milled notch was chosen as stress raiser for the specimens in this study. A sharp pre-crack was thought to be less sensitive to differences in level of inherent flaws in the material because of the high stress intensity of the pre-crack itself. A blunt notch was therefore thought to better reveal the influence of the additives and process conditions. The impact performance is characterised in terms of force at fracture initiation (maximum force) and the absorbed energy corresponding hereto. This was found to be adequate for internal comparisons, since all data are obtained under the same conditions and the fracture mechanical measures depend linearly on the force and energy, respectively.

The expected influences of the varied process parameters were described in chapter 5.6.2. The influence of the admixture of additives to be expected is less straightforward. Hashemi *et al.* [62] describe the competition between opposing mechanisms that influence the effect on fracture performance. One mechanism is that the reduction in modulus induced by a debonded or soft foreign phase reduces the stress at a given deflection and, hence, point in time during impact. That the effective yield stress of the material also will be lower due to less plastic constraint, further ads to this as a toughening mechanisms. From this mechanism we may expect a reduced maximum force of the blended grades (less load-bearing material/more compliant material) but an increased deflection corresponding thereto. The same would be the result if the additive has a plasticising effect. Another mechanism is that the additive particles may act as stress raisers/flaws initiating the crack. Even soft particles may act as points of stress concentrations irrespective of the bonding to the matrix [75]. This mechanism is of course most likely to dominate for relatively hard particles or additives with a high aspect ratio or sharp edges. Initially round, soft particles may however be deformed under the shear field imposed by melt injection and could thus possibly also cause high stress concentrations. The net effect of the opposing mechanisms is hard to predict qualitatively, not least quantitatively, highlighting the need for experimental evaluation.

To reveal potential differences in the fracture progress among the different grades, it was decided to capture high-speed videos of the impact tests. Any characteristic features in the force-time traces could then be correlated with possible events in the videos of the loading and fracture progress. Microscope investigations of the fracture surfaces ('fractography') are used to reveal information about the conditions prevailing at the site of fracture initiation, possibly linking this event to the presence of the additives.

The abbreviated designations introduced in 2.4.2 are used for the four process conditions: S&C, S&W, F&C and F&W, with e.g. the latter referring to fast melt injection into a warm mould.

5.7.2. Experimental

SENB test specimens with nominal dimensions of 28 x 6 x 1.5 mm^3 were machined from the injection moulded blanks described in chapter 2.4.2 (IPL machine shop, DTU, Denmark). Machining conditions were not specified or recorded, but the specimens were presumably made in accordance with the specification given in appendix 11.2. The specimens were notched to 3 mm depth with a wheel cutter in a milling machine, to the dimensions illustrated in Figure 5.3. The orientation of the test specimen in the blank leads to the crack surface propagating parallel to the melt flow direction and therefore parallel to the expected direction of molecular orientation in the skin cf. the findings in chapter 4.3 for the pure grade. This was expected to be the direction of lowest fracture resistance. Compared to an unnotched specimen of the ligament cross-section, the notch provides a stress concentration factor of approx. 6.4 (determined by finite element analysis[A]) when loaded by forced displacement in three-point bending under the applied conditions.
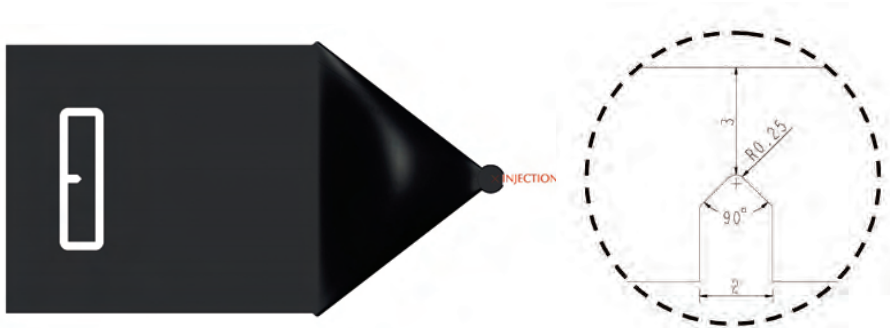

Figure 5.3: Position of SENB specimen in test blank and details of the milled notch.

The impact testing was done with a falling-weight impact tester, instrumented with an AC-coupled piezoelectric force transducer set to a test range of up to 140 N. Fixed Ø6 mm pins were used as support spanning 24 mm, in combination with a custom-made radius 3 mm wedge striker. The setup is illustrated in Figure 5.4. A more detailed description of the impact testing setup can be found in appendix 11.2.
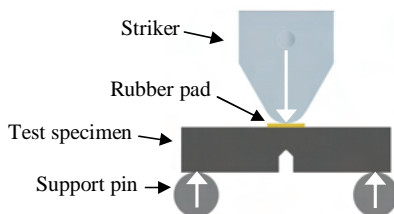

Figure 5.4: Illustration of impact testing setup.

[A] Finite element analyses were made by Laurits Højgaard Olesen, Device Simulation at NNAS.

The drop height for the impact tests was adjusted to 51 mm to provide an impact velocity of 1 ± 0.02 m/s. The mass of the drop weight was 3.7 kg ensuring negligible slowing down during impact. Mechanical damping of the inertial force peak ("mechanical filtering"), as allowed in ISO17281 and quantitatively qualified by e.g. Akay & Barkley [76], was provided by a 0.5 mm thick pad of crosslinked silicone rubber between striker and specimen (Elastosil LR 3003/40, Wacker Chemie GmbH). The loading condition without the damper is characterised by an initial engineering strain rate in the notch root of approx. 165 s^{-1} (based on the linear-elastic assumption). Energy correction tests (chapter 5.5.1) were not made since only relative values were required for the comparisons and only one notch depth was used. Five parallels were impact tested for each combination of additives and process settings.

A MotionPro X4 system with a macro lens (IDT) was used to acquire high-speed video recordings of the fracture progress. The black test specimens were lit by two fibre-optic light sources (Leica Microsystems) to minimize heating. The lights were placed 2 cm from the side surface of the test specimen, above and below the root of the notch. A sampling rate of 73.5 kHz provided 4-5 frames of fracture propagation.

Scanning electron microscopy (SEM) images for fractography were taken on a Quanta 200 system (FEI Europe B.V.). The specimen surfaces were made electrically conductive by sputter coating with a AuPd alloy. The images were acquired in high vacuum mode with 12.5 kV acceleration voltage and a medium spot size.

5.7.3. Impact testing

An example of the force recordings from five impact tests on similar test specimens can be seen in Figure 5.5, alongside the evolution in the derived energy for one of the specimens. Brittle fracture is confirmed by the abrupt drop in force after maximum load. The effect of the damping pads applied between striker and specimen is seen as an increasing stiffness of the first part of the force curves.
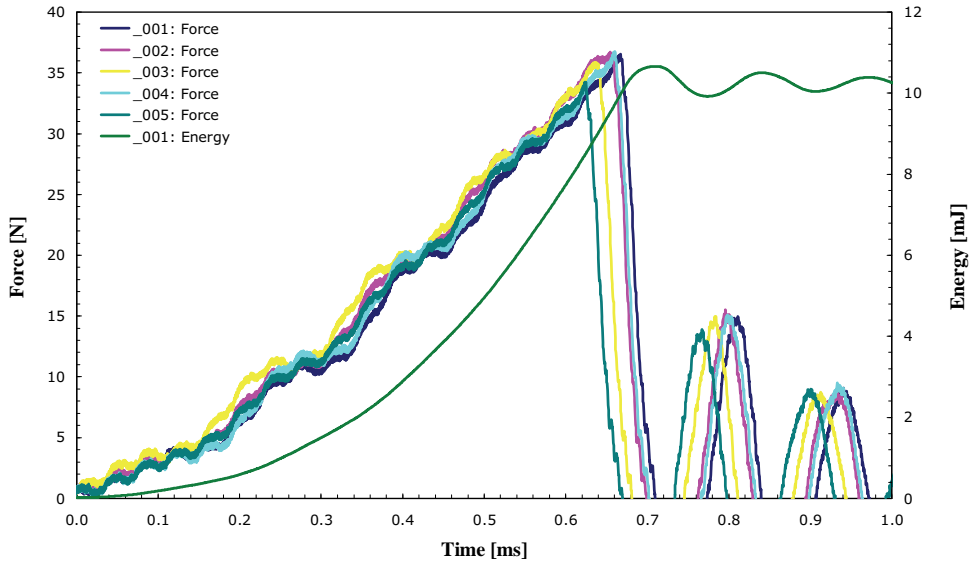
Figure 5.5: Example of impact test data, for neat POM+PTFE moulded under process condition F&W.

Figure 5.6 shows variability charts for the two impact response variables. The data for both measures show remarkably little scatter, bearing the chosen notch approach in mind. The averages of the relative standard deviations for each group is 4% and 7% for the two measures, respectively. No overall correlation is found between the additive or process factors, and the impact response variables. In other words, the impact performance evaluated in this way is neither reduced significantly by the additives themselves nor by the process settings applied to the four grades viewed as a whole. Some data suggest significant effects among the individual groups, but the data basis of only five parallels is deemed insufficient for sound conclusions on this level.
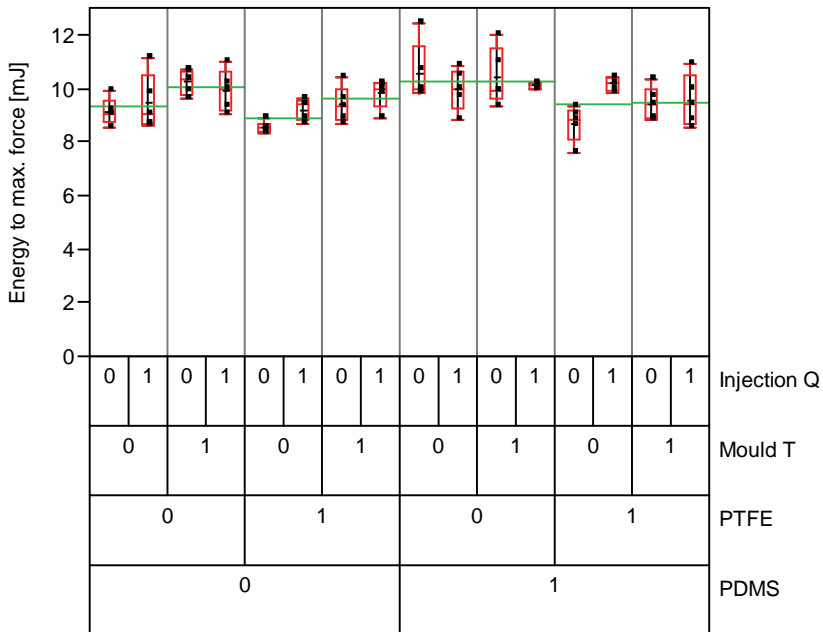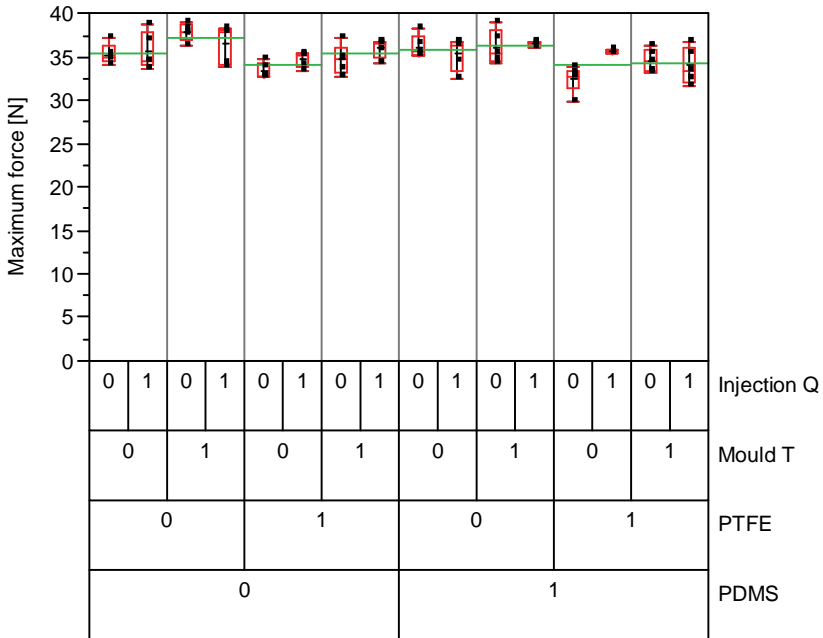
Figure 5.6: Variability charts for maximum force (upper) and energy to maximum force (lower). Mould temperature 0 = Cold, 1 = Warm; injection melt flow 0 = Slow, 1 = Fast.

Chapter 5.6.1 referenced a K_c value of 4.90 MPa√m for the pure POM grade in 4 mm thickness with a 0.25 mm notch radius. The reported value was found in Hashemi *et al.* [62] using the expression:

$$K_c = \frac{3F_{max}L}{2bw^2}Y\sqrt{a}$$

Equation 24

where the geometry function $Y \approx 2.5$ for an $a/w = 0.5$. The same expression yields $K_c = 2.9$-3.5 MPa√m for these data with $F_{max} = 32$-38 N. A higher K_c value from this study could have been expected based on the larger size of the plastic zone when tested in the present 1.5 mm thickness. The lower value may be related to the differences in processing conditions, relative extent of the δ-layer, direction of loading or the laser additive in present neat POM grade.

5.7.4. High-speed video

The high-speed video recordings were acquired at 73.5 kHz. This high sampling rate requires a low resolution and the CCD of the camera thus had to be masked off to only capture the most important area of the specimen, i.e. the area around the notch root (see Figure 5.7). The frames in Figure 5.8 and Figure 5.9 shows the crack initiation and growth in the neat POM and the PDMS blended grades, respectively. The neat POM shows a simple brittle fracture without any immediate signs of plastic flow. The same overall impression was found for the grade with the PTFE additive alone (not shown). The PDMS modified grades reveal very different viscoelastic fracture behaviour. Fibrils of material are seen to form a craze-like zone across the crack opening. The two grades shown have similar evolution in the force data under crack growth, i.e. with the force drop indicating brittle fracture. This means that the fibrils forming carry only negligible load and indicates that they consist of PDMS rather than e.g. plasticised POM. This conclusion underpins the assumption that the PDMS additive, because of its immiscibility with the POM matrix and its high molecular weight, remains in small domains rather than dispersing homogenously throughout the material. Had the latter been the case, then a dramatic change in fibril formation with an approximate PDMS concentration of only 1 wt% would not be expected. Moreover, a less degree of viscoelastic contraction of the fibrils would be expected had they consisted of yielded POM; the fibrils seen here contract completely upon rupture when the crack opens further (confirmed by the SEM fractography).

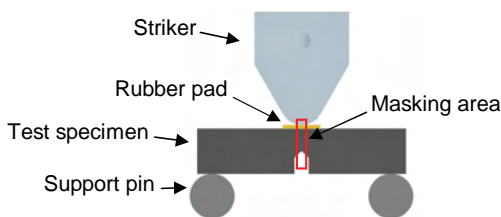Figure 5.7: Illustration of impact test showing the masking area used for high-speed video recordings.
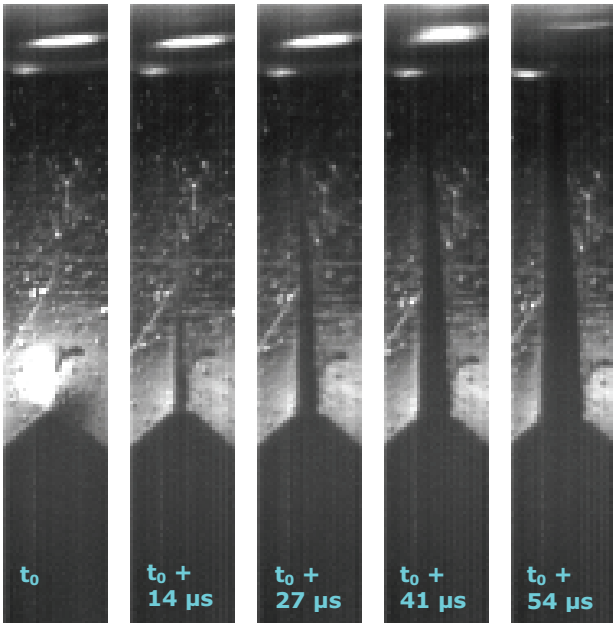
Figure 5.8: Crack growth in neat POM S&W. The crack is growing from the notch in the lower part of the pictures and upwards. The white spot on the first frame is caused by reflection of light into the camera, due to Poisson contraction of the material around the notch root.
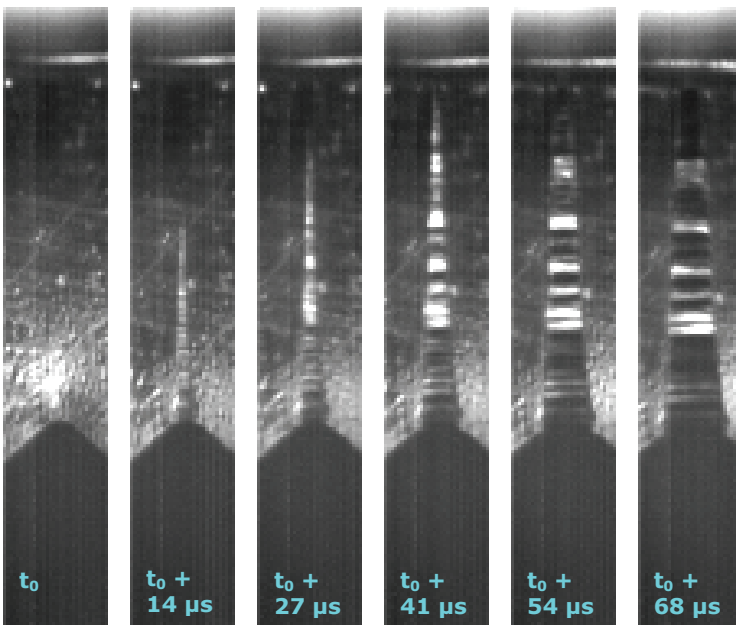

Figure 5.9: Crack growth in neat POM+PDMS S&W.

The specimens were markedly heated during video recording, even with the use of fibre-optic lights. The maximum force measured under the video recorded impact tests were all on the order of 30-35% lower than the test results reported in chapter 5.7.3. This obviously adds to the uncertainty regarding the extent to which the observed phenomena are relevant at ambient temperatures also. At any case, the fibril formation found for the PDMS containing grades do not seem to relate to the crack initiation and hence to the reported impact performance measures.

5.7.5. Fractography – part 1

Fracture surfaces from the four grades were examined by SEM to reveal differences in their characteristics. No fundamental differences were found between fracture surfaces of specimens of the same grade but with different process history. A fracture surface from the grade with only the PTFE additive is shown in Figure 5.10. The initial assumption of negligible adhesion between the PTFE and POM is confirmed by the smoothness of the particles and holes left behind. All grades showed reduced roughness of the fracture surface near the skin layer, as well as evidence of a small plastic zone at either or both of the corners. Consistent overall impressions were found for the two grades without PTFE additive. Figure 5.10 illustrates the overall impression of the two PTFE grades; namely that the PTFE particles have been deformed into flat ellipsoidal geometries, presumably by the shear stress generated under injection. The smaller axis of the ellipsoids is predominantly oriented normal to the plane of the blank, consistent with shear alignment. The situation is illustrated in Figure 5.11 case A. The direction of loading chosen in this study is seen to be the least severe with respect to crack initiation originating from the additive-matrix interface. In Figure 5.11 case B, corresponding to out-of-plane bending of the plate, the added shear stress in the plane of primary disc orientation would cause a combination of in-plane crack opening and shearing of the fracture surface. The result is believed to be a reduction in the measured impact strength at loss of mechanical integrity. The most severe additive orientation, case C in Figure 5.11, would for the present geometry correspond to e.g. out-of-plane tensile impact testing. This testing scenario is hardly possible with the chosen geometry, but would be relevant for e.g. characterisation of fracture resistance in weld line interfaces. The highly deformed particles suggest that the weld line strength of these grades may be severely impaired. Studies of this are supported by the procured testing setup but has not been conducted as part of this project.
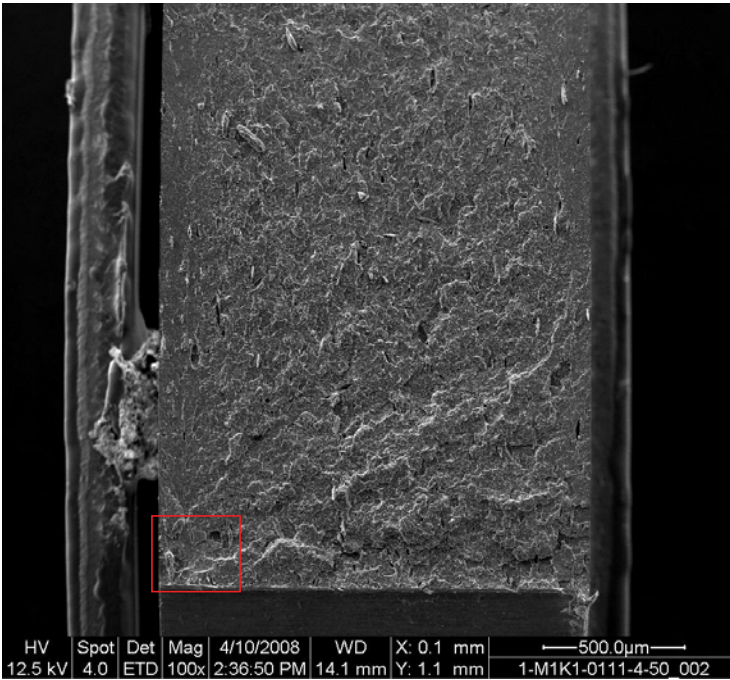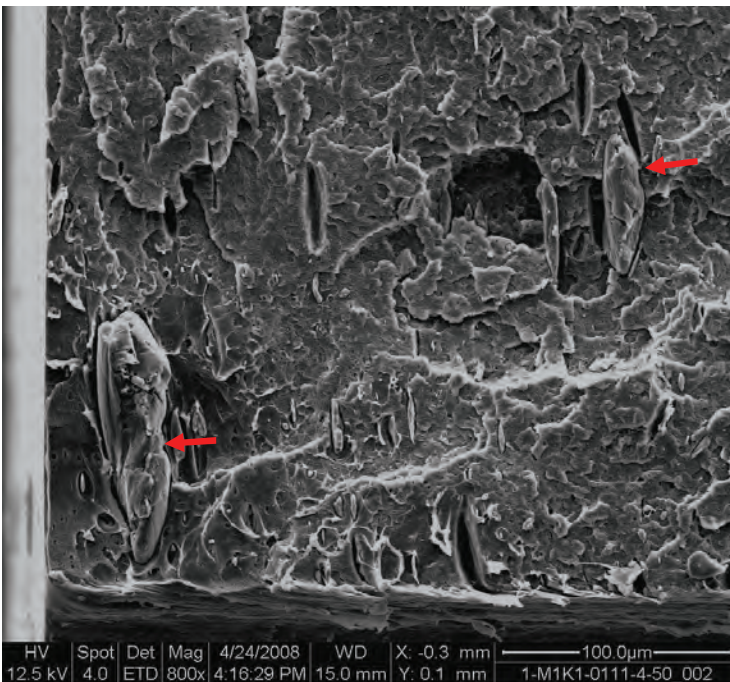
Figure 5.10:
SEM fractography of neat POM+PTFE F&W. The notch is in the bottom of the picture and the crack propagated upwards. The red square (upper) indicates the position of the close-up (lower), showing the deformed and flow oriented PTFE particles and holes left behind (arrows), and the plastic zone (lower left corner) containing a large PFTE particle.
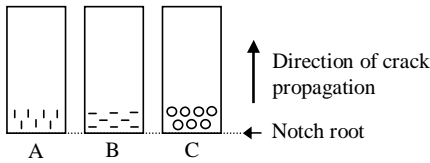
Figure 5.11: Sketch of fracture surfaces with the three principle orientations for additives of ellipsoidal shape. The loading direction is normal to the plane of the paper.

5.7.6. Extra impact tests: Out-of-plane impact flexure

It was decided to carry out some further experiments with the four grades, based on the findings described above. Out-of-plane impact flexure was made in an attempt to generate a high shear flow in the in-plane direction to load the material cf. scenario B in Figure 5.11. It was thought that this loading might better reveal a potential difference in impact performance caused by the PTFE additive than the traditional SENB loading used above. Specimens were this time machined from plates in both directions parallel and transverse to the flow direction, referred to as FD (flow direction) and TD (transverse direction)[A]. Only plates from the S&C and F&W process conditions were used, expecting that these represent the conditions of most pronounced difference in performance. A notch was made as described in chapter 5.7.2, yet now only 2.1 mm in depth (a/w = 0.35). The support span was adjusted to 22 mm width (minimum possible with the procured fixture) and the specimens were impacted without mechanical damping, which was found unnecessary when loading in the out-of-plane direction. Five parallels were tested per group. The resulting initial strain rate in the notch root was determined by FEA to be ~50 s^{-1} and resulted in brittle fracture for all specimens.

Figure 5.12 and Figure 5.13 show variability charts for force and energy, respectively. A clear effect of the loading direction is seen, with the TD specimens giving both lower maximum force and energy compared to the FD specimens. For the FD specimens of the PDMS grade a significantly higher force and energy is seen for the F&W process condition. Such effect, which is not seen when comparing the other groups, was found most likely to be attributable to an error in handling of the specimens in the process of machining them from the test blanks (e.g. taking specimens from the wrong plastic bag when machining-in the notches). This assumption was strengthened by a comparison of fracture surfaces, in which a specimen from the S&C-FD group showed the typical characteristics of a TD specimen (described in chapter 5.7.7). The observed effect is therefore thought not to be genuine. All in all, it may be concluded that the PTFE additive (and PDMS additive) did not show a significant influence on the impact behaviour under this loading scenario either.

[A] The nomenclature regarding orientation used in this thesis refers to the direction of the normal stresses causing opening of the crack in mode I loading, relative to the melt flow direction. The direction given will therefore be perpendicular to the general direction of crack propagation in the specimen.

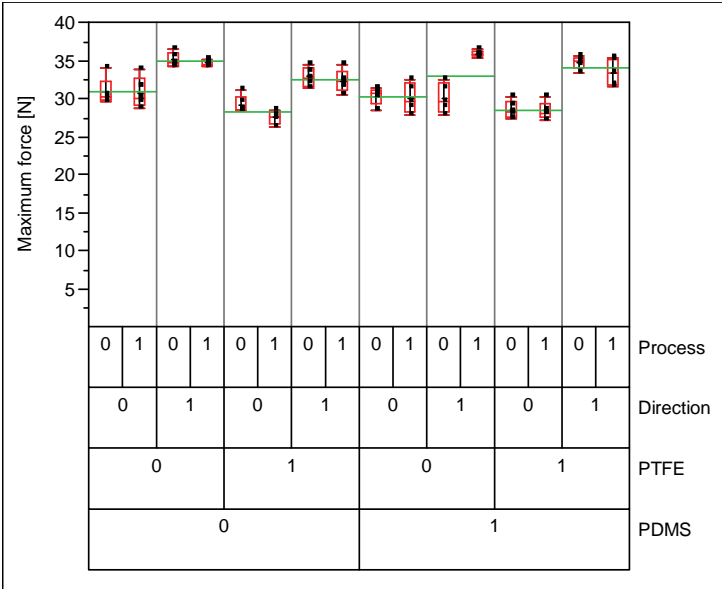Figure 5.12: Variability chart for maximum force for sideways impact of notched specimens. Direction 0 = transverse direction (TD), direction 1 = flow direction (FD). Process 0 = S&C, process 1 = F&W.
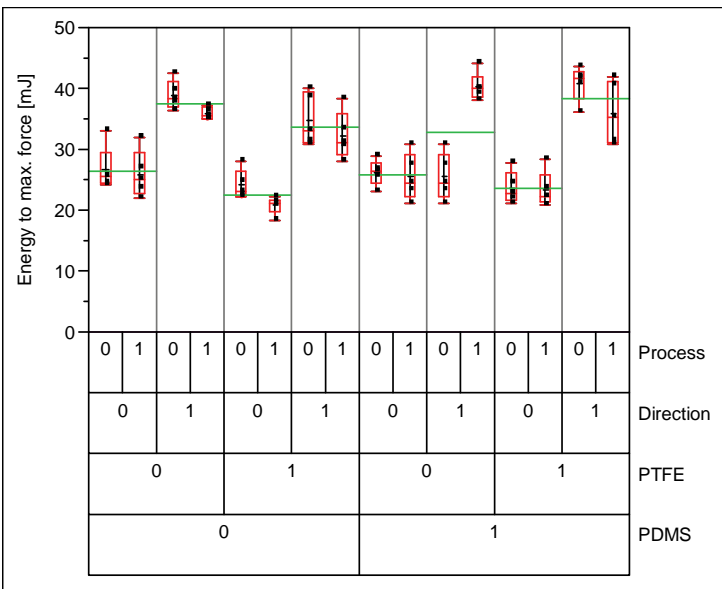

Figure 5.13: Variability chart for energy to maximum force for sideways impact of notched specimens. Direction 0 = transverse direction (TD), direction 1 = flow direction (FD). Process 0 = S&C, process 1 = F&W.

5.7.7. Fractography – part 2

Fracture surfaces from the out-of-plane impact tests were also investigated by SEM fractography. Examples are shown in Figure 5.14-Figure 5.16. The plastic zone could be identified on all examined specimens. This zone is known to be the site of fracture initiation [49;53;77;78], which was confirmed to be in the notch root in all cases. The position of the plastic zone was found to depend on the loading direction. In the FD-specimens the centre of the plastic zone was found at a depth of approx. 200-300 µm below the moulded surface of the specimen. In the TD-specimens the fracture was found to initiate in the corner of the notch at the moulded surface. This consistent difference implies that the material in the δ-layer has a higher yield stress than the underlying layers when loaded in the melt flow direction. The TD-pictures suggest that this is not the case when loading in this direction. It may therefore from this observation be concluded that the δ-layer is stronger in the direction of orientation as indicated in chapter 4 for the pure POM plates (the Impact & Indentation Study). This is in agreement with e.g. the reference of Schrauwen [73].

Figure 5.14:
Neat POM S&C-FD
specimen. The notch is in
the bottom of the pictures
and the striker hit the
specimen from the left-
hand side. The red square
(upper) indicates the
position of the close-up
(lower). The arrow in the
close-up indicates the
centre of the plastic zone.
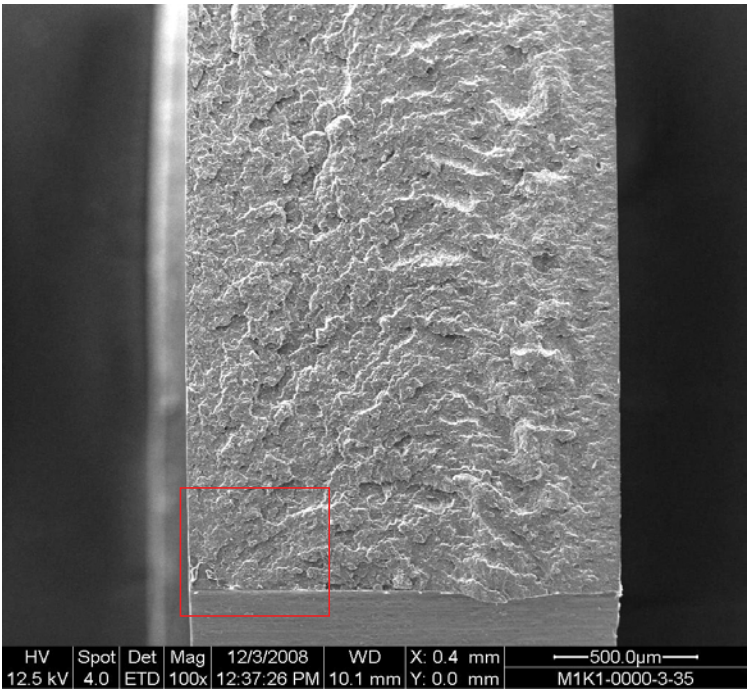
Figure 5.15:
Neat POM S&C-TD specimen. The notch is in the bottom of the pictures and the striker hit the specimen from the right-hand side. The red square (upper) indicates the position of the close-up (lower). The arrow in the close-up indicates the centre of the plastic zone.

Figure 5.16:
Neat POM+PDMS+PTFE
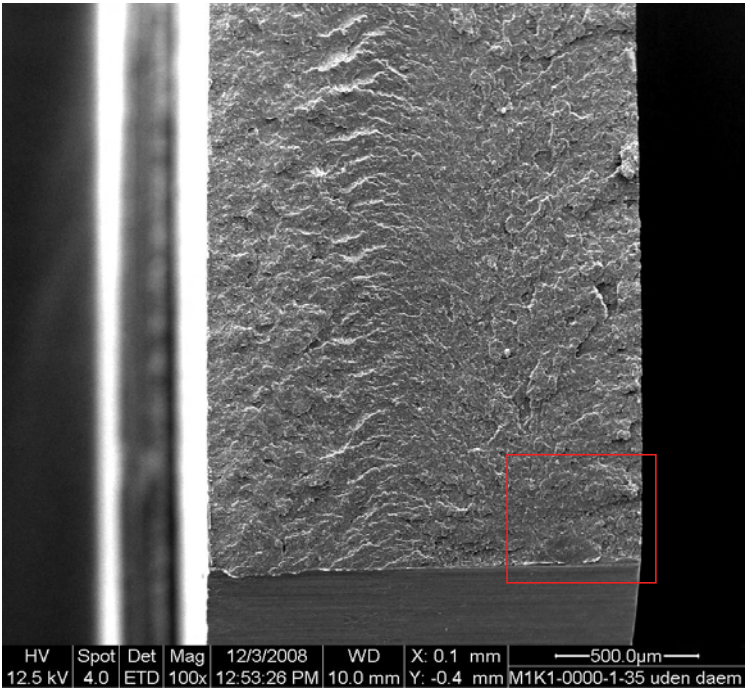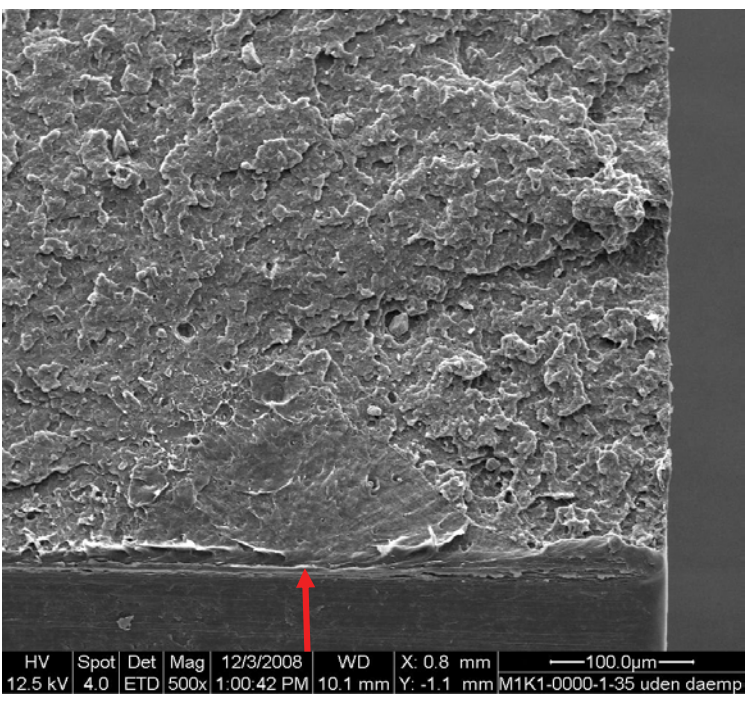F&W-TD specimen. The
notch is in the bottom of
the pictures and the striker
hit the specimen from the
left-hand side. The red
square (upper) indicates
the position of the close-
up (lower). The arrow in
the close-up indicates the
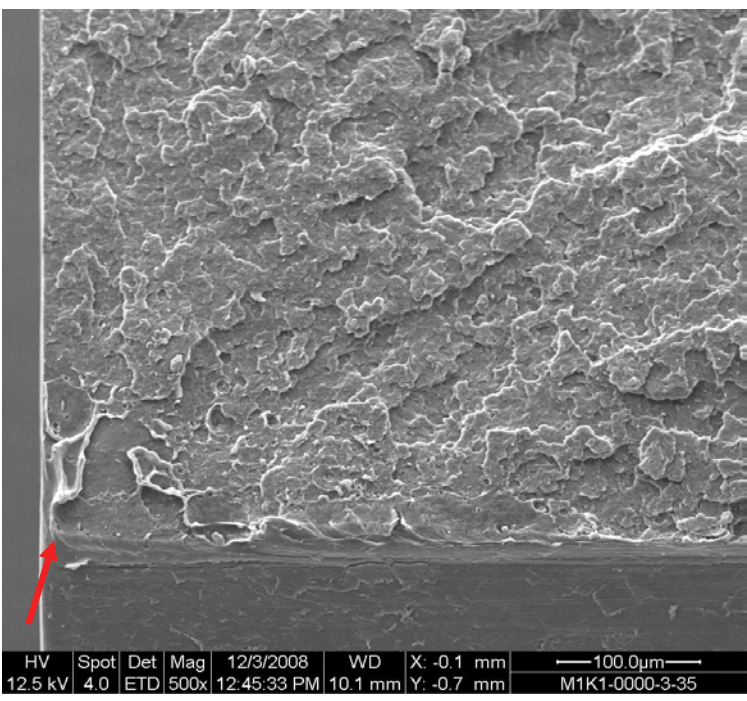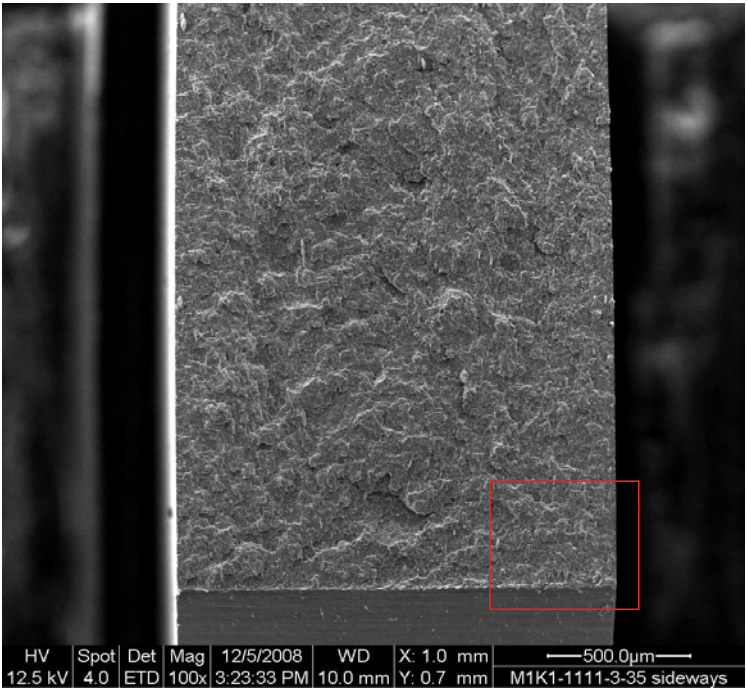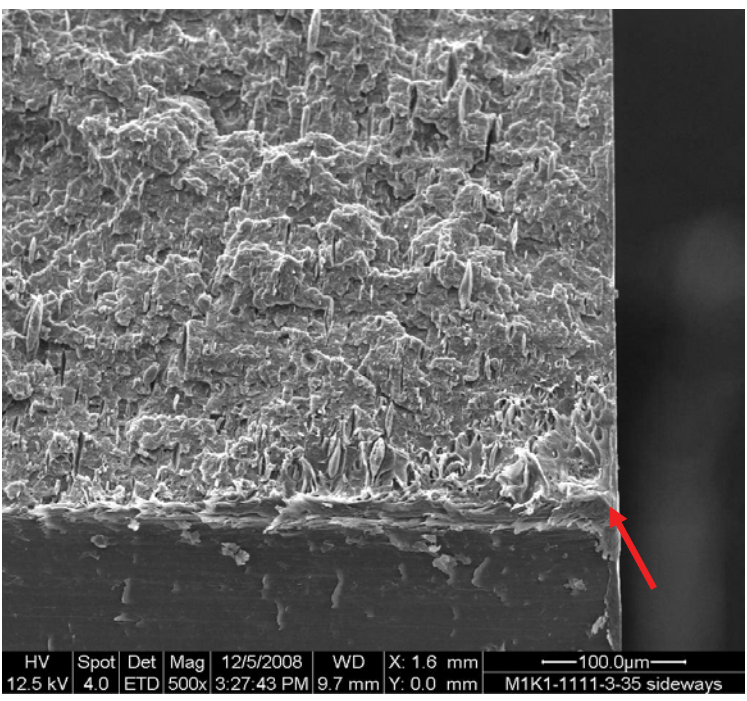centre of the plastic zone.

5.7.8. Determination of critical stress intensity factor and strain energy release rate

Based on the discussion in chapter 5.7.3 it was decided to determine the K_c and G_c values of the neat grade, i.e. the grade containing only the laser additive. Specimens from process condition S&W was used, since it is closest to that used by Hashemi *et al.* [62] and to the recommendations from the material manufacturer.

Eighteen specimens were prepared with pre-cracks of varying depths cf. the ISO 17281 procedure described in chapter 5.5.1. A sharp notch was made by milling with a nominally sharp engraving tool with an apex half-angle of 20° (4000 RPM, 1 mm/s feed). The notch was further sharpened into a pre-crack using a fresh razor blade in a special holder in a milling machine (without rotation), pressed swiftly into the notch to a controlled depth of 0.2 mm below the notch depth[A]. The resulting crack-depth ratios were $a/w = 0.38$, 0.53 and 0.68, respectively. An example of the force-time curves from the impact tests are shown in Figure 5.17. The lacking or very subtle inertial force peak (would be between 0 and 0.1 ms) suggests that the system is over-dampened with the chosen 0.5 mm rubber pad. Damping pads consisting of Parafilm (0.15 mm), as suggested by e.g. Pavan [79], was also tested but was found to provide too little damping for pre-cracked specimens of this size, where the short time-to-fracture yields little time for the oscillations to die out. In fact, with the chosen solution one group exhibited oscillations that were just out of the ±10% limits of fluctuation allowed by ISO 17281 ($a/w = 0.68$). The chosen solution may in this light be considered barely enough. The differences in unloading slopes seen in Figure 5.17 are a consequence of the different rates by which the broken sample is pushed away from the striker during crack growth. The differences thus arise from the different amounts of absorbed energy at fracture, rather than from different degrees of brittle-ductile behaviour.

[A] The standard requires a pre-crack length of minimum four times the radius of the preceding notch. In this case, the requirement compares to a notch tip radius from the engraving tool of <50 μm, which was found to be a reasonable assumption. The risk from making very long pre-cracks by pressing a razor blade into the notch is the introduction of crazing at the crack tip, which will effectively blunten the crack. The chosen method of pre-cracking is widely used [61].
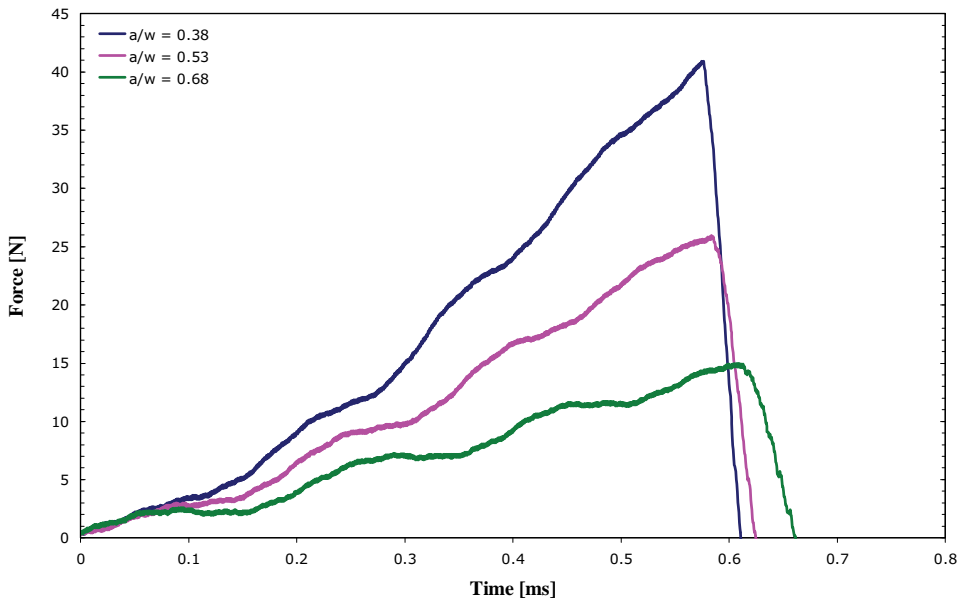
Figure 5.17: Force-time curves for pre-cracked specimens with varying crack lengths.

The critical stress intensity factor was determined cf. ISO 17281, i.e. from the specimens of relative crack length $a/w = 0.53$ (seven parallels), resulting in $K_c = 2.70$ MPa√m. A check of the applicability of the LEFM procedure for all the specimens and chosen crack lengths at hand was made by plotting $F_Q/(b{\times}w^{0.5})$ against the geometry calibration factor $f(a/w)$, as seen in Figure 5.18[A]. A linear regression through origo is seen to represent the data well, the slope yielding $K_c = 2.67$ MPa√m.

[A] This approach corresponds to the plot of $\sigma^2 Y^2$ against a^{-1} used in Hashemi *et al.* [62].
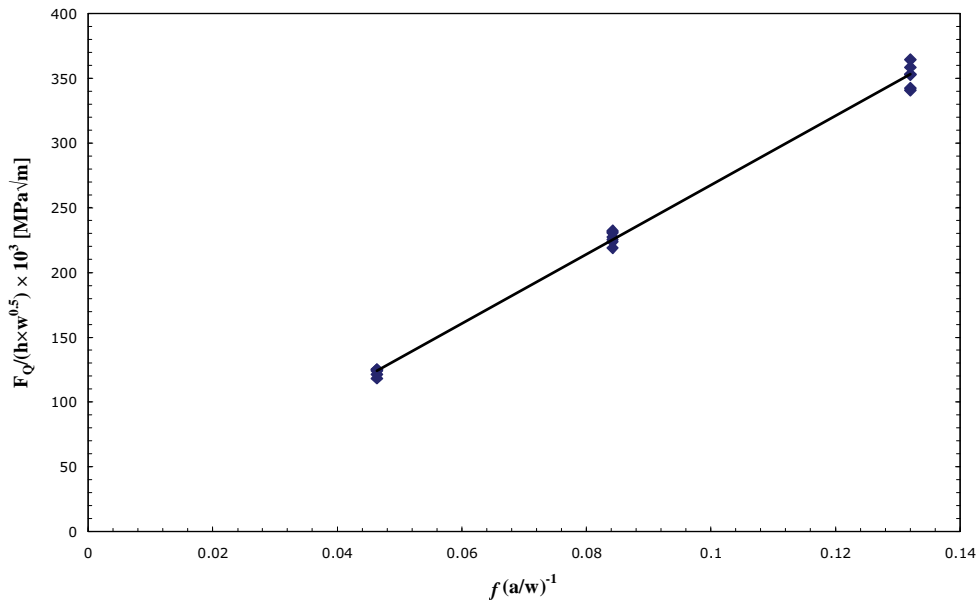
Figure 5.18: K_c determination for neat POM S&W based on all 18 data points.

The K_c value found here for the neat grade is somewhat below the expected value for the pure grade under similar conditions ($K_c \approx 3.3$ MPa√m as found in 5.6.1). This may be taken as an indication of slight embrittlement caused by the laser additive, presumably through a yield stress increasing effect on the micro-scale. A direct comparison of material moulded under the same conditions would have to be made for a certain conclusion in this regard.

The critical strain energy release rate was found cf. the ISO 17281 approach using all eighteen measurements[A]. The plot of the total absorbed energy at F_Q is shown in Figure 5.19, alongside the energies after ECT correction. The energy correction test was made with an impact velocity of ~0.52 m/s to provide a time to F_Q within ±50% of the time to fracture in the SENB tests for all three crack lengths (requirement of the standard). A value of $G_c = 1.40$ kJ/m² is found, but it should be noted that the fluctuations of neither of the specimens with $a/w = 0.68$ were within the required ±10% limits of the standard (all were for $a/w = 0.53$ and 0.38). The linear regression is however seen to represent all three groups well. The positive offset of 1.12 mJ corresponds presumably to the kinetic and inertial energies of the test.

[A] One data set had to be manually calculated through Newton's second law and the equations of motion due to premature triggering of the optoswitch on the impact tester. The validity of the method of manual calculation was confirmed by a cross-check on another data set.
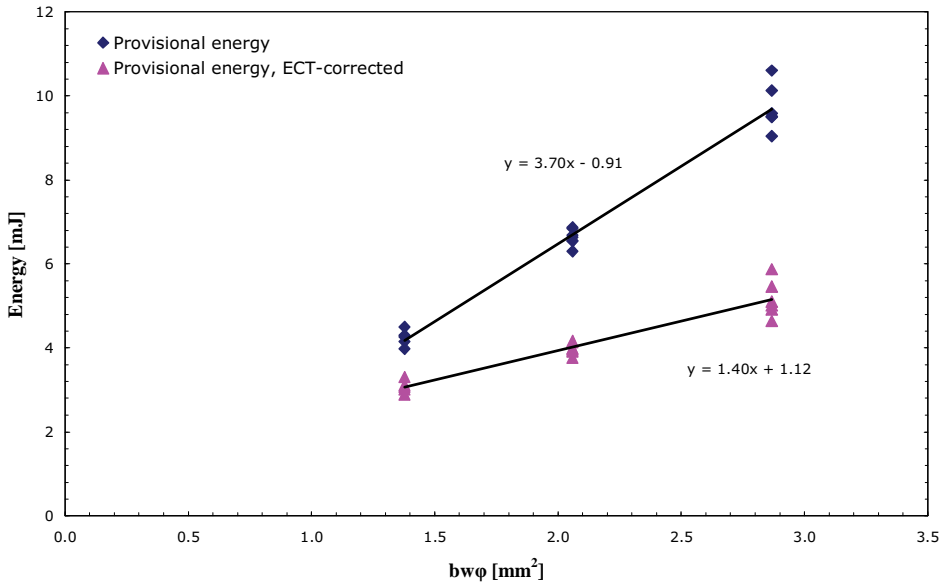
Figure 5.19: G_c determination for neat POM S&W cf. the ISO 17281 procedure.

The G_c value found here may be compared to the G_c estimate of 4.8 kJ/m^2 derived in chapter 5.6.1, suggesting a highly reduced toughness of the present grade. The comparison with the K_c value suggests that the toughness reduction stems from a reduced strain-to-break. The dynamic modulus of elasticity may be estimated through equation 14 yielding ~5.1 GPa, which is very high compared to the expected value of around 3 GPa. A cross-check as proposed in ISO 13586 against the modulus determined from the stiffness – equation 16 – may be made, if the ECT data are used to derive the true curve for force vs. specimen load-point displacement. A curve fit of the corrected displacement has to be made to cope with the phase-lag between force and displacement caused by the simple mass-spring model from which the data are calculated – Figure 5.20 left. The curve compares well with the principle evolution of the specimen load point displacement for a rubber dampened impact as reported by Bezeredi *et al.* [80] – Figure 5.21. A surprisingly high modulus of elasticity is found from this stiffness also, ~4.6 GPa. With the little strain-rate dependence of the modulus of POM reported by Plummer [49] in mind, this might suggest a shortcoming in this rather simple approach. This may be why this kind of comparison is not encouraged in ISO 17281, although the K_c^2/G_c-ratio still is to be reported for the sake of information. Determination of the dynamic modulus of elasticity through undampened impact of unnotched specimens were also tested, but excessive crushing and buckling of the specimens was found for this combination of low thickness and high moment of inertia of these specimens. The approach was therefore abandoned.
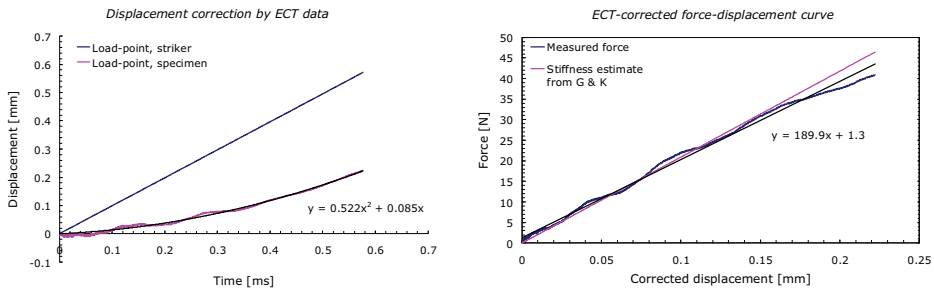
Figure 5.20: Estimation of true curve for force vs. specimen load-point displacement (for specimen with $a/w = 0.38$).
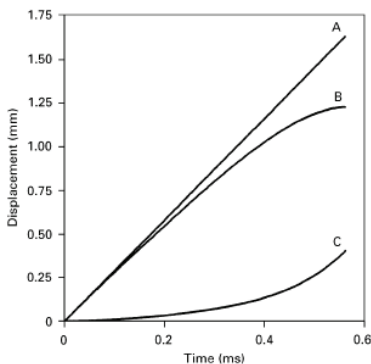
Figure 5.21: Principle evolution of load-point displacement vs. time for striker (A), damper (B) and specimen (C). From Bezeredi *et al.* [80].

5.7.9. Main conclusions

The following main conclusions may be drawn from the impact testing part of the Additives & Impact Study:

- All the grades fail by brittle fracture when tested in the SENB geometry under the chosen loading conditions.
- No technically significant change in impact performance was found from the admixture of PDMS and/or PTFE additives, or from the changes in process conditions.
- Fractography by SEM showed that the PTFE particles had been smeared out into flat ellipsoidal geometries, presumably as a consequence of high shear in the melt. The particles were highly aligned in the flow direction, and it was seen that the chosen impact testing scenario is far from worst case with respect to the particle orientation. This might explain the lack of influence on the impact measures from the admixture of the PTFE additive.
- Specimens impacted in out-of-plane bending showed a significant increase in force and energy at fracture initiation from loading of the material in the flow direction, compared to loading transverse to flow. The same effect is expected for standard SENB loading in the two directions. The out-of-plane bending loading is also found to be insensitive to the additives and the varied process conditions.

- Values of K_c and G_c were determined for the neat grade of the S&W process condition. A comparison with reference data suggests a possible embrittlement from the laser additive in the neat grade.
- The performed impact tests imply that the tribologically modified grades can be processed under the same conditions as the neat POM without noteworthy decrease in impact performance.
- Fractography of the PTFE containing specimens suggests that this additive may cause a significant reduction in the weld line strength retention.

5.8. The Impact & Indentation Study – impact testing
5.8.1. Introduction

Based on the conclusions from the Additives & Impact Study it was decided to undertake a more fundamental investigation of the impact properties of the pure POM grade itself, i.e. not containing the laser additive. The moulding of the test blanks for this study was described in chapter 2.4.3 and is referred to using the abbreviated designations VS&VC, VS&W, VF&VC and VF&W, with e.g. the latter meaning very fast melt injection into a warm mould. Moulding conditions in a production setup are expected to fall within these extreme conditions. The plate blanks contain moulded-in notches to provide for impact tests of notched SENB specimens with the δ-layer of the moulding present in the notch root.

The out-of-plane impact bending in the Additives & Impact Study suggested a strong dependence of the crack initiation site on the loading direction of the δ-layer. This raises the question as to whether a milled-in notch or pre-crack can be expected to reveal process dependence in impact properties, as it would come to expression in a real moulded component. The PLM investigation in chapter 4.1 revealed pronounced differences in the δ-layer thickness of the specimens from the present study. The WAXS and SAXS investigations in chapter 4.3 furthermore showed process dependent differences in the lamellar thickness and extent of molecular orientation in the δ-layers. With this in mind, it seems likely that different conclusions regarding process dependence and anisotropy might be found from impact studies based on the standard pre-crack approach versus testing on specimens with a moulded-in notch. This latter approach is expected to better simulate the conditions leading to brittle fracture in real components, though it may yield non-conservative values compared to the standard approach. The impact part of this study compares these two approaches to impact fracture testing.

5.8.2. Experimental

The test specimens were machined from the injection moulded blanks described in chapter 2.4.3 using a fine-toothed band saw (24 TPI blade, 15 m/s cutting speed, 3 mm/s feed). The specimens for the impact tests with moulded-in notch were cut directly to the SENB geometry with nominal dimensions of 28 x 6 x 1.5 mm^3 from the positions shown in Figure 5.22. The size and notch dimensions in these specimens are nominally the same as used in the Additives & Impact Study – see Figure 5.3. The same nomenclature as introduced in chapter 5.7.6 is used to designate the two specimen directions: FD for specimens cut out in the melt flow direction, TD for specimens cut out from the direction transverse to the melt flow, as shown in Figure 5.22.
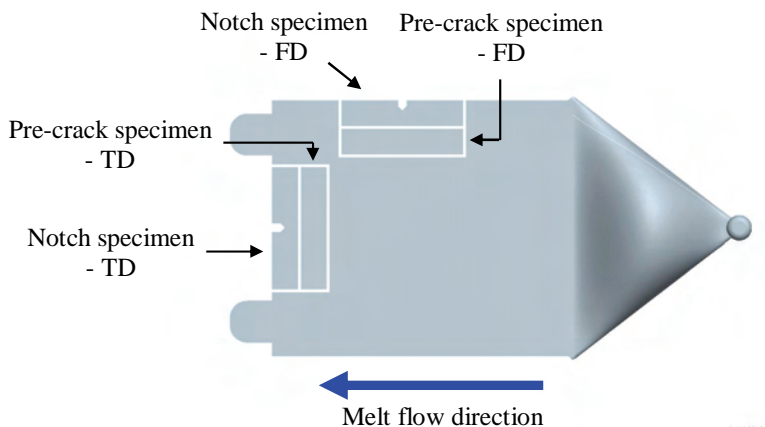
Figure 5.22: Specimens for the Impact & Indentation Study as sawn from injection moulded test blanks. Note that the pre-crack specimens are shown without the pre-crack.

The specimens for the pre-crack tests were sawn to slight excess width and milled down to 6 mm from one side to provide an even surface of contact with the support of the impact testing rig (described in chapter 5.7.2 and appendix 11.2). A sharp notch was milled to 2.8 mm depth from the same side using the procedure described in 5.7.8, including sharpening into a pre-crack with a razor blade to a total crack length of 3.2 mm ($a/w = 0.53$). The surface opposite the notch (the compression side during the impact tests) was left as sawn, yet freed from burr, if any. The specimens were impact tested under the same conditions as in the Additives & Impact Study, described in chapter 5.7.2. A close-up picture of the actual impact testing setup is shown in Figure 5.23.
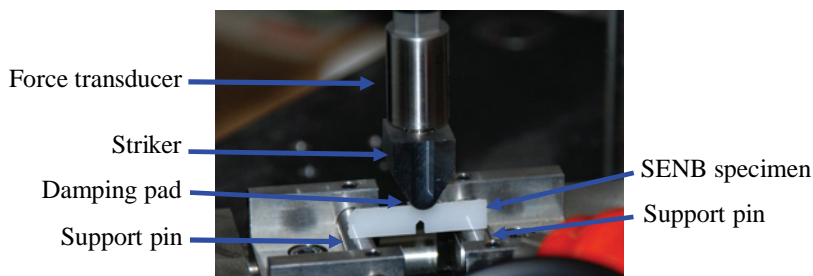
Figure 5.23: Close-up of impact testing setup. A guide fixture used to accurately position the specimens has been removed for clarity (can be seen in appendix 11.2).

5.8.3. Impact testing - comparison of moulded-in notch and pre-crack methods

An example of force recordings from the two approaches, pre-crack and moulded-in notch, and the two loading directions, TD and FD, can be seen in Figure 5.24. Brittle and ductile-brittle fracture is confirmed by the abrupt drop in force after maximum load.
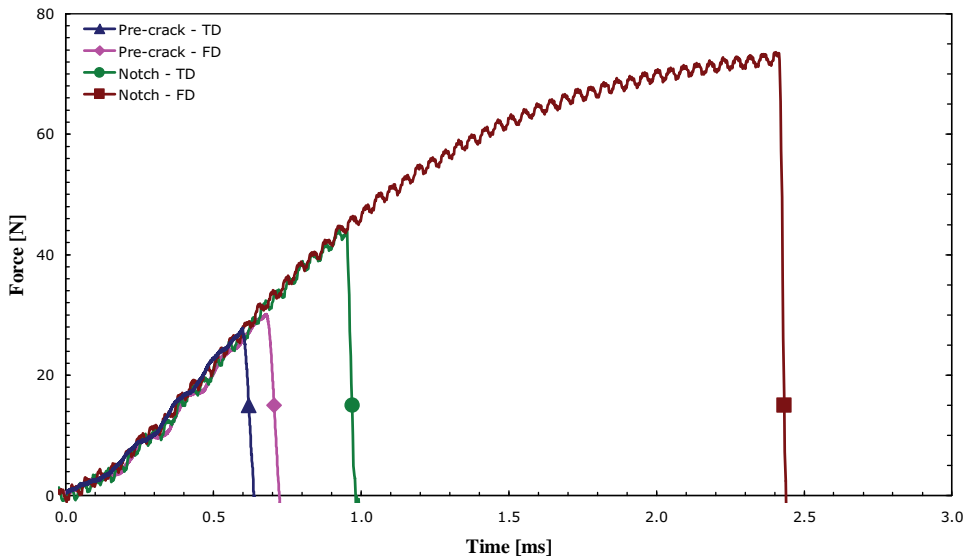
Figure 5.24: Example of force curves for process condition VS&VC. Notice the self-similarity of the curves for both loading directions and testing approaches.

The maximum force, corresponding to the force at fracture initiation, is compared for the two approaches in Figure 5.25. The data from the notch approach reveals a pronounced anisotropy of the impact behaviour. A dependency on the process condition is also seen. The pre-crack method reveals no difference from process conditions and only very slight influence on the loading direction. The force levels are of course much lower in the pre-crack tests than in the notch tests.
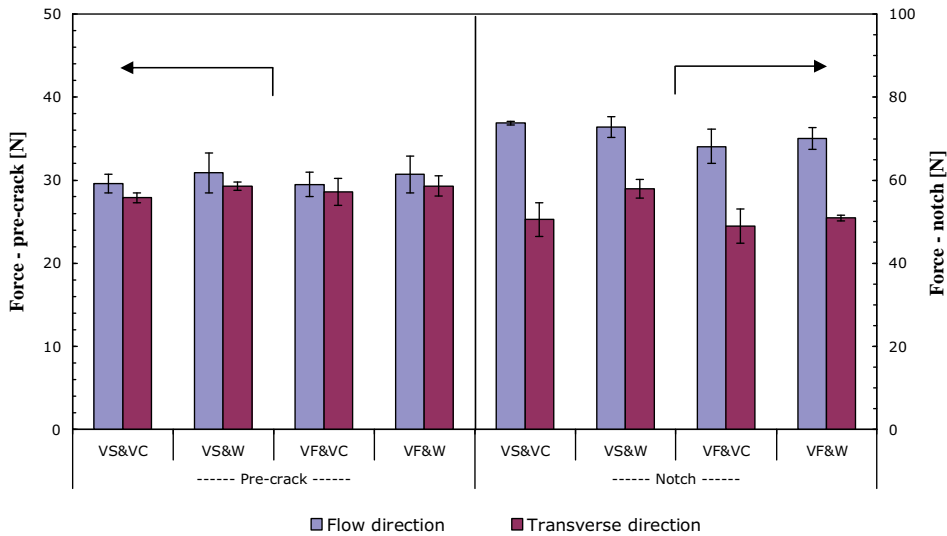
Figure 5.25: Comparison of maximum force for specimens with pre-crack and moulded-in notch, respectively.

As seen from Figure 5.24, the difference in impact behaviour between the two loading directions lie primarily in the time-to-fracture and hence the deflection and energy corresponding hereto. The comparison of energy-to-fracture is made in the terms of J_c as per equation 19. For the pre-cracked specimens this is confer the approach of e.g. Fasce *et al.* [59]. For the pre-crack specimens and the TD-specimens with moulded-in notch the standard ECT procedure of ISO 17281 can be used, since the force traces are essentially linear up to fracture (brittle cf. the definition in chapter 5.1). This approach was not found feasible, however, for the FD-specimens with moulded-in notch, where the relatively long time-to-fracture would prescribe a fall height in the ECT of only a few millimetres. A measurement under such conditions is not readily possible with the impact tester used, and would furthermore not simulate the decreasing evolution of force encountered in the fracture tests. The correct energy has therefore instead been calculated for these specimens from a determination of the actual load-point deflection of the specimen, not by ECT, but through the use of high-speed video recording and digital image correlation (DIC). A speckle pattern was applied to the side of a specimen by spray paint and the impact was recorded with a digital high-speed video camera at 100 kHz (Fastcam Ultima APX RS, Photron). DIC software (VIC-2D, Limess, Germany) was used to determine the actual load-point displacement based on the relative movement of the speckles, from which the corrected energy was calculated through the work of external forces. The approach was qualified by comparison with ECT-corrected data for the TD-specimen from the same blank (self-similar force traces) – Figure 5.26. The difference between the uncorrected energy and the energy based on the DIC-corrected displacement is seen to be similar to the energy correction from the standard ECT approach. This procedure was used for all the FD-specimens with moulded-in notch, based on separate DIC displacement-corrections for each process condition.
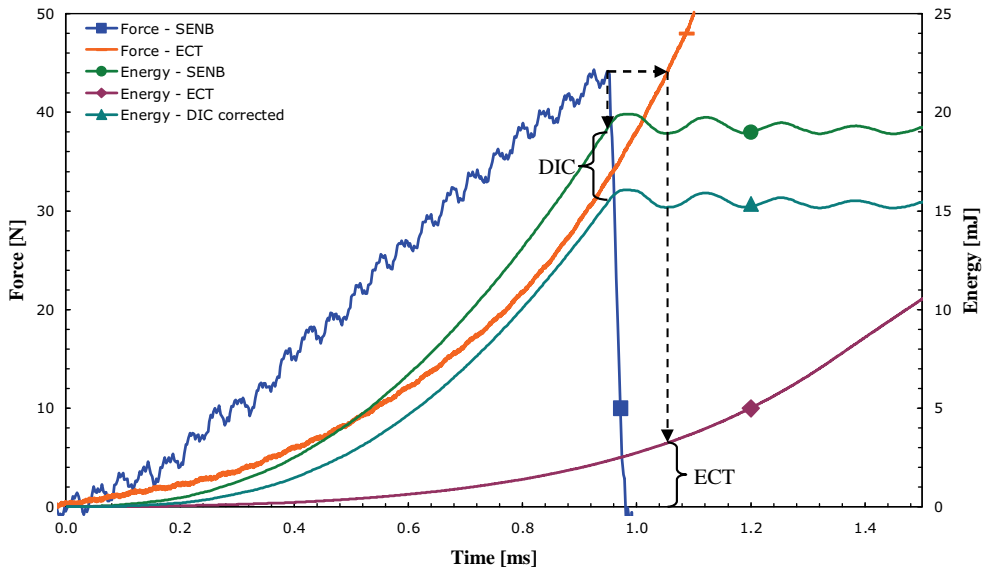
Figure 5.26: Energy correction by ECT and DIC (corrected energy curve) of notch data from transverse direction (VS&VC process condition).

The J_c values calculated from the corrected energies at crack growth initiation are compared in Figure 5.27 across process, loading direction and evaluation method. The data clearly illustrate the difference between the two approaches for evaluating anisotropy and process-dependence of impact behaviour. The ratio of anisotropy for the four process settings range from 2.5 to 4.4 for the moulded-in notch data, and from 1.1 to 1.3 for the pre-crack method. The relative effect of the process conditions are up to 70% for the notch data (thickest/thinnest δ-layer), but less than 18% for the pre-cracked specimens. The latter of course yields a much lower toughness values, however. Since only five specimens (with constant relative crack-length) were tested per configuration G_c-values cannot be determined according to the standard procedure. Taking the inertial and kinetic energy contributions as found in the Additives & Impact Study, we may compare the G_c value from that study with the J_c value for the VS&W-TD specimens of the pre-crack tests in this study. The former was $G_c = 1.4$ kJ/m^2, the latter yields $J_c = 1.7$ kJ/m^2 (the uncorrected value is 2.1 kJ/m^2). Comparing the highest uncorrected J_c-value with the size requirement (equation 20) results in a minimum yield stress requirement of less than 50 MPa, which is clearly below even the quasi-static value. The J_c-values found should therefore represent the plane strain value. It may be noted from the presented data from specimens with moulded-in notch, that in the weakest direction, TD, the highest impact fracture toughness is found for the VS&W process condition, both in terms of force and energy at fracture initiation.
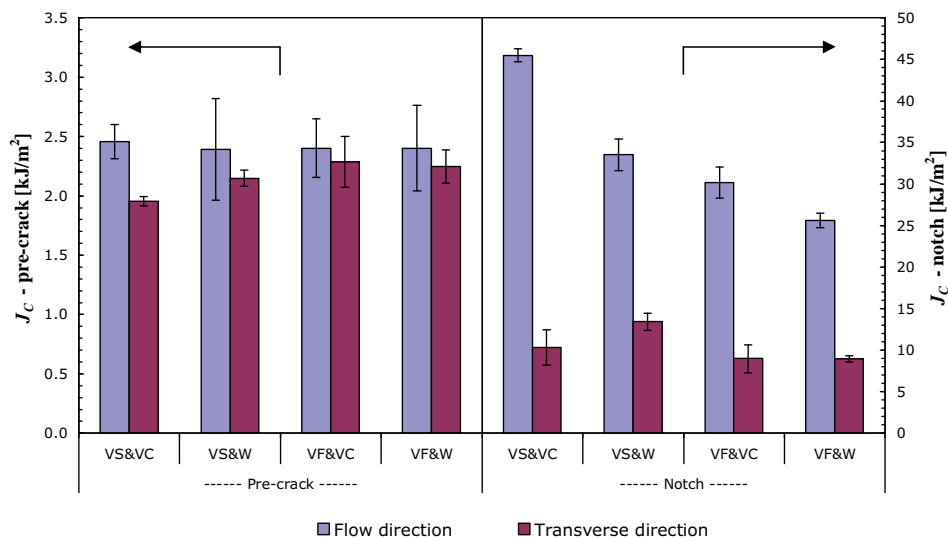
Figure 5.27: J_c for specimens with pre-crack and moulded-in notch, respectively.

5.8.4. Determination of critical stress intensity factor for pre-cracked specimens

The impact data from the pre-cracked specimens were furthermore analyzed according to the ISO 13586/17281 procedure. The provisional stress intensity factor was calculated for each group according to the procedure outlined in chapter 5.5.1 and is shown in Figure 5.28, alongside the corresponding time-to-fracture. Only minor influences on K_c of process conditions and loading direction are seen. A test against the size validity criterion of the standard (equation 13) using the specimen thickness of 1.5 mm results in a minimum yield stress requirement of 116-128 MPa in order for the K_c values found to represent the plane strain condition. A comparison with the yield stress from the data sheet reveals that the 1.5 mm thickness clearly is below the thickness requirement, in agreement with the conclusion of Hashemi *et al.* [62]. The values found here are close to the value of 3.3 MPa√m estimated for this condition in chapter 5.6.1. Evaluated at the linear part of the force vs. corrected displacement curve, the loading condition may be characterised by a K-rate of 5.7-6.3 MPa√m/s. Comparing with the K_c value found in chapter 5.7.8 for the grade with laser additive still suggests a slight toughness reduction from the additive (2.7 with additive vs. 3.0 MPa√m without for same loading direction and similar process), though not more than what might be related to measurement uncertainties. The two grades may qualitatively be compared simply by means of the recorded force traces – Figure 5.29 – since they were tested under the same conditions. This comparison yields the same conclusion as suggested by K_c, but also rules out a large reduction in deflection-to-break from the laser additive, as suggested in chapter 5.7.8. The deflection-to-break is simply much lower than anticipated in chapter 5.6, in agreement with the very high modulus of elasticity found in chapter 5.7.8, which clearly is of the same order of magnitude for the pure grade.
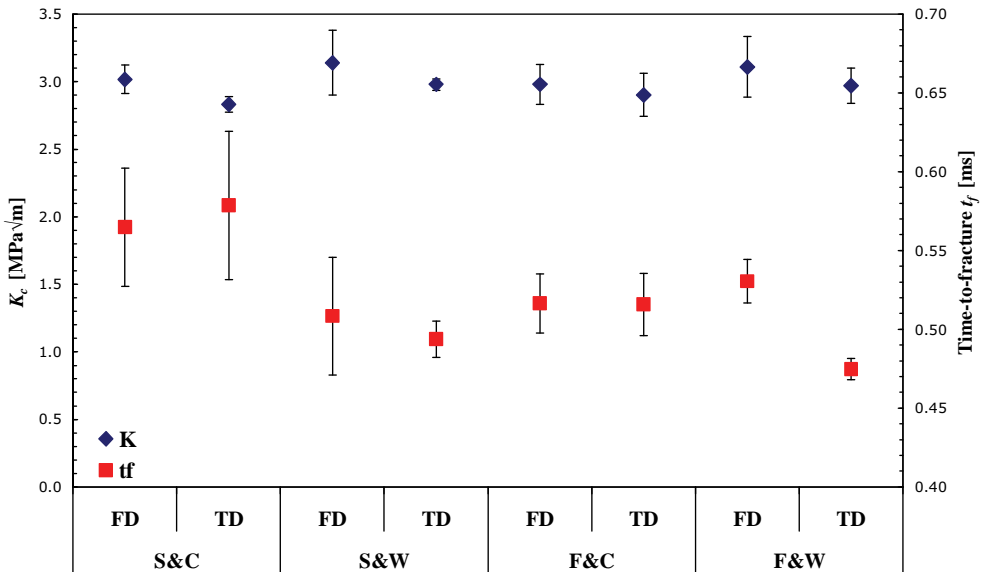
Figure 5.28: K_c and time-to-fracture from ISO 17281 analysis of pre-crack data.
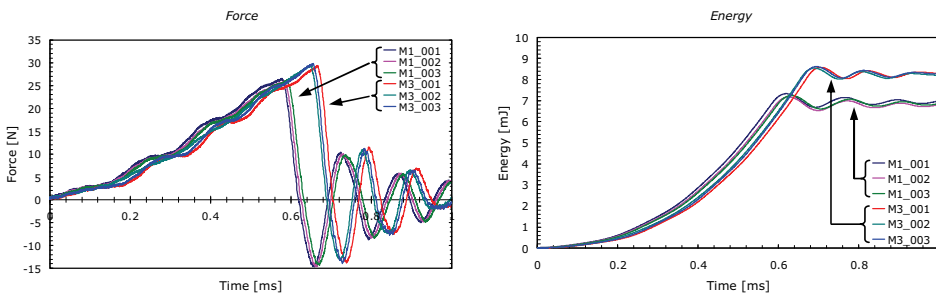
Figure 5.29: Comparison of force (left) and uncorrected energy (right) for grades M1 = neat POM, and M3 = pure POM, i.e. the material with and without laser additive, respectively.

5.8.5. Comparison with quasi-static SENB flexure

Quasi-static SENB flexure tests were carried out for the specimens with moulded-in notch to compare with the impact data. The tests were performed on a screw-driven Lloyd LF Plus tensile testing machine using the same support rig and striker geometry as used for the impact tests. The tests were performed at 10 mm/min, i.e. a factor of 6,000 slower than the impact tests. Specimens were prepared by the same procedure as used for the impact testing specimens – chapter 5.8.2. No damping pad was needed and the deflection measure taken from the crosshead position is thus only in excess of indentation of striker and support pins into the specimen. Since these two contributions are kept small by the relatively large radius of the striker and support pins (3 mm), the stiffness at

the point of highest slope should represent the flexural modulus of elasticity quite well. An example of force-displacement curves for the two directions are shown in Figure 5.30, together with the curves from the corresponding impact tests (specimen condition VS&VC, i.e. highest δ-thickness cf. 4.1). Note that the specimen tested in the flow direction did not fracture within the 6 mm deflection limit set, clearly showing its superior toughness (only the VS&VC condition gave 'no-break' results). In addition to the differences in stiffness and, presumably, yield stress (difficult to quantify directly from these data in a meaningful sense), it may especially be noted how the impact condition renders the fracture of the TD specimen truly brittle, whereas the quasi-static loading leads to appreciable plasticity prior to fracture. Moreover, the energy absorbing capability is severely reduced under the impact loading in either direction.
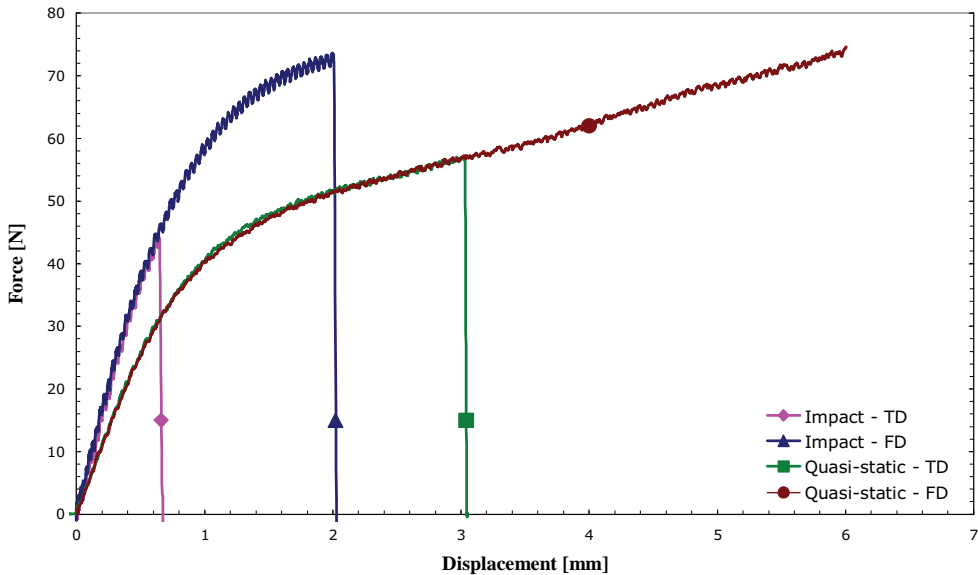
Figure 5.30: Comparison of force-displacement curves for specimens from process condition VS&VC with moulded-in notch tested under quasi-static and impact SENB flexure. The impact data are after displacement correction by the DIC method described in chapter 5.8.3. The quasi-static test of the FD specimen was terminated at a maximum displacement of 6 mm, corresponding to 38 s, without fracture of the specimen. The time-to-fracture t_f in the corresponding impact test (FD) was 2.4 ms.

The apparent flexural modulus for each condition was calculated from the (uncorrected) linear stiffness S and an S/E-ratio of 0.024 mm, found through a plane stress FE analysis[A]. The moduli are shown in Figure 5.31. The scatter in the data is quite high, but good correlation with the data sheet value of 2.7 GPa is found. The data shows a trend regarding processing conditions, correlating with an increase from decreasing δ-thickness and increasing optical anisotropy (chapter 4). The higher modulus in the transverse direction found for the VS&VC and VF&W conditions are in agreement with the findings of Bowman [35].

[A] Finite element analyses in ABAQUS by Laurits Højgaard Olesen, Device Simulation at NNAS.
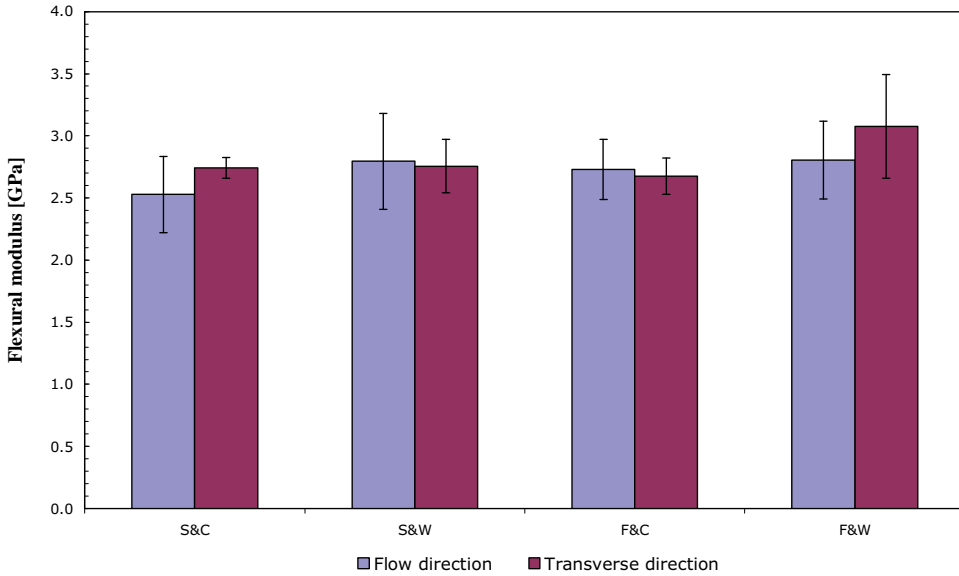
Figure 5.31: Apparent flexural modulus from quasi-static SENB flexure.

Figure 5.32 compares maximum force across the conditions with the corresponding values from the impact tests. The levels of maximum force are strikingly alike, and there is no overall trend regarding which loading rate results in the higher maximum force (or stress or stress intensity). There is a trend towards less anisotropy under quasi-static loading than under impact, and that this effect is decreasing with increasing δ-layer thickness, i.e. showing little difference in anisotropy for the VS&VC condition. Viana [9] found for a similar system (injection moulded POM in 1.5 mm thickness) a strong increase in quasi-static anisotropy of K_c from a tripling of the melt flow. A trend in this direction is not seen from these data, where the contrary is found for the cold moulding condition. This again suggests different mechanisms of process dependence resulting from the δ-layer and the core.
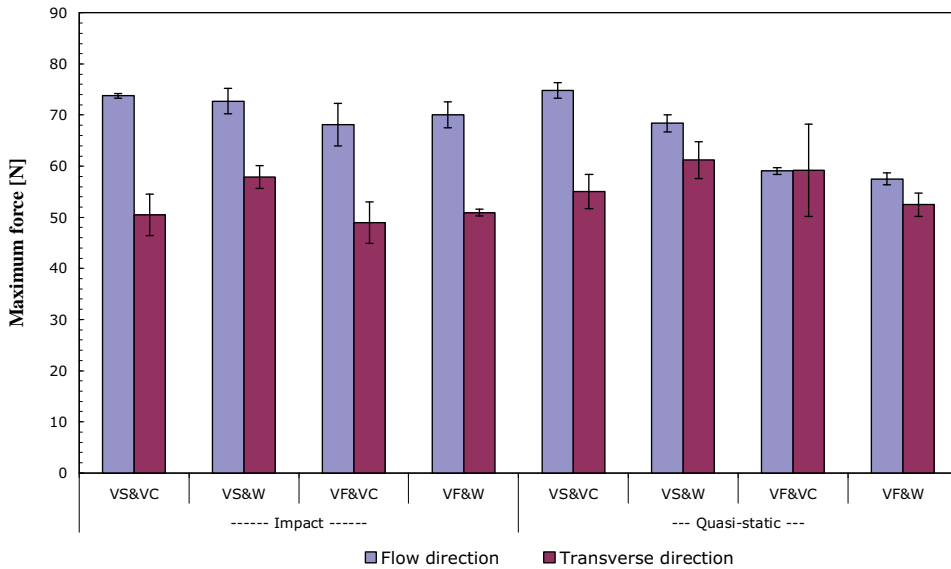
Figure 5.32: Comparison of maximum force from flexure tests under impact and quasi-static conditions. Value for VS&VC in flow direction under quasi-static loading represents the force at 6 mm load-point displacement, rather than at fracture initiation.

Figure 5.33 shows the deflection at maximum force for the quasi-static tests. The dashed horizontal line represents the test limit of ~6 mm, within which all but the VS&VC-FD specimens fractured. A comparison with the impact testing data is not made, since the corrected deflections for these have not been derived for all conditions[A]. The data show a high dependence on both process condition and loading direction. The high degree of scatter in the TD-data compared to the FD-data suggests either a difference in the local distribution of flaws around the notch root or a higher flaw tolerance in the FD direction. It may also be noticed, that the VF&W condition results in the lowest deflection-at-break (and hence strain-at-break) in both loading directions. This was the condition that showed the thinnest δ-layer, but also the highest birefringence in the skin in the PLM investigation in chapter 4.1. A negative effect of a highly oriented skin layer on the ductility is in agreement with the findings of Viana *et al.* [2] for injection moulded PP.

[A] The method of obtaining the corrected deflections described in chapter 5.7.8 is rather time-consuming and was therefore only used when needed for the energy corrections cf. the description. For the other conditions the standard ISO 17281 approach was used, which does not involve the determination of the corrected displacement function.
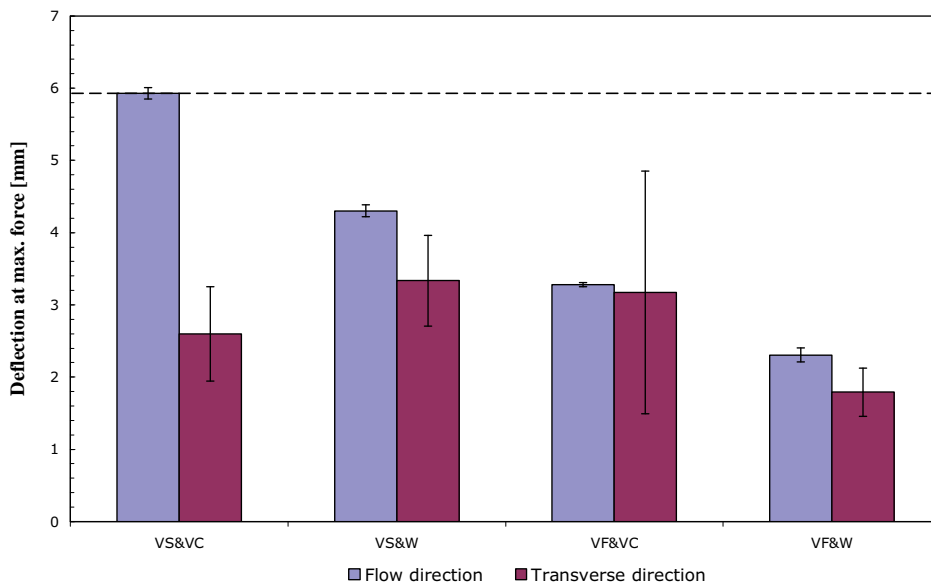
Figure 5.33: Deflection at maximum force. The dashed horizontal line at ~6 mm represent the deflection limit on the support fixture. The FD-specimens of the VS&VC condition did not fracture within this limit.

The energy to maximum force is compared for the two loading rates in Figure 5.34. The higher scatter in the quasi-static data may be ascribed to the deflection-at-break, which, contrary to expected, was found to vary less under the impact condition. For the TD-specimens the rate change corresponds to a difference in failure type, brittle vs. ductile-brittle, where the latter apparently leads to a higher sensitivity in this measure towards inherent flaws. The two loading rates show same trends, but the relative differences between the process conditions are much more pronounced for the quasi-static loading. This is contrary to the findings of Viana *et al.* [1] for injection moulded PP, where both strain-at-break and corresponding energy was found to depend more on process conditions at impact rates. The anisotropy is highest under impact rate for the VS&W, VF&VC and VF&W process conditions. Since the quasi-static tests for the VS&VC-FD specimens were stopped prior to break, it could possibly be the other way around for this process condition. The quasi-static loading definitely also leads to high anisotropy for these specimens. The impact rate fractures generally takes place after much lower amounts of energy absorption, with the exception being the VF&W process condition. The thin and highly oriented δ-layer of these specimens seem to result in low toughness regardless of loading rate. This implies that the rate-dependence in toughness is caused by a high extent of the δ-layer, rather than by a high maximum degree of orientation.
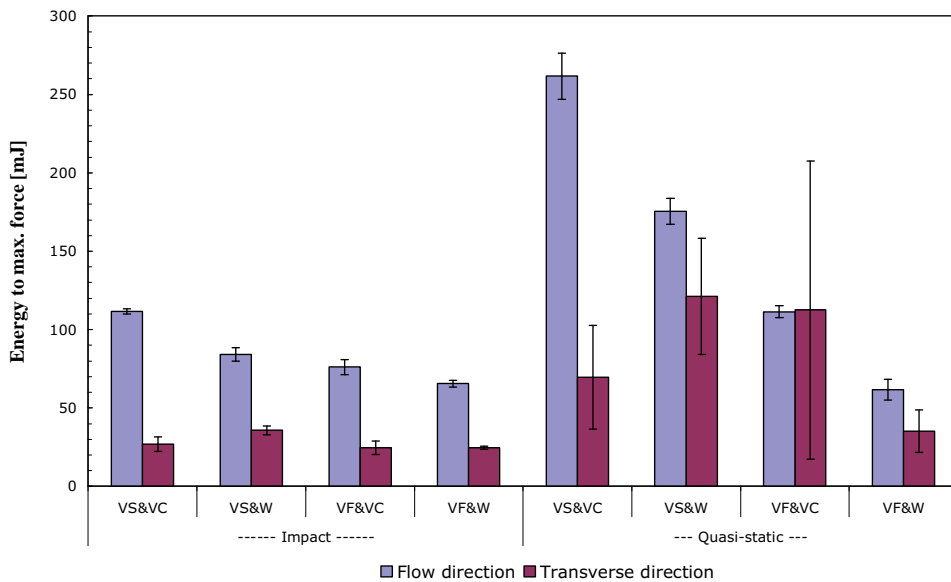
Figure 5.34: Comparison of energy to maximum force for the flexure tests under impact and quasi-static conditions. Note that the quasi-static tests for VS&VC-FD were stopped prior to fracture.

5.8.6. Fractography

Fracture surfaces were investigated by SEM fractography for comparison. Examples are shown in Figure 5.35-Figure 5.40. The plastic zone could be identified for all specimens. The position of this zone was found to depend strongly on the loading direction for both testing approaches. For the FD-specimens with moulded-in notch the fracture was found to initiate in the core, whereas the fracture of the similar TD-specimens was found to initiate in the skin. This is consistent with the findings from the out-of-plane impact bending in the Additives & Impact Study. It clearly reveals the high extent of anisotropy of the skin or δ-layer, being stronger than the core material only when loaded in the direction of the flow-induced orientation. Its low strength in the transverse direction leads to surface crazing for the TD-specimens with a thick δ-layer (Figure 5.38), in agreement with the observations of Bowman [35]. Comparing Figure 5.36 and Figure 5.38 reveals a geometrical difference in the notches from the VF&W and VS&VC process conditions. The low melt viscosity of the former is seen to cause a slight flash tendency, which clearly is not seen for the specimens of the latter process condition. Figure 5.36 shows fracture initiation in this thin edge, whereas its absence in Figure 5.38 may be the cause of the plastic line zone observed here. Böhme [34] reports a similar crack-inducing effect of flash.

Figure 5.39 and Figure 5.40 shows fracture surfaces from the pre-crack specimens of the VS&VC process condition. In the FD loading direction the largest depth of the plastic zone is seen in the core material. This clearly reveals a higher yield stress in the δ-layer, since the opposite is expected from a constraint point-of-view. This is found for the TD-specimen, with large crazing zones in the δ-layer in both sides. Consistent conclusions regarding the cause of the anisotropy are thus found for both impact approaches.
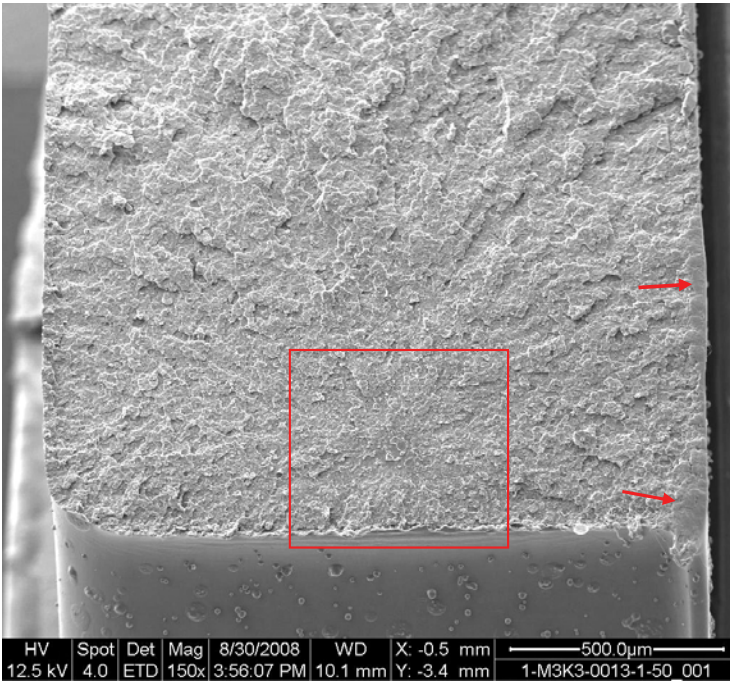
Figure 5.35:
Pure POM VF&W-FD
with moulded-in notch.
The notch is in the bottom
of the pictures and the
striker hit the specimen
from above. The red square
(upper) indicates the
position of the close-up
(lower). The arrows in the
upper picture indicates
bruises from contact with
the floor. The ellipse in the
close-up indicates the
plastic zone, showing
evidence of a craze-like
crack initiation (multiple
cavitation).
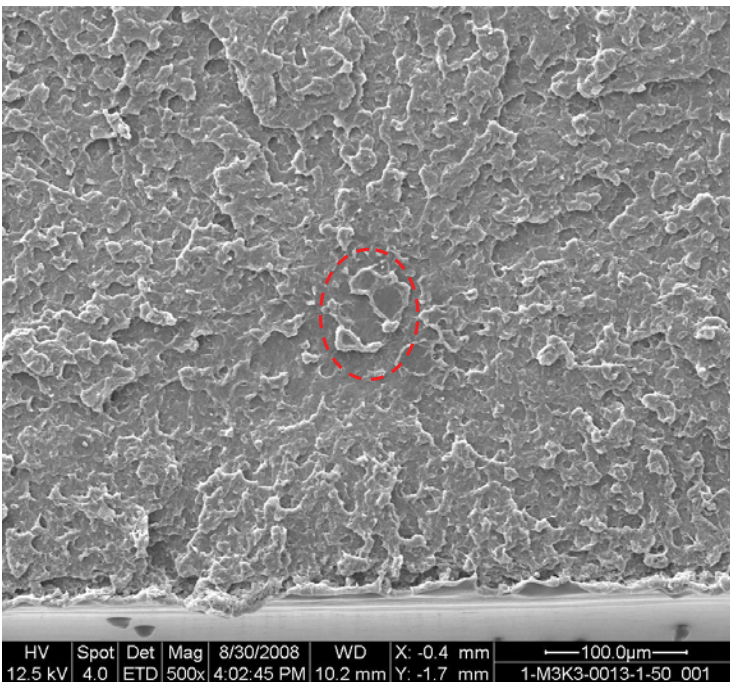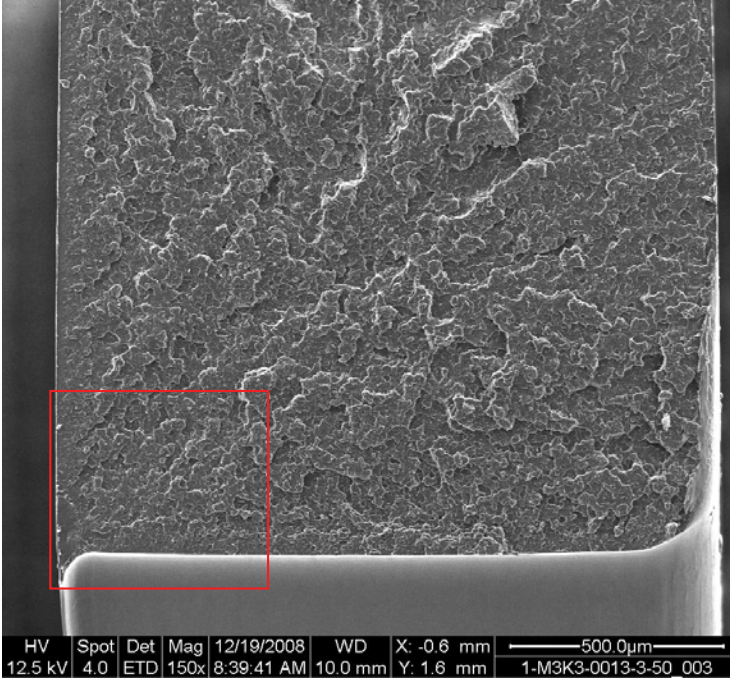
Figure 5.36:
Pure POM VF&W-TD
with moulded-in notch.
The notch is in the bottom
of the pictures and the
striker hit the specimen
from above. The red square
(upper) indicates the
position of the close-up
(lower). The semi-ellipse
in the close-up indicates
the approximate extent of
the plastics zone. The
arrow indicates a zone
showing craze remnants.
Notice the sharp edge in
the lower-left corner,
indicating a tendency
towards formation of flash
with this process condition.
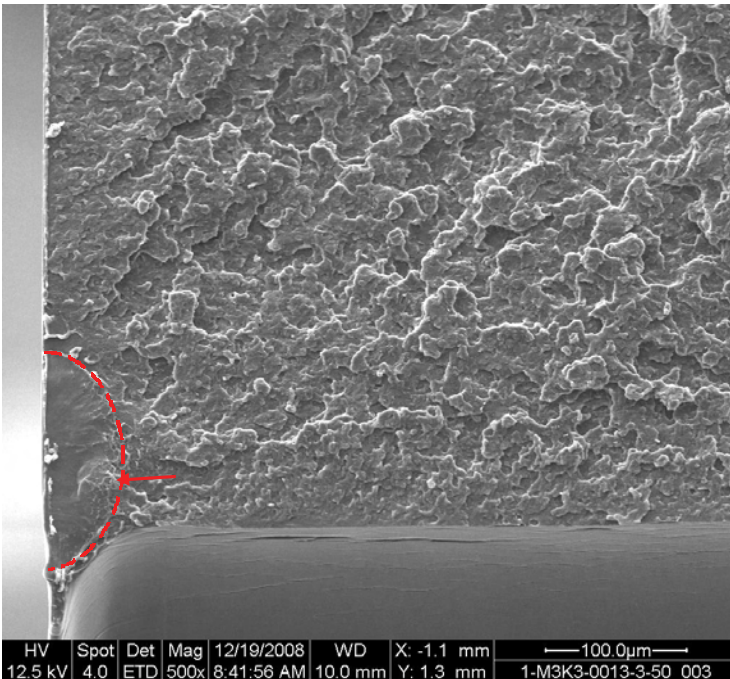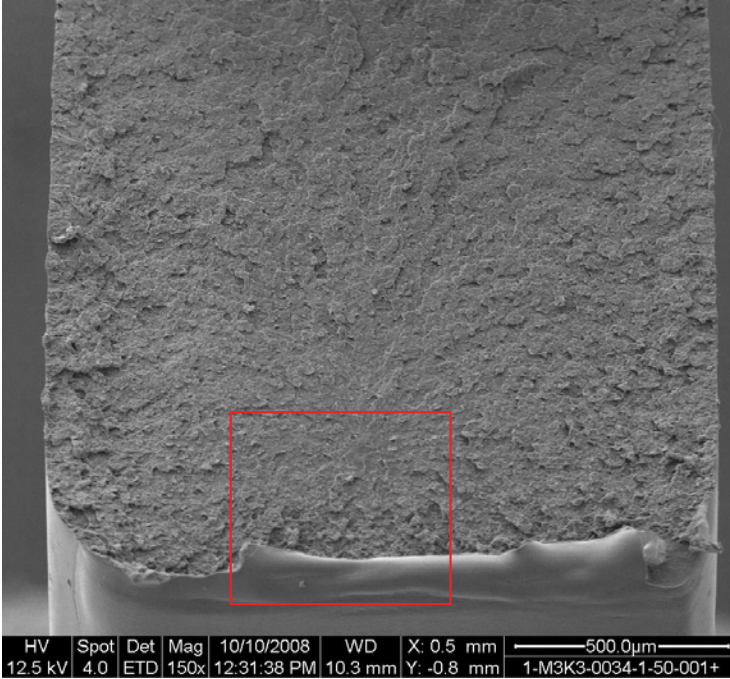
Figure 5.37:
Pure POM VS&VC-FD
with moulded-in notch.
The notch is in the bottom
of the pictures and the
striker hit the specimen
from above. The red square
(upper) indicates the
position of the close-up
(lower). The ellipse in the
close-up indicates the
position and extent of the
plastics zone, which shows
no evidence of crazing.
Notice the 'lip' of skin in
the bottom.
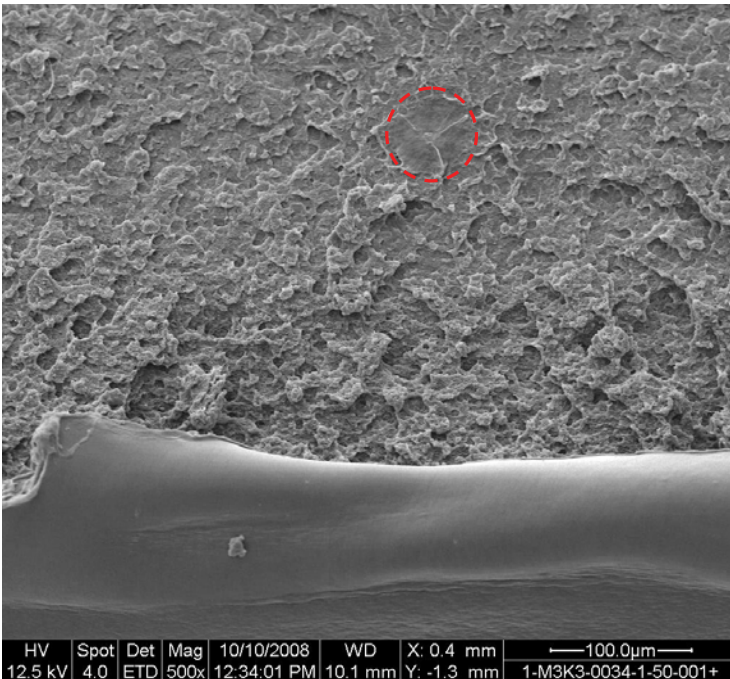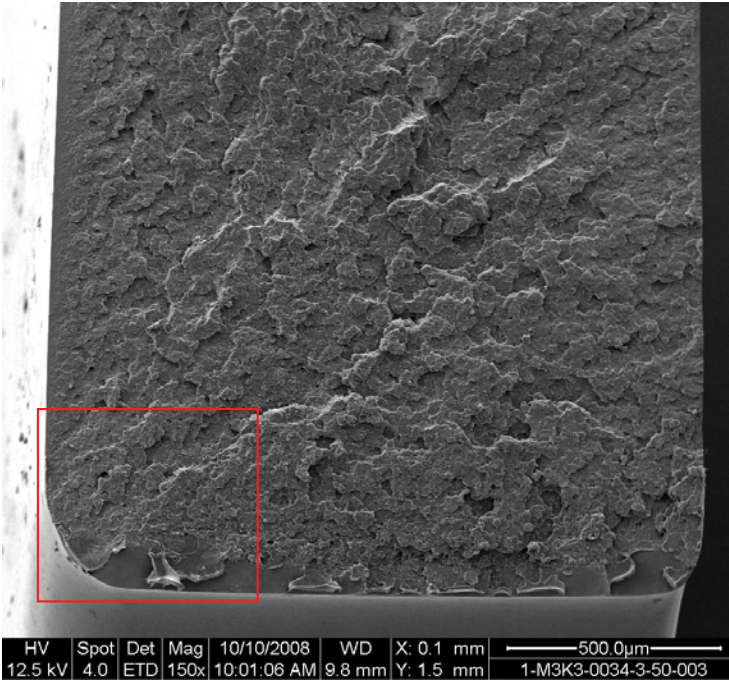
Figure 5.38:
Pure POM VS&VC-TD with moulded-in notch. The notch is in the bottom of the pictures and the striker hit the specimen from above. The red square (upper) indicates the position of the close-up (lower). Multiple crack initiation sites are seen along the notch root, with the material here showing evidence of positions of very low coherence. Notice the absence of the sharp edge in the corner found for the VF&W process condition, and the coarseness of the fracture surface topography compared to the FD-specimen (Figure 5.37).
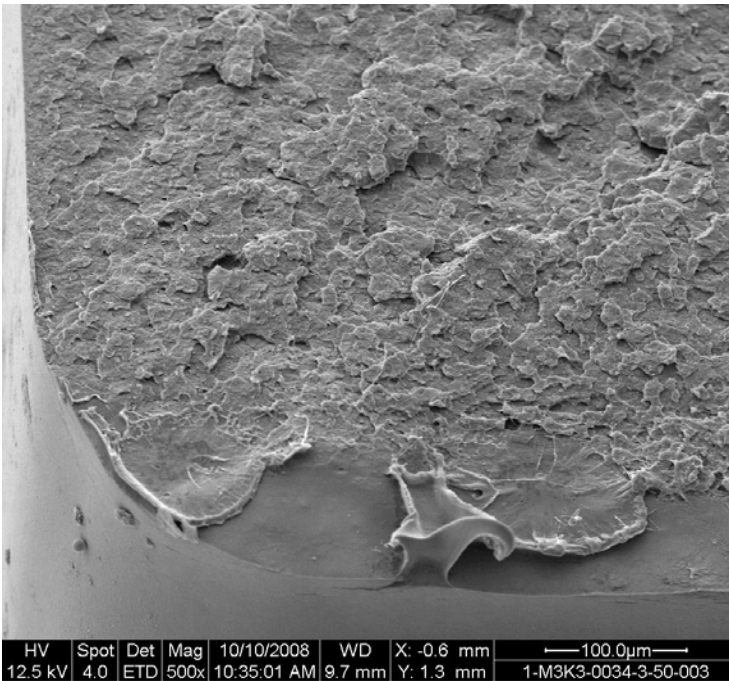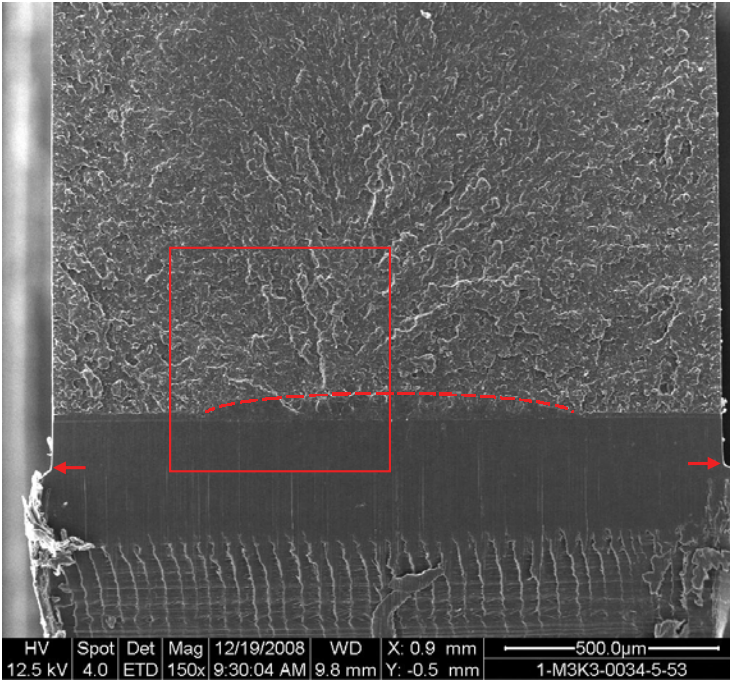
Figure 5.39:
Pure POM VS&VC-FD with pre-crack. The pre-crack is in the bottom of the pictures and the striker hit the specimen from above. The red square (upper) indicates the position of the close-up (lower). The dashed line indicates roughly the extent of the plastic zone, being almost constant in depth to approx. 300 µm below the moulded surface and increasing in depth in the centre of the specimen. The arrows in the upper picture indicates the depth of the milled sharp notch, those in the lower picture the end depth of the pre-cracking by razor-blade.
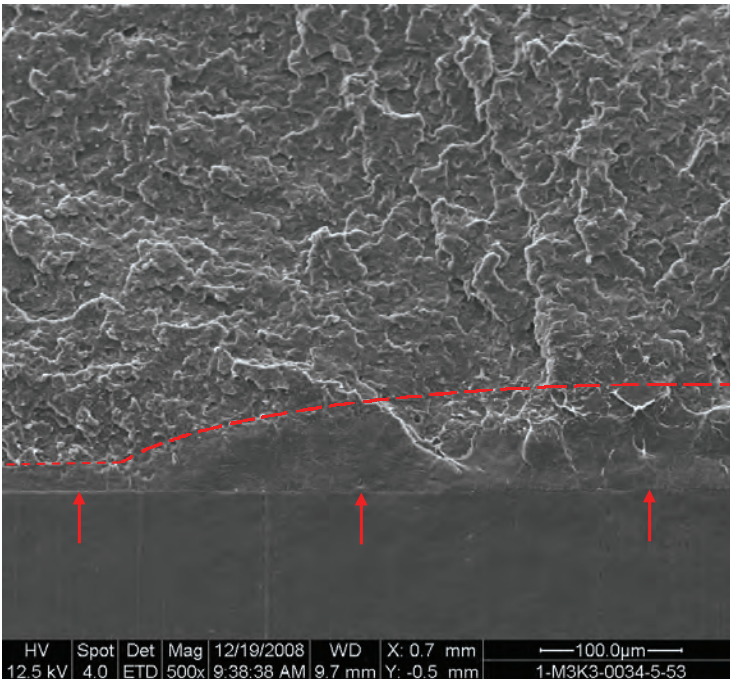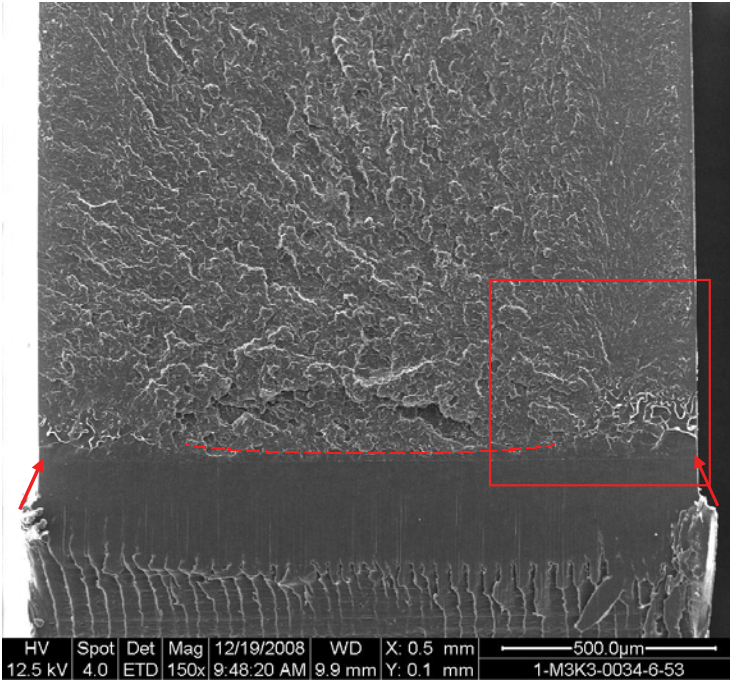
Figure 5.40:
Pure POM VS&VC-TD
with pre-crack. The pre-crack is in the bottom of
the pictures and the striker
hit the specimen from
above. The red square
(upper) indicates the
position of the close-up
(lower). The arrows in the
upper picture indicates a
plastic zone in both
corners. The arrows in the
close-up shows the
approximate extent the
plastic zone in the right-
hand side, clearly showing
evidence of crazing. The
extent of this craze zone in
the horizontal direction
compares well the zone of
least plasticity in FD
specimen (Figure 5.39).
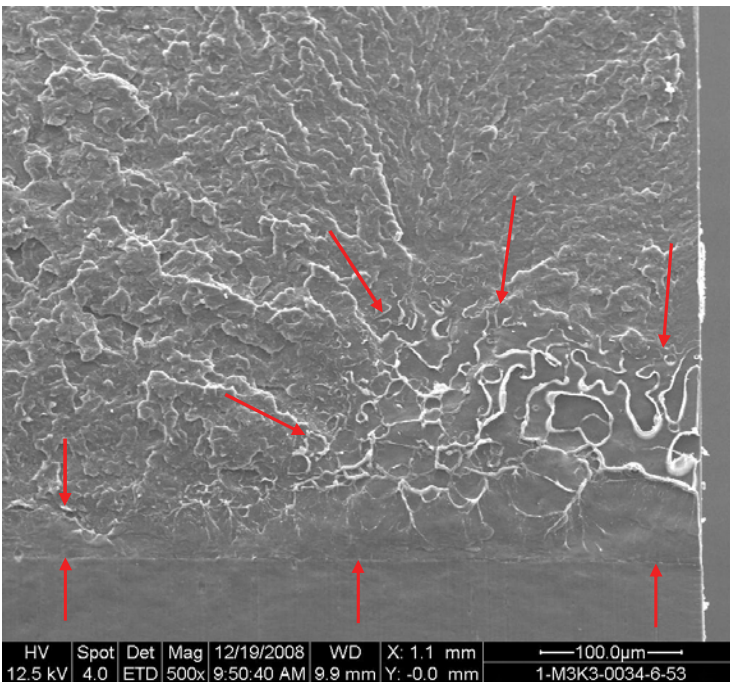
5.8.7. Main conclusions

The following main conclusions may be drawn from the impact testing part of the Impact & Indentation Study:

- Impact testing with a pre-crack lead to brittle fracture regardless of loading direction. With a moulded-in notch fracture in the FD-specimens were preceded by a highly non-linear behaviour.
- Impact testing with a pre-crack showed little or no influence of process and loading direction on the force at fracture initiation. Impact testing with a moulded-in notch revealed a high influence of loading direction on this measure, and also a significant process dependence in the TD loading direction.
- Impact testing with a pre-crack showed a small influence of loading direction and process conditions on the energy to cause fracture initiation. Impact testing with a moulded-in notch revealed a very high extent of anisotropy and process dependence of this measure.
- When loaded parallel to the melt flow direction highest energy at fracture initiation was found from using the low melt flow and mould temperature. Loaded transverse to the melt flow direction the highest value was found from the low melt flow and warm mould.
- The critical stress intensity factor was found from the pre-crack tests to vary between $K_c =$ 2.8-3.2 MPa√m, with only a slight dependence on loading direction. The values were found not to fulfil the plane strain size requirement for LEFM testing.
- Average J_c-values were found in the range of 2-2.4 kJ/m^2, all values fulfilling the plane strain size requirement for this method. J_c therefore seems to be a valid toughness parameter for POM even in this 1.5 mm thickness, making it suited for evaluation of process dependence and anisotropy under realistic material conditions. The same may not be done in terms of force at fracture initiation.
- A comparison with quasi-static loading of specimens with moulded-in notch revealed a higher degree of process dependence for the force at fracture initiation under this condition. The general force level was similar for the two loading rates. The energy to fracture initiation was found to depend more on process conditions under quasi-static loading than under impact, but showing the same trends. The impact rate reduced the toughness for all but the specimens of high melt flow and mould temperature, which were the most brittle under all conditions.
- Fractography of the impact tested specimens showed that the fracture initiation site changed from the core when straining the material in the flow direction, to the skin when loading perpendicularly thereto. Comparison of fracture surfaces for both loading directions and impact approaches pinpointed the δ-layer as the source of anisotropy and process-dependence.
- A comparison with the pre-crack data from the Additives & Impact Study suggests a slight embrittlement from the laser additive in the neat grade.
- The pre-crack method seems appropriate for obtaining lower-bound values of impact fracture toughness. The performed impact tests imply, however, that for the evaluation of process-dependence and anisotropy of impact performance, testing on specimens with a moulded-in notch will better reveal what will come to expression in a real thin-walled injection moulded component.

6. NANOINDENTATION

This chapter provides a brief introduction to nanoindentation and its applicability to mechanical characterization of polymeric materials. The term nanoindentation is used for depth-sensing indentation on both the micro- and nanometer scale, as it has become a common term in the literature. The chapter also accounts for the indentation part of the Impact & Indentation Study. Focus is only on the techniques I have used in the experiments in my project, which all have been carried out at the laboratories at MIT, USA. The treatment of the subject shall be seen in this light. For a more thorough treatment the reader is referred to the summary work of Fischer-Cripps [4] and the article of Van Landingham [81] for the applicability to polymers.

6.1. Introduction

Instrumented nanoindentation is characterized by micro or nanometer scale penetration of a hard indenter into a sample surface, with simultaneous measurement of applied force and resulting indenter displacement. The technique can be seen as a further development of traditional hardness measurement techniques like the Vickers method. Traditional methods characterize the material by only a single measure, e.g. the Vickers Hardness, corresponding to the maximum applied load. Nanoindentation on the other hand, provides the whole force-displacement curve of the indentation. It compares to getting the whole force-displacement curve from a uniaxial tensile test, rather than just the yield stress. Moreover, nanoindentation does not rely on a post-indentation measurement of the residual imprint to obtain the desired characteristic. Values of hardness and elastic modulus are typically obtained from the measured data by applying analytical contact mechanical solutions and an appropriate material model.

Nanoindentation of polymers poses several challenges compared to indentation of metals. The relatively low elastic modulus of polymers requires very small loads in order to make shallow indents. Shallow indents are often desired to obtain a high spatial resolution or is simply a requirement due to the displacement characteristics of the instrument used. Also, the viscoelastic nature of polymers generally calls for special methods applied to obtain the time-independent properties often sought: the hardness and modulus. Alternatively, more rigorous, time-dependant analyses have to be adopted to appreciate e.g. creep behaviour.

All indentations reported in this thesis have been made using the pendulum-based NanoTest600 nanoindenter (Micro Materials Ltd., UK). AFM-based nanoindentation was also tested in the early part of this project, but was soon opted out due to technical problems in relation to polymer indentation and lack of time. These exploratory studies are not reported in this thesis.

6.1.1. The NanoTest instrument

The NanoTest instrument is a dedicated nanoindenter and is designed to give a very well-defined movement of the indenter during measurement. The indenter is mounted on a (proportionally) large pendulum and the indenter movement can be considered normal to the surface of the sample, which is mounted vertically (see Figure 6.1). The pendulum can freely rotate about a friction-less pivot at its centre. A voice coil is mounted at the top of the pendulum and with a coil-current present the coil is attracted towards the permanent magnet, producing motion of the indenter towards and into the sample surface. The indenter displacement is measured by means of a plate capacitor, of which one plate is attached to the indenter holder, the other to the stationary machine frame. As the indenter moves, the corresponding change in capacitance can be measured as function of the applied coil-current. The equilibrium position of the pendulum with zero coil-current is adjusted with a

counterweight. A movable limit stop defines the maximum outward movement of the indenter and adjusts for different indenter lengths. Two closely mounted damping plates reduce pendulum vibrations prior to indenter-sample engagement. The sample is mounted on a stub, which again is mounted on a XYZ-stage. Precise sample manipulation is achieved by motor positioning with magnetic encoders.
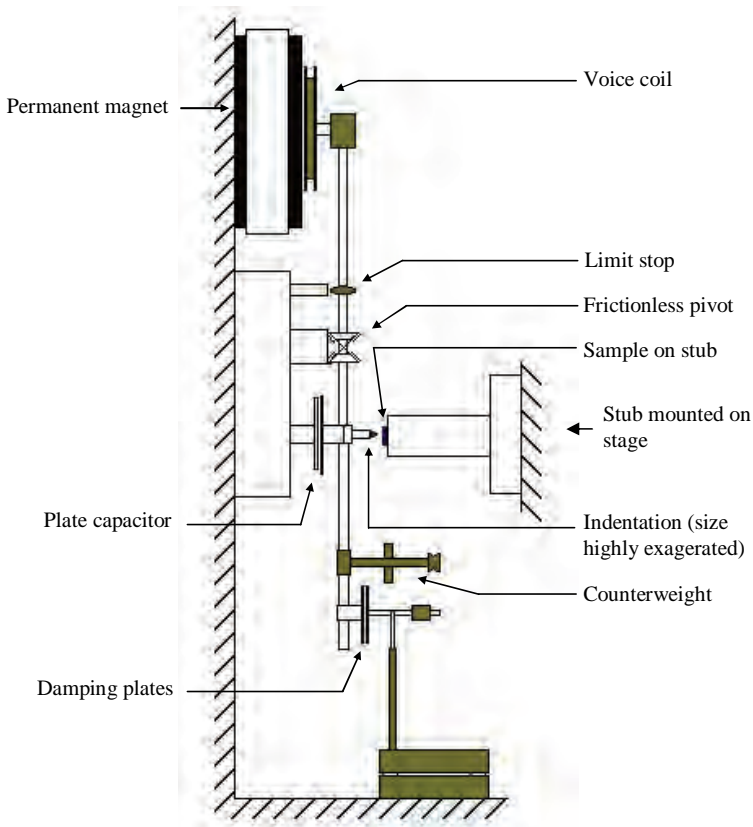
Figure 6.1: Schematic illustration of the NanoTest nanoindenter.

Indentations with the NanoTest instrument are made through a programming interface, where a loading rate, a load ramp termination condition and an unloading rate are specified. The primary advantages of the NanoTest instrument are its relatively large displacement and load capability, a well-defined indenter movement during indentation (required for qualitative measurements of absolute material properties), and that it can be programmed to run a series of indentation experiments without user intervention. Disadvantages are that the instrument is very slow (e.g. 10×10 indentations in ~14 hours in an automated setup), and that the combined optical microscope provides only a rather poor means by which a specific area of interest may be located for the indentation.

6.2. Extracting mechanical properties

The load-displacement curves may be analysed to provide genuine mechanical material properties. The common objective of nanoindentation is to determine elastic modulus and hardness. Determined in this way, these values are referred to as the indentation modulus and indentation hardness. They will not always be identical to the values determined by the methods of uniaxial tensile testing and e.g. Vickers hardness testing. Some reasons for observed discrepancies are discussed below, but the reader is referred to Fischer-Cripps [4] and Mencik [82] for a general treatment of the subject.

The standard method used at MIT and in most of the referenced literature for calculation of indentation modulus and hardness of polymers is that of Oliver and Pharr [83], described in the following.

The indentation modulus is determined from the unloading part of the indentation curve, assuming this accounts for purely elastic unloading only. At first the indentation data are corrected for load frame compliance so that it represents only the part related to the sample and indenter deformation. The corrected unloading curve is fitted with a power law function of the form

$$P(h) = \alpha \left(h - h_f \right)^m$$

Equation 25

where P is load, h is penetration depth, h_f is the final unloading depth, m is an exponent dependant on the indenter used and α contains effects of both geometry, and indenter and substrate materials.
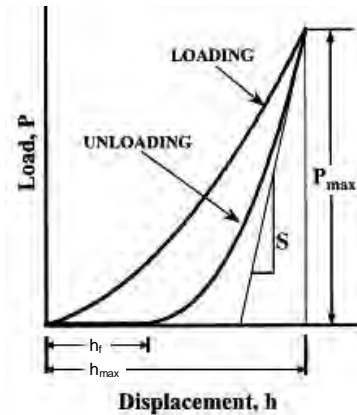
Figure 6.2: Force displacement curve for indentation.

The contact stiffness S is defined as the slope of the fitted unloading curve at maximum load and displacement:

$$S \equiv \left. \frac{dP}{dh} \right|_{(h_{max}, P_{max})} = \alpha m \left(h_{max} - h_f \right)^{m-1}$$

Equation 26

Oliver and Pharr showed how S relates to the so-called reduced modulus E_r through the following equation:

$$S = \frac{2\beta}{\sqrt{\pi}} E_r \sqrt{A_c}$$
Equation 27

where A_c is the projected area of contact and β is a parameter accounting for non-circularity of the indenter. A_c is found from an indenter area function (known as the diamond area function – DAF), which can be either an analytical term or a polynomial fit of reference data from indentations into a ductile material. A_c is evaluated at the contact depth h_c, which is determined from the maximum indentation depth h_{max} and the corrected contact stiffness S through

$$h_c = h_{max} - \varepsilon \frac{P_{max}}{S}$$
Equation 28

where ε is an indenter geometry function.

The reduced modulus E_r takes into account linear (!) elastic deformation of both sample and indenter materials through the following equation, also accounting for the triaxial stress state imposed by indentation:

$$\frac{1}{E_r} = \frac{1 - v_s^2}{E_s} + \frac{1 - v_i^2}{E_i}$$
Equation 29

Here subscripts s and i represent specimen and indenter values of Poisson's ratio v and Young's modulus E, respectively. The sought indentation modulus is thus determined as E_s. Diamond indenters have been used for all the reported indentation data in this thesis, with the following elastic values: $E_i = 1140$ GPa and $v_i = 0.07$. A Poisson's ratio for copolymer POM of $v_s = 0.35$ has been assumed.

With the contact area A_c defined above, determining indentation hardness is straightforward from the definition of the so-called Meyer hardness

$$H \equiv \frac{P}{A_c}$$
Equation 30

where P then is taken as the force at maximum depth, P_{max}.

It is here worth noting how hardness determined this way is linked to the determination of the corrected contact stiffness S through the determination of the projected contact area A_c. Moreover, it should be noted that determination of hardness, the traditional concept defined as the ability to withstand plastic deformation, requires, said, plastic deformation. In praxis a fully developed plastic zone is assured when hardness is sought through relatively deep indentations and/or acute indenters.

The above solutions assume negligible friction between indenter and substrate, and a fully developed plastic zone. Under these assumptions the yield stress may be approximated from the Meyer hardness as:

$$\sigma_y \approx H/3$$
Equation 31

For materials with a low E/σ_y-ratio the constraint factor imposed by the elastic stress field may not be as high as 3. Mencik [82] reports an approximate iterative scheme for finding the appropriate constraint factor (and hence yield stress) when $1.1 < H/\sigma_y < 3$

$$\frac{H}{\sigma_y} \approx \frac{4}{3} + \frac{2}{3} \ln\left(\frac{5E\varepsilon_{rep}}{3\sigma_y}\right)$$
Equation 32

where ε_{rep} is the representative strain of the indenter – see chapter 6.3.1.

An elasticity index η_e is defined as the ratio of elastic work to total work:

$$\eta_e = \frac{U_e}{U_e + U_p}$$

Equation 33

Note that the work designated as being plastic also contains any viscoelastic contributions on timescales longer than the effective time of the indentation.
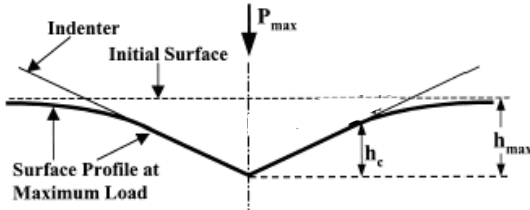
Figure 6.3: Cross-section through an indent with an obtuse indenter, showing the elastic sinking-in of the material.

6.3. Practical considerations

6.3.1. Indenter geometries

Different indenter geometries are used for different purposes. The geometries may be divided into blunt and pointed indenters. Blunt indenters are typically in the shape of a sphere or a cone ending in hemisphere. They are used for shallow, purely elastic indentations or deeper indentations to increasing maximum strains. Pointed indenters include the modified Berkovich pyramid – see Figure 6.4 – and the four-sided pyramid. The former has been used for all the reported investigations in this thesis. The modified Berkovich geometry is an obtuse, three sided pyramid with a face angle α of 65.27°, resulting in a width of the indent of approx. 7 times the depth. For the ideal pyramidal geometry the representative strain in the substrate is independent of the indentation depth. Real Berkovich pyramids have tip radii of the order of 50-100 nm when new and impose a representative strain of approx. 7%. The intercept and geometry correction factors ε and β are 0.75 and 1.034, respectively. The ideal indenter area function is given by:

$$A_c(h_c) = 24.5 h_c^2$$

Equation 34

Figure 6.4: The Berkovich pyramid as schematic (left) and measured (right).

Further indenter geometries are described in the reference by Fischer-Cripps [4].

6.3.2. Viscoelastic properties and corrections

Viscoelasticity will increase the initial slope of the unloading curve. Often the material creep faster than the load is being removed and a negative contact stiffness will be measured. This renders the Oliver & Pharr analysis (6.2) inapplicable. To get around this problem a dwell period at maximum load is often adopted – Figure 6.5. With 30 seconds of controlled creep, i.e. under constant load,

many polymers will effectively increase the time scale of additional creep to where it is no longer affecting the measured contact stiffness. If the creep rate after dwell is found still to be significant an approach of Feng & Ngan [84] (based on an assumption of linear viscoelastic creep) may be used to correct the stiffness.
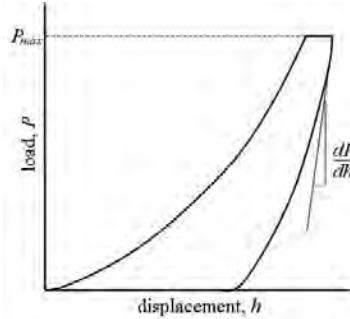
Figure 6.5: Principal load-displacement curve with dwell period at maximum load.

When interested in the time-dependant properties of a polymeric material, the creep behaviour is often what is sought. The contact creep compliance C_c may be calculated as given by Tweedie & Van Vliet [85] for cone-equivalent indenter geometries (like pyramids):

$$C_c(t) = \frac{8\tan(\alpha)h^2(t)}{\pi P_0} \qquad\qquad \text{Equation 35}$$

where P_0 is the constant force at dwell. Solutions for other geometries and other means of contact creep characterisation are given in [4;86].

A more rigorous approach to characterisation of the viscoelastic properties of plastics is through dynamic mechanical analysis (DMA). This experimental technique may also be applied on the micro or nano-scale using certain nanoindentation instruments. nanoDMA has not been used in this project and the reader is referred to Fischer-Cripps [4] for a further description.

6.3.3. Sample preparation and length-scale considerations

Specimen preparation for nanoindentation is critical and turned out to be quite a challenge with the polymer of this project. Surface roughness is stated Fischer-Cripps [4] to result in artificially low values of the measured indentation modulus. This effect must, however, depend strongly on the indenter used and the ratio of length scales of the roughness, and one can easily imagine situations where the opposite would be the case. Significant surface roughness will under all circumstances add to the measurement variation and uncertainty, and care must therefore be taken to minimize such artefacts.

The primary objective of the indentations made in this project have been to characterise the mechanical behaviour of the outer layers of the microstructure. The first approach investigated was to expose a cross-section of the specimen and to make indents across the thickness. Specimens were embedded in a cold-curing epoxy, cut with an abrasive wheel cutter to the approximate depth of the desired cross-section, and then ground and polished. The standard procedure used in the department at NNAS had been developed for geometrical measurements on exposed cross-sections and turned out to be inadequate for this purpose. Different alternatives were tested and a useful technique was

finally derived, consisting of four grinding steps (grit 500, 1000, 2400 and 4000) and subsequent polishing with a colloidal silica suspension (0.04 µm). The specimens were washed in demineralised water in an ultrasound cleaner between each step to remove debris and loose abrasives. It was found essential to use also demineralised water for the 2400 and 4000 grit grinding steps in order to avoid particle contamination from tap water leading to scratches.

An indentation size artefact may potentially arise from cold-working of the outermost material during polishing. Fischer-Cripps [4] estimates the depth of the affected zone to be of about the same size as the nominal grit used. This and the 1/10-rule of Buckle suggests that artefacts from the surface preparation technique described above may be avoided by keeping the indentation depth greater than 0.4 µm, provided that all artefacts from earlier grits are effectively erased by the next step of preparation. All indentations made with the NanoTest instrument comply with this conservative approach.

A certain minimum distance from an indention to any discontinuities in the material is required in order for the measured response not to be affected by its proximity. The rule of thumb used for polymer indentations in the group at MIT was to keep a minimum distance to the specimen boundaries or imprints from other indentations of ten times the width of the indenter at the depth of indentation. This rule of thumb was used for deciding on grid spacing and minimum distance to the specimen edge in this project.

6.3.4. Fracture mechanical testing by indentation

Indentation with sharp indenters into brittle materials can lead to cracks forming at the corners of the imprint. Several researchers have shown for ceramics that an analysis of the size and form of these cracks can provide for an evaluation of the fracture toughness. In a recent study Lach *et al.* [87] have evaluated different expressions for use with brittle polymers and concludes that the expression of Laugier [88] gives good agreement with results from standard fracture mechanical testing for various PMMA and PS systems. Indentation-induced cracks have not been observed in the POM materials tested in this project, neither has it been reported in the referenced literature for this material. In other words, POM is not adequately brittle under indentation conditions for this approach to be relevant for fracture toughness evaluation. The reader is referred to Fischer-Cripps [4] and Lach *et al.* [87] for further reading on this subject.

6.3.5. Standardization

At present no standardisation of depth-sensing indentation exist covering polymeric materials. ISO 14577 (parts from 2002-2008) covers metallic materials but had at the time of my stay at MIT not been adopted in their work, wherefore I have not taken offset in this standard for my indentation measurements. Instead I have used the common praxis in their labs, which differ little from the standard though.

6.4.   Reference data

Remond & Vedrines [89] have reported on the through-thickness gradient in the Young's modulus of injection moulded Hostaform POM of 3.1 mm thickness. The data, shown in Figure 6.6, were obtained by measurement of the change in resonance frequency with consecutive thinning of a moulded plate by milling. Their results show a distinct increase in modulus with increasing depth below the moulded surface. The level at ~0.5 mm depth is seen to be more than 50% higher than that of the surface layer. Moreover, there seem to be a maximum around this depth.
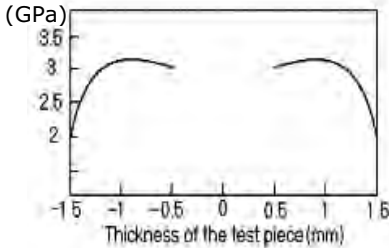
Figure 6.6: Variation in Young's modulus through the thickness of a 3.1 mm POM moulding. From [89].

Pistor & Friedrich [90] studied the scratch and indentation properties of a homopolymer POM injection moulded with mould temperatures of 20, 80 and 120°C, respectively. The indentations were made with a Vickers microhardness setup using a load of 1 N, providing a maximum indentation depth of 14-15 µm. Skin and core properties were measured on polished surfaces where approx. 1 µm and 1 mm, respectively, had been removed from the moulded surface. The skin layer measurements showed no effect of the mould temperature, even though the skin layer thickness (layer 1 in the description in chapter 4) was found to vary from 25 µm at a mould temperature of 20°C to non-existence at 120°C. The δ-thickness varied from ~250 µm to ~10 µm over the same mould temperature range. This finding suggests that the yield stress of the δ-layer is constant throughout and independent of the mould temperature. The core measurements showed a slight decrease in microhardness as the mould temperature increased, and at lower mould temperatures the hardness of the core was found to be higher than that of the skin. The latter indicates that a high yield stress is favoured by the lamella thickening resulting from the slow cooling in the core; the former, however, indicates the opposite effect. The experimental information provided in the article are too sparse for a further analysis and since only two repetitions of each measurement have been made the statistical foundation is also rather weak. The hardness values reported in the study compares approx. 360-410 MPa in Meyer hardness, i.e. to yield stress values well above 100 MPa.

6.5.   Exploratory indentation measurements of through-thickness gradients

During my three months stay abroad I tested various indentation techniques for measuring the variation in mechanical properties through the thickness of the outer layers of injection moulded POM. The following chapter presents some exploratory investigations on preliminary POM specimens, i.e. other than those reported on in the two primary studies.

Measurement of through-thickness gradients by depth-sensing indentation may be done either by indentations made directly on moulded surfaces to varying depths, or by making indentations across

the thickness of exposed cross-sections. The former approach requires a high surface quality as-moulded and was deemed less suited for studies with varying process conditions, since these inevitably will affect the surface quality of the mouldings. Moreover, this approach is expected to suffer from a decreasing sensitivity to local variations, since the volume of interaction is an increasing function of the indentation depth. With indentations on an exposed cross-section each depth below the moulded surface can be measured under the same indentation conditions, and the maximum depth will not be limited by the depth or force capabilities of the instrument. Based on this argumentation the latter approach was chosen as point of departure for the indentation measurements of the through-thickness gradients.

6.5.1. Exploratory measurements – part 1

The first measurements were made on an injection moulded component from the InnoLet® insulin pen (the injection mould of this project had not been made at this time). The component is made of a POM grade similar to the neat grade of the Additives & Impact Study. A structural link in the component was known to be highly birefringent, as revealed by the PLM micrograph in Figure 6.7.
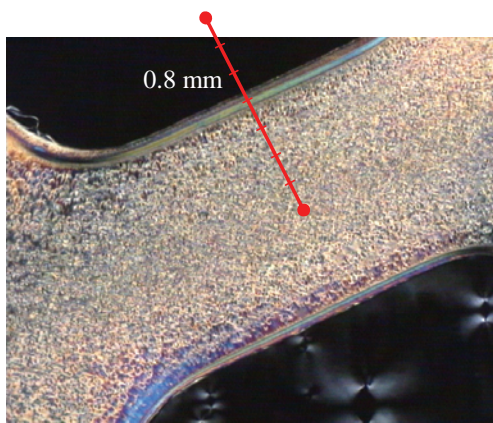
Figure 6.7: Pickup-arm link in the coupling ring for the InnoLet® device. The red line of 0.8 mm total length represents the approximate location of line of indentations.

The objective of the measurement was to characterise the change in elastic modulus, hardness and elasticity index across the width of the link cross-section, going through the different layers of the microstructure. The component was embedded in epoxy and a cross-section through the link was prepared according to the description in chapter 6.3.3, though with the original grinding and polishing technique used at NNAS. The NanoTest apparatus in its lowest load-setup (NT0) was used to make a line of 40 indents across the link, using a maximum force of 0.1 mN and spacing of 20 µm. The initial contact was detected at a pre-load of 5 µN and the load was applied and removed at 20 µN/s. 5 seconds dwell at maximum load was used and the resulting maximum depth of the indents was 100-210 nm. The characteristic data are shown in Figure 6.8. The values for positions less than approx. 200 µm represents the epoxy of the embedding. For 280 µm and above both indentation hardness and modulus are seen to be much higher, representing the response of the POM link. With the chosen depth of indentation (max. force) and spacing two indents at most might be directly influenced by the proximity of the epoxy-POM interface, qualifying the measurements below 240 and above 300 µm as representing the epoxy and POM, respectively. The elasticity index shows little effect on the position across the POM cross-section. The hardness data show high

scatter between 340 and 460 µm. This could indicate the position of a mechanically inhomogeneous layer of the microstructure. The general level of scatter as indicated by the supposedly homogenous and isotropic epoxy is however quite high as well, rendering a conclusion in this regard doubtful. A comparison with the microstructure shown in Figure 6.7 suggests that the inhomogeneity may stem from the comet spherulites in the rather coarse layer 4 (below the shear layer, cf. chapter 4). Local measurements of the mechanical properties in this layer might be highly dependent on the spatial position because of the relatively high amount of amorphous intercrystalline material. The measured hardness between 300 and 340 µm, corresponding to depths less than 60-80 µm below the moulded surface, is seemingly not very different from that of the core material. The average indentation hardness for these layers is 0.16 GPa. The indentation modulus shows relatively high scatter all across the POM link and no distinct layers can be identified from the response. The average indentation modulus of the POM material is 3.1 GPa, which is comparable to the data sheet tensile modulus of 2.85 GPa. The hardness is close to the ball indentation hardness of 0.144 GPa reported by the vendor [91]. The yield stress of 54 MPa found from the hardness of 0.16 GPa and equation 28 is somewhat below the uniaxial tensile yield stress of 64 MPa found in the data sheet. Taking the ratio E/σ_y suggests the use of equation 29 instead, which results in a constraint factor of 2.5 rather than 3, and a yield stress of 64 MPa. This suggests that the strain imposed by the Berkovich indenter is less than the strain at the yield point of the POM grade. A comparison with the data sheet value supports this conclusion (~7% vs. 9% from the data sheet), though the difference in stress state makes such a comparison doubtful.
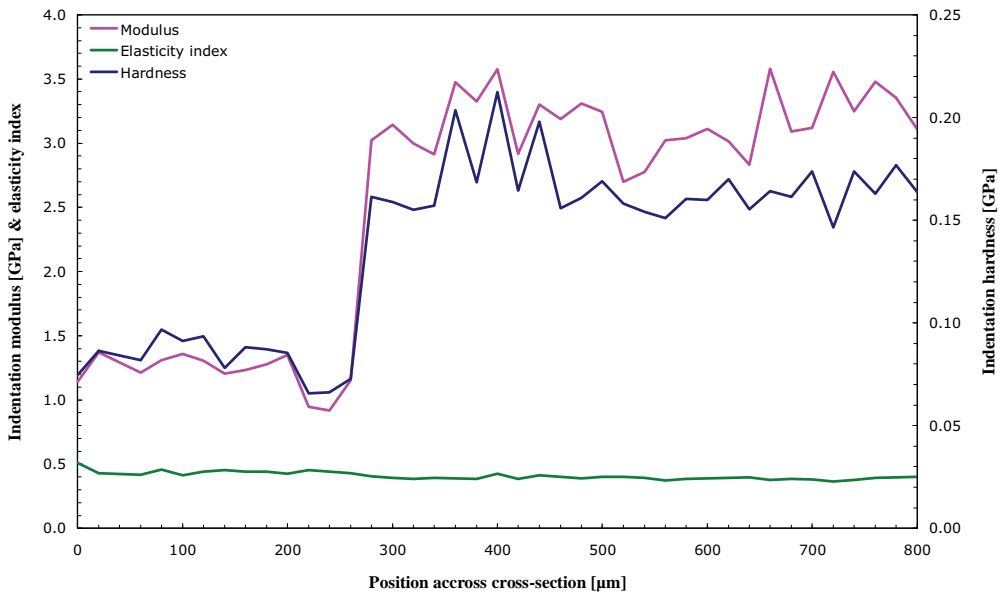
Figure 6.8: Indentation modulus and hardness, and elasticity index for measurements across an exposed cross-section of an epoxy-embedded POM component.

All in all, it may be concluded that the measured values are in good agreement with comparable values from the data sheet, but also that a positive separation of distinct microstructural layers will require a reduction of the general level of scatter. Moreover, a higher spatial resolution is desirable for characterisation of the outermost layers of the microstructure.

6.5.2. Exploratory measurements – part 2

The second round of measurements on the NanoTest instrument was made on exposed cross-sections of specimens from the Additives & Impact Study - Figure 6.9. The objective was to reveal differences in possible through-thickness gradients of the neat grade, resulting from the different process conditions used for this study. The preparation technique (chapter 6.3.3) had at this time been refined further in an attempt to reduce the general level of scatter. 10×11-grids were made on cross-sections close to the specimen edge, though this time not crossing the interface to the epoxy embedding. The indents were performed at a loading rate of 0.5 mN/s and were terminated at a maximum depth of 0.5 µm. Initial contact was detected at a load of 10 µN and a 30 s dwell period at maximum load was used. The general spacing was set to 35 µm cf. the description in chapter 6.3.3, but a cross-hair misalignment on the instrument microscope lead to the first and second rows having a distance to the interface of only 20 and 46 µm, respectively. Indentation modulus, hardness and elasticity index were calculated from the measured data as described in chapter 6.2 and are shown as contour plots for the four process conditions in Figure 6.10 and Figure 6.11. Note that all values on the abscissa (the depth below the moulded surface) are shown equidistant despite the smaller distance between the first two columns.

Figure 6.9: Position of indentation sample and tested cross-section in the moulded test blank.

The overall impression from the contour plots are a decrease in all three measures as the depth below the moulded surface decreases. This effect is most clearly seen for the elasticity index data, where process conditions S&W, F&C and F&W show a remarkable drop for the 20 µm depth. Process condition S&C, however, shows no depth dependence for this measure. This is contrary to what might be expected based on the assumed thickest skin and δ-layers of this process condition, suggesting a lack of correlation between the extent of the microstructural layers and the through-thickness gradient for this characteristic. Seemingly outliers are seen for all process conditions, but they may well simply be due to the laser additive present in this grade. The specimens from the F&C and F&W process conditions both show areas of the grid where the properties change remarkably in the direction along the specimen surface. All three measures show reduced values in these areas. The areas were examined using an optical microscope but this did not provide an

explanation to the difference in response. The areas did contain scratches, but seemingly not more or worse than in the other areas of the grid.

The elasticity index most clearly shows an effect of the proximity of the specimen edge, yielding a more viscoelatic or plastic response at the lowest depth below the moulded surface. The specimen moulded with the S&C process condition, however, does not show this effect. The most pronounced gradient in elasticity index is seen for the F&W process condition. This combination yielded the most birefringent skin layer in the Impact & Indentation Study. A correlation of this kind is also supported by the other process conditions, suggesting that the elastic capabilities of the material depends more on the molecular orientation than on the microstructure itself.

Standard rectangular grids were used for these indentations. A higher depth resolution (smaller spacing in depth direction) could have been used if the indents had been spread more in the direction along the specimen surface. Because of the relatively high extent of surface defects from the preparation technique it was decided, however, to keep the indents closely packed, to make it easier to avoid large defects when the grid layout was positioned on the surface. The minimum depth below the moulded surface is anyhow limited by the depth of indentation with this approach, rather than by the proximity of the other indents.

The F&C process condition shows a remarkable increase in indentation modulus at the lowest distance to the moulded surface. This has not been explained and the observation does not correlate with the systematic variation in elasticity index.
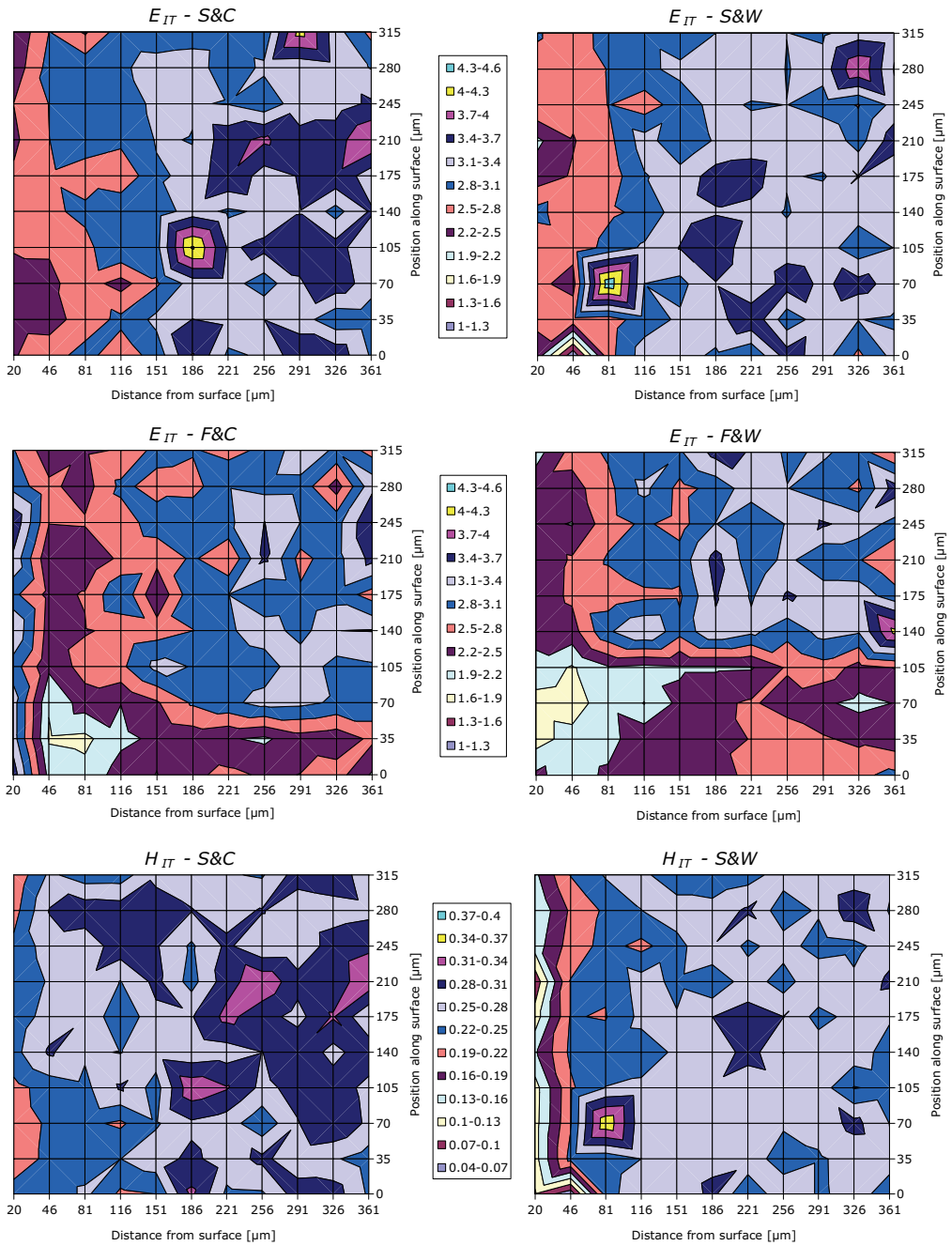
Figure 6.10: Contour plots of indentation modulus [GPa] (upper left to centre right) and hardness [GPa] (lower left to lower right) for the different process conditions (slow&cold to fast&warm).
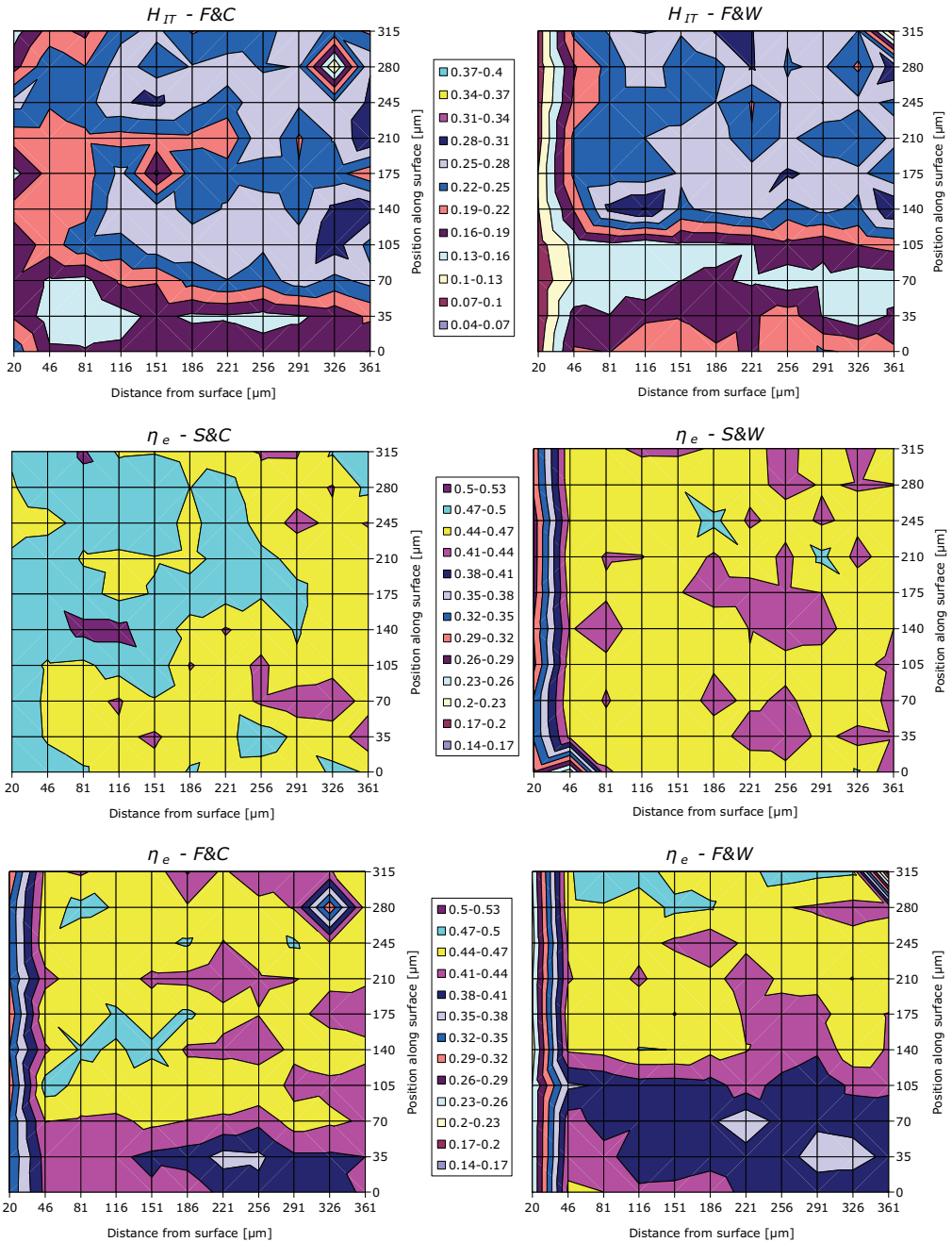
Figure 6.11: Contour plots of indentation hardness [GPa] (upper left to upper right) and elasticity index (centre left to lower right) for the different process conditions (slow&cold to fast&warm).

6.6. The Impact & Indentation Study - nanoindentation

6.6.1. Introduction

The exploratory indentation measurements showed that the NanoTest instrument was suited for probing the local mechanical properties of the moulded POM specimens. They revealed however also that measuring through-thickness gradients on ground and polished cross-sections has its clear limitations, both in terms of closeness to the surface and with respect to specimen preparation. For this study it was therefore decided to use the NanoTest instrument with the alternative approach described in chapter 6.5, i.e. to probe the mechanical properties of the outer layers of the mouldings by indenting directly on the moulded surface of the specimens[A].

6.6.2. Experimental

The measurements were made with the modified Berkovich indenter geometry. Depth-controlled indentations were made to maximum depths of 1, 5 and 10 µm, respectively, each depth in 4×4 grids. Assuming little variation in microstructure across the plate the grids were laid out so as to best avoid scratches and surface inhomogeneities resulting from the extreme process conditions used in this study. A spacing between the indentations in each grid of 50 times the indentation depth was used. Loading and unloading times were both 5 seconds and a dwell time of 30 seconds was applied at maximum depth. The data analysis method of Oliver and Pharr (chapter 6.2) was applied to the unloading data between 20 and 95% of maximum depth. Elasticity index, indentation hardness and modulus were calculated based on the ideal diamond area function for the modified Berkovich geometry as described in chapter 6.3.1. Creep data from the dwell period were analyzed and creep-rate correction of the unloading stiffness (chapter 6.3.2) was found uncalled for.

6.6.3. Results and discussion

The indentations revealed clear depth-gradients in indentation modulus – Figure 6.12 – and hardness – Figure 6.13. Both measures show a decrease with increasing maximum depth of indentation. This is contrary to the general trend found from the exploratory measurements and to the findings of Remond & Vedrines [89] and Pistor & Friedrich [90] described in chapter 6.4. This suggests that the mouldings may have a decreasing through-thickness development in mechanical properties to a certain extent, but that beyond this depth the modulus (and possibly hardness) increases again. The data of the two mentioned references would not show this decreasing behaviour, because of, in the former case, the depth resolution is too poor, and in the latter case, only one measurement depth was used for characterising the skin layer. A certain conclusion regarding this indication would however require a direct comparison of data measured on the same microstructure with e.g. both of the indentation techniques (on as-moulded surfaces and exposed cross-sections, respectively). Such comparison have not been made.

In the case of process setting VF&VC the elastic modulus at an indentation depth of 1 µm is roughly 30% higher than that at 10 µm. The former depth may be considered a measure of the skin layer only (layer 1 in chapter 4.1), the deeper depths with increasing amounts of the transition layer in the volume of interaction. The fact that also the VS&VC process condition (skin layer thickness measured to be ~23 µm in chapter 4.1) shows a decreasing through-thickness gradient going from 1 to 5 µm depth implies that the phenomenon is not related to the comet spherulites of the transition layer, but rather is related directly to the cooling rate, possibly through the relaxation of molecular orientation. This correlates also with the highest levels of indentation hardness and modulus being

---

[A] The indentation part of this study was made in collaboration with Zeynep Ilke Kalcioglu (graduate student in the Van Vliet Group at MIT), who has performed the actual measurements on the NanoTest instrument.

measured at all depths for the process condition yielding also the highest birefringence (VF&W). The difference between the process conditions constitutes at most a 20% increase. Approximating the yield stress as one third of the hardness (equation 28) results in a range from 90 MPa at 1 micron indentation depth to 64 MPa at 10 micron depth. The latter is consistent with the data sheet value from uniaxial tensile testing.
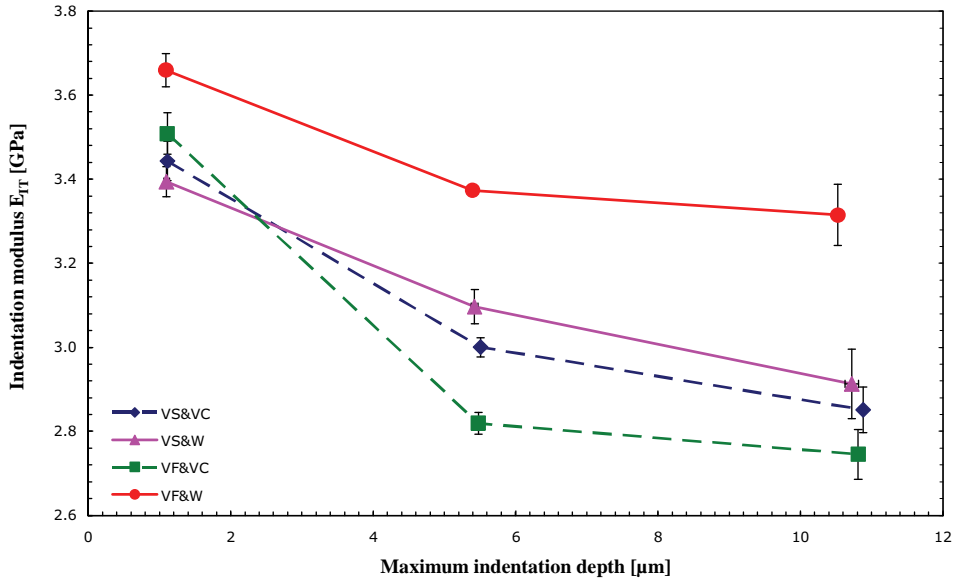
Figure 6.12: Indentation modulus as function of the maximum indentation depth.
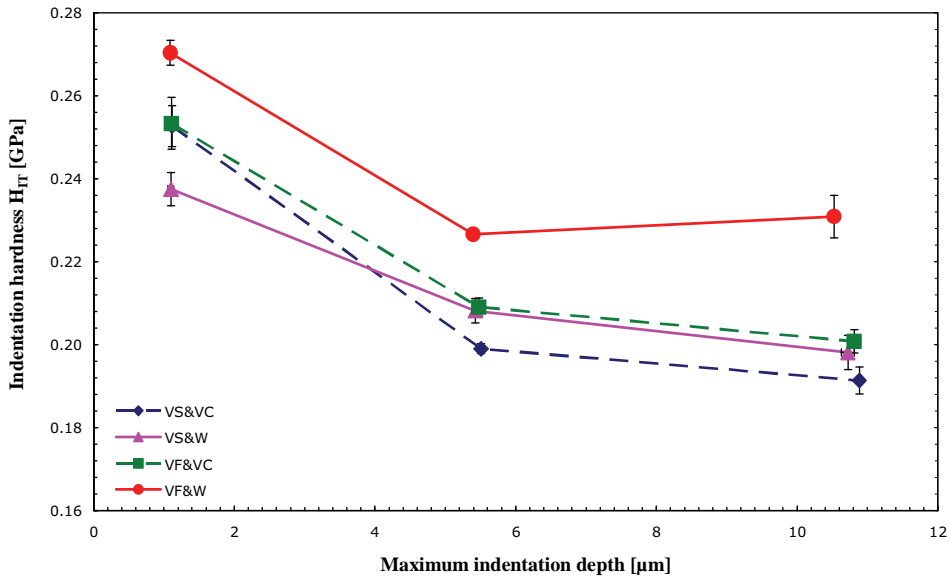
Figure 6.13: Indentation hardness as function of the maximum indentation depth.

Several researchers have described substantial differences between the mechanical properties of amorphous polymers near free surfaces and in the bulk. Tweedie *et al.* [92] ascribe the enhanced mechanical stiffness found from shallow indentations of amorphous polymers to the formation of a confined region near the probe/polymer interface. The phenomenon yields similar decreasing depth gradients as encountered in these experiments. The scaling with the relative volumetric proportion of the so-called "interphase" makes it relevant only for shallow indents, however. For indentations to contact depths well above 200 nm the mechanism is not expected to contribute significantly to the measured response, and least of all for semicrystalline polymers. This phenomenon can therefore not explain these observations.

The elasticity index data show different trends for the four process conditions. The general level is somewhat higher than what might be expected for these depths based on the results found in chapter 6.5.2. The difference is likely to result from the difference in test method, rather than from the difference in process conditions or the laser additive.
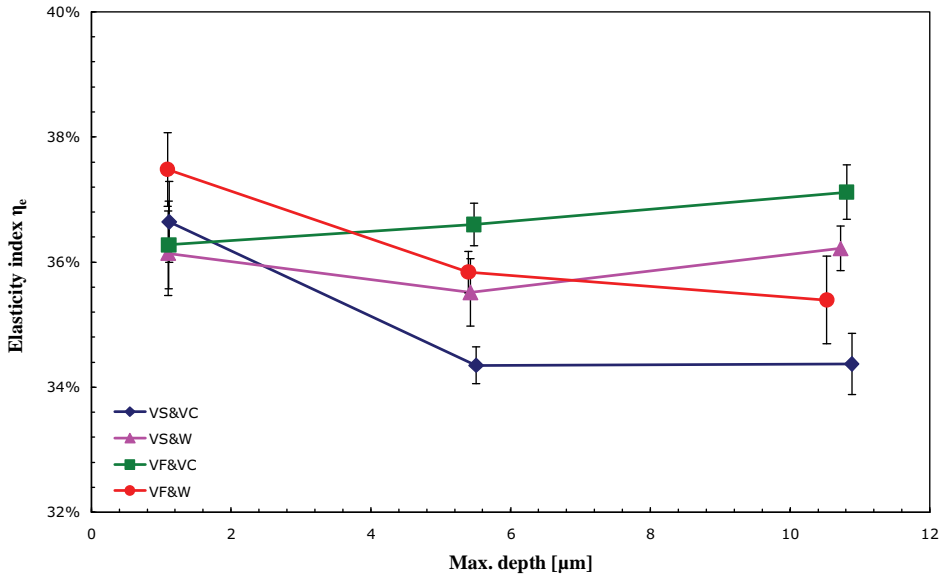
Figure 6.14: Elasticity index as function of the maximum indentation depth.

6.6.4. Main conclusions

The following main conclusions may be drawn from the presented indentation data:

- Nanoindentation of the present injection moulded POM specimens may be made directly on the moulded surfaces, without this leading to unacceptably high scatter in the data. Comparing with part 2 of the exploratory measurements, this method comes out as the preferred indentation approach to characterisation of the depth-gradients in the δ-layer.
- It may be concluded that the skin layer has higher values of both hardness and elastic modulus than the underlying transition layer.
- Both indentation hardness and modulus seem to be favoured by high lamella thickness and/or degree of orientation, as provided in the skin layer by the VF&W process condition. This suggests the smallest plastic zone for this process condition, which is in agreement with the observed lowest impact fracture toughness of these specimens.

7. SUPPLEMENTARY INVESTIGATIONS

Two extra investigations were decided on the eleventh hour of the project. They were meant simply to strengthen the conclusions already drawn on the basis of the presented studies. The results from these investigations were however not in immediate continuation of the earlier results, and consequently lead to revisions in the conclusions that had already been drawn.

7.1. Extra nanoindentations

It was decided to investigate whether or not the decreasing through-thickness gradient found in the nanoindentation investigation of the Impact & Indentation Study in chapter 6.5.2 could be observed also at increased indentation depths. Based on the results of Remond & Vedrines [89] it was thought that increases in indentation modulus and hardness might be observed if deeper indentations were made. The maximum indentation depth of 10 µm was originally chosen based on the depth capability of the NT-pendulum of the NanoTest instrument at the Chemomechanics lab at MIT, which had been used for these measurements. The NanoTest instrument at the NanoLab at MIT is equipped also with an MT-pendulum (MicroTest), allowing for higher maximum forces and displacements. This setup was used to acquire also measurements at 30 and 50 µm maximum indentation depth. The results found were not foreseen.

The new measurements were made with the same indentation conditions as used for the 1-10 µm indents, including the relative grid spacing. This meant a spacing of 1.5 mm for the 30 µm depth and a spacing of 2.5 mm for the 50 µm deep indentations. Again, assuming negligible influence of the position of the grids on the specimens (keeping a minimum distance to the edge of 5 mm), the grids were laid out so as to avoid surface defects and the grids from the earlier indentations. The indentation modulus from the new measurements showed for all process conditions remarkable periodic variations. The most extreme case was seen for the VF&W process condition at 50 µm depth, where the modulus was found to change by a factor of 2.3 over a distance of only 7.5 mm (Figure 7.1). Four indents to 1 µm depth were made in between the first two rows of the grid to make likely if the periodicity would have been present also at this depth, had a spacing of 2.5 mm been used for this depth as well. This was found not to be the case, implying that the periodic changes are not related to the surface quality or the properties of the skin layer, but rather to variations in the transition and shear layers.

Figure 7.2 and Figure 7.3 show contour plots of all the reported indentations[A] and their relative positions on the indentation specimens. The plots reveal a response highly dependent on the position on the specimen surface, clearly exorcising the earlier assumption of a homogenous response across the plate. At the 30 and 50 µm depths this is clearly not the case, although extra 30 µm grids on the VS&VC and VF&VC specimens showed areas of very little variation. No clear trend regarding the gradient across the plane of the plate is seen, and both decreasing and increasing changes are found for the two principal directions. It may be noted that the length scales of the variations encountered here are much above what might be expected if the cause of the variation was the local proximity of comet spherulites in the transition layer. From a comparison with the PLM micrographs in chapter 4.1 it is, however, evident that a certain correlation with microstructural inhomogeneities in this layer is the most likely explanation for the observed variations.

[A] Some preliminary indentations used to find suitable settings have also been made but are not shown in the figures.
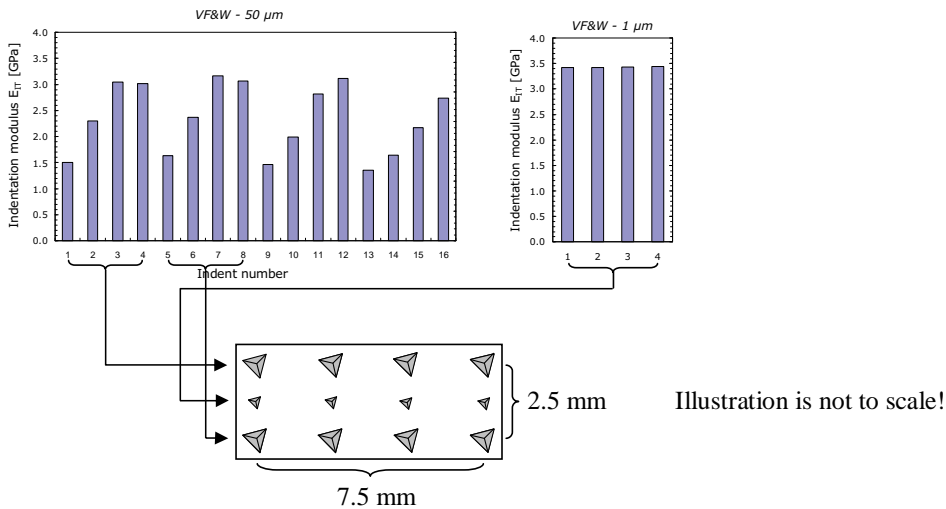
Figure 7.1: Variation in indentation modulus with indent position in grid for 50 and 1 µm maximum depths. Process condition VF&W.

The contour plots suggest that the PLM micrographs presented in chapter 4.1 may not be representative of the microstructure in general. An extra microtomed thin section was prepared from the position in the VF&W specimen, where the largest gradient in modulus had been observed (marked with a red dashed line in Figure 7.3). Micrographs from positions 'a' and 'b' are shown in Figure 7.5. Figure 7.4 shows the original 10 µm section under similar microscope settings (100X) for comparison. The new micrographs both show a higher maximum birefringence, less well-defined layer 3 (shear layer) and a pronounced layer 4 with coarser comet spherulites. The interspherulitic material in the δ-layer and in the outermost part of layer 4 is seen to be slightly more birefringent at position 'b' than at 'a', as suggested by the purple and darker brown colourations. Taking the relation between optical anisotropy and indentation properties concluded in chapter 6.6.4, position 'b' should lead to both higher indentation hardness and modulus. This is confirmed from Figure 7.3 (the extra contour plot), supporting this phenomenological conclusion. The observed difference in birefringence may be related to differences in the shear heat input to the frozen layer during the filling stage, providing a faster cooling rate in the skin layer downstream. This allows for less relaxation of flow-induced orientation and hence results in higher birefringence, hardness and modulus. Seen as such, the material in Figure 7.4 may represent a fully-developed frozen layer, where a balance between heat loss through conduction and heat input through shear heating and forced convection from the flowing melt has occurred already in the injection stage. That this condition has not been obtained in positions 'a' and 'b' at the time of switch-over can explain the variations in the mechanical response of the δ-layer along the flow path here. This argumentation can, however, not readily explain the pattern of the observed variations and other more complex mechanisms must also be in play. Moreover, the variations in the skin layer observed in the vertical direction of the micrographs suggest that fluctuations in melt flow during injection may also be part of the underlying phenomena. A comparison between e.g. Figure 7.3 lower and the

cooling line layout in Figure 2.4 does not suggest an immediate link to mould temperature inhomogeneity. Further investigations into this matter has not been made at this time.
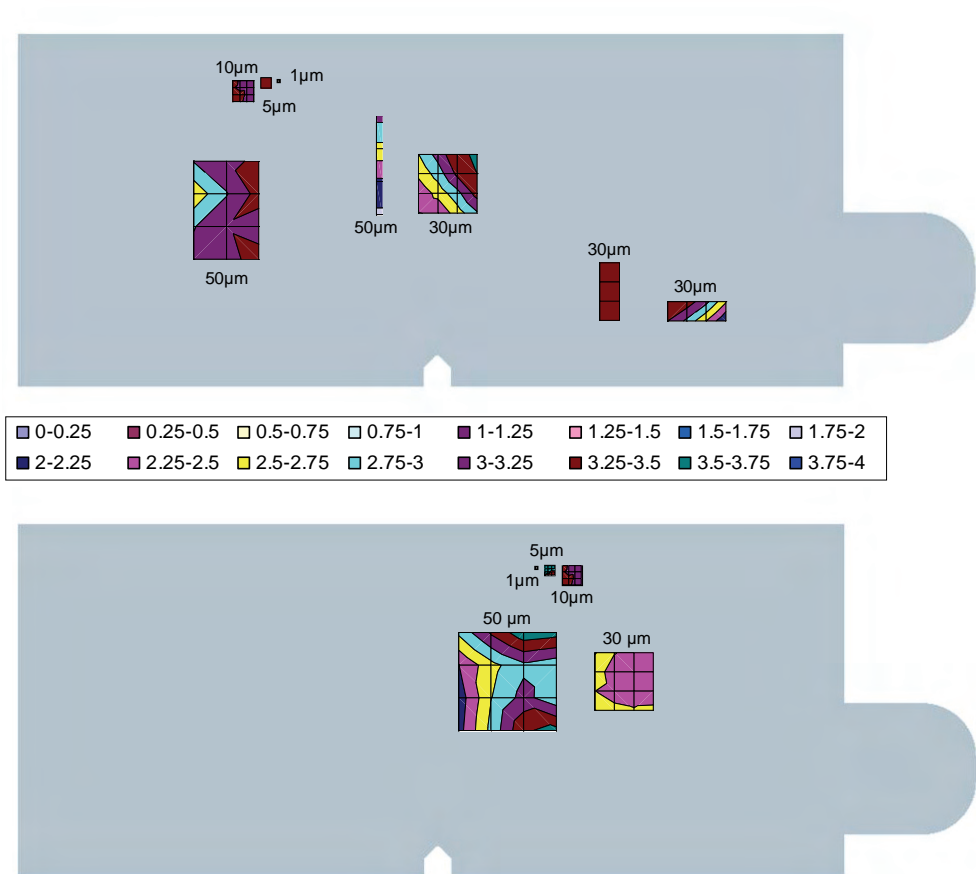
Figure 7.2: Contour plots of indentation modulus E_{IT} [GPa] placed according to the position on the indentation specimen where the measurements were made. Upper = process condition VS&VC, lower = process condition VS&W. The melt flow direction is from left to right.
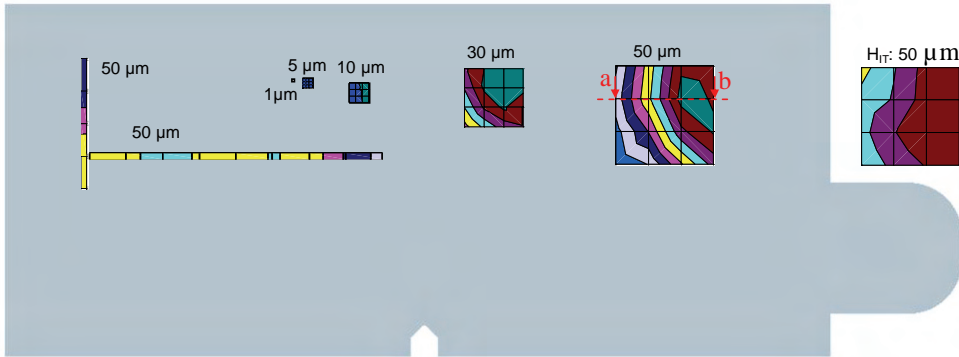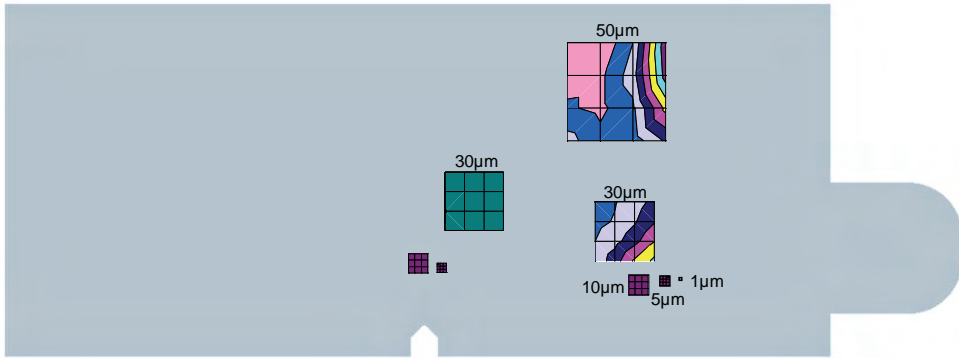
Figure 7.3: Contour plots of indentation modulus E_{IT} [GPa] placed according to the position on the indentation specimen where the measurements were made. Upper = process condition VF&VC, lower = process condition VF&W. The melt flow direction is from left to right. The dashed red line and arrows indicate the positions of the extra PLM micrographs shown in Figure 7.5. The extra contour plot to the right of the lower specimen shows the indentation hardness for the 50 µm grid with a similar graduation of the value axis.

Figure 7.4: PLM micrograph from the original 10 µm thin section of the plate from process condition VF&W (chapter 4.1), taken at same magnification as used in Figure 7.5 (100X).
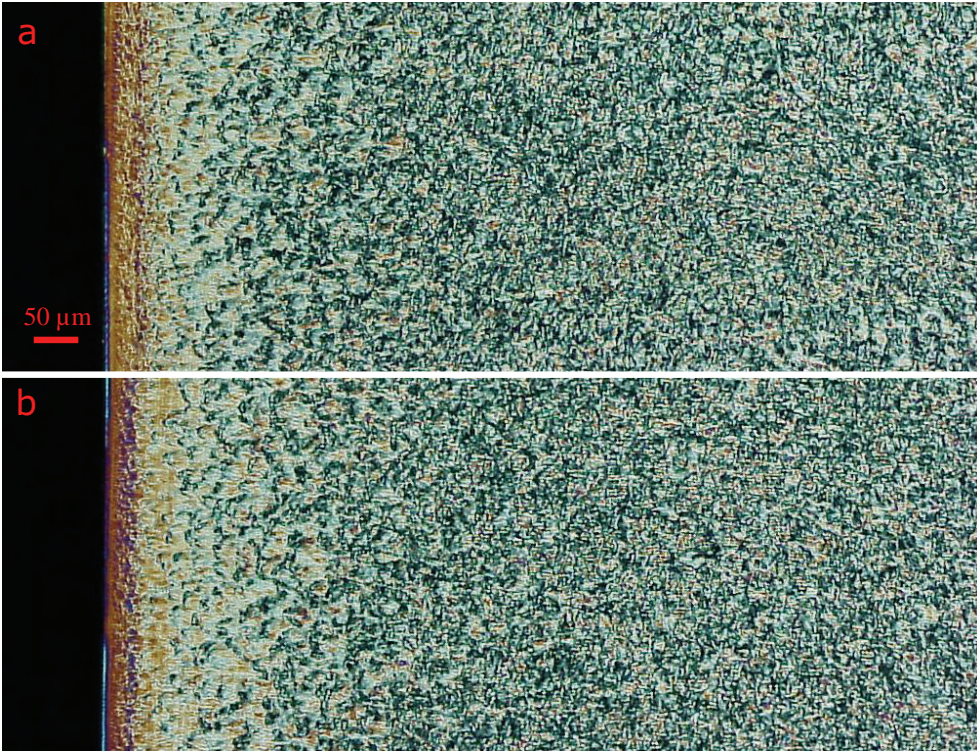
Figure 7.5: Extra PLM micrographs of 10 µm thick microtomed thin sections from process condition VF&W. Upper = upstream (position "a"), lower = downstream (position "b"). See main text for details.

7.2. Quasi-static tensile testing

Concurrently with the extra nanoindentations, it was decided to measure the quasi-static tensile yield stress of the moulded plates, as resulting from the four process conditions and two in-plane loading directions. The size requirement of the fracture mechanical testing methods are based on the yield stress as determined from unidirectional tensile testing. Although the measured impact data had already made likely that the LEFM size requirement is not fulfilled under the imposed testing conditions, whereas the J_c size requirement is, it was found of interest to investigate how the tensile yield stress varied with process and loading direction. The measured quasi-static yield stress data could furthermore be compared with the yield stress estimates from the nanoindentations, and be extrapolated to high strain rates for a more precise evaluation of the fracture mechanics size requirements.

Tensile tests were made on dumbbell-shaped specimens milled from the test blanks according to ASTM D638-02a type V (the gripping zones were shortened by 2 mm compared to the standard). Specimens were prepared from both principal directions, having the length axis either in the flow direction (FD) or in the transverse direction (TD) – see Figure 7.6. Because of scarcity in the amount of test blanks left at this time in the project[A], only one blank from each process condition could be used for each direction. The nominal dimensions of the narrow section were $3.2 \times 9.5 \times 1.5$ mm^3. The tensile tests were carried out at a displacement rate of 1 mm/min on a screw-driven Lloyd LF Plus tensile testing machine.

Figure 7.6: Dumbbell-shaped specimens for tensile testing.

Extensometer was not applied since only the stress at the yield point was sought. The engineering stress is reported as function of the nominal extension ratio of the narrow section only, i.e. the crosshead displacement divided by the length of the narrow section. An example of the stress curves is shown in Figure 7.7. Notice the abrupt drop in load at fracture of the TD-specimens compared to the FD-specimens (the relation between this feature and the loading direction was not this consistent for all conditions).

[A] The injection moulding machine that was used for making all test blanks in this project became unoperational in mid-summer 2008. It was decided that using another machine for making additional test blanks was undesired, because of the risk uncontrolled differences between the blanks. The injection moulding machine did not become available again within the time of the project, and the investigations in this study were therefore limited by the amount of blanks.
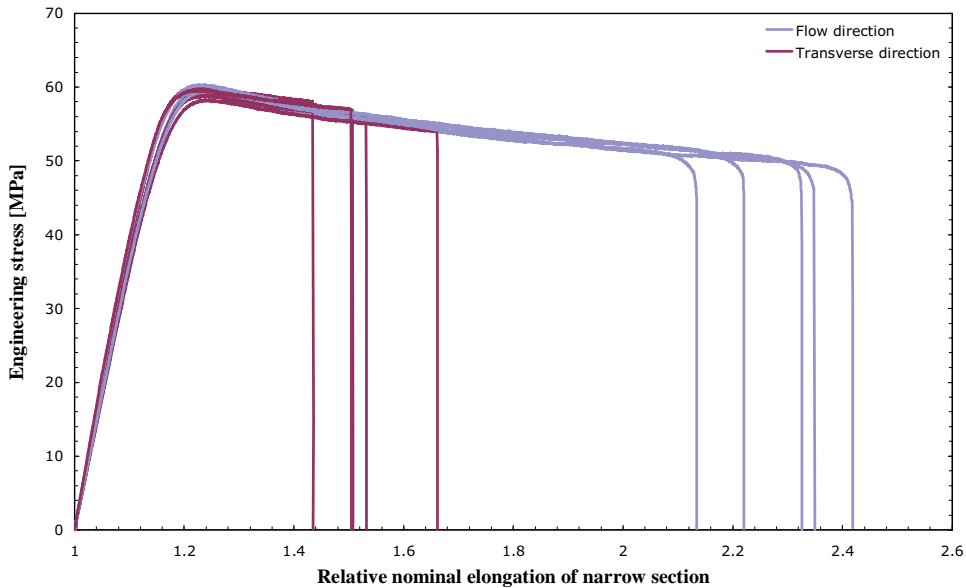
Figure 7.7: Example of tensile testing curves for the two loading directions (VF&VC data).

The measured engineering yield stress values are shown in Figure 7.8 on the primary ordinate axis. The yield stress for especially the VS&VC condition is seen to be highly anisotropic. The remarkably lower value in the flow direction is contrary to the findings of Schrauwen *et al.* [40] for injection moulded PP and HDPE, but in agreement with the POM study of Bowman [35] mentioned in chapter 5.6. The yield stress in the flow direction is seen to show a general dependence on the mould temperature, a warmer mould leading to higher yield stress. This is consistent with lamella thickening, as suggested by the SAXS measurements in chapter 4.3.2. The data sheet value of the tensile yield stress is 64 MPa for comparison.
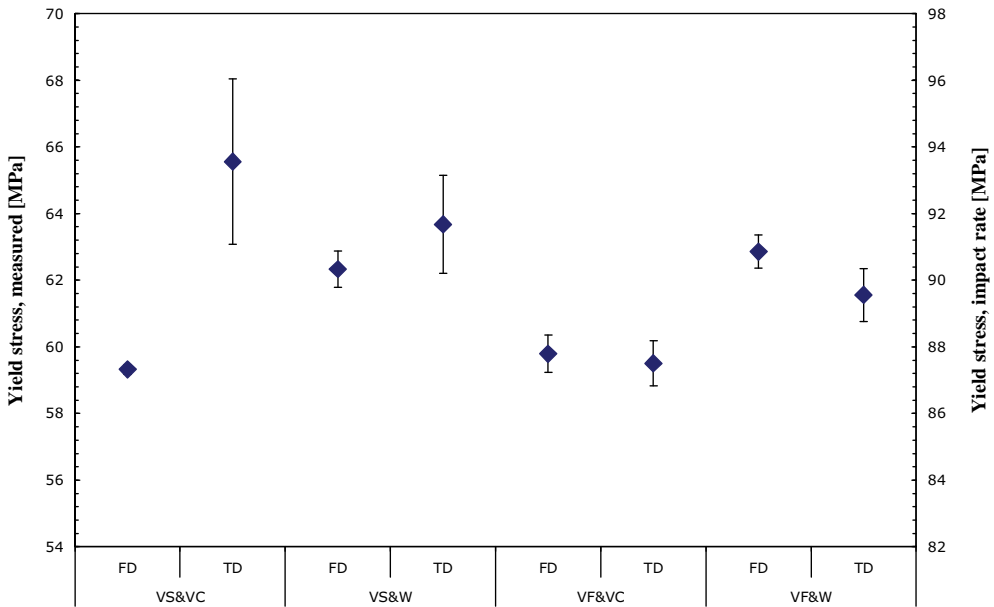
Figure 7.8: Stress at yield point from quasi-static tensile tests (primary ordinate). Regarding secondary ordinate, see below. Error bars may be smaller than the marker.

Figure 7.9 shows the strain rate dependence of the yield stress of POM as given by Plummer *et al.* [49] for a homopolymer and by Hashemi *et al.* [62] for the copolymer grade of this study. Both report similar rate dependence. Also shown are the results from measurements on this grade that NNAS have had made at Risø National Laboratories, Denmark (now Risø DTU). These measurements are clearly above the values reported by Hashemi, but extrapolating to higher strain rates the difference is less. The three points in the Risø data correspond to times-to-yield of 763, 76 and 8 s, respectively. The values on the secondary ordinate axis in Figure 7.8 results from using the strain rate dependence of Hashemi to extrapolate the yield stress values from this study to 165 s^{-1}. A lowest value of ~87 MPa is found. Taking the time-to-yield from a similar extrapolation of the Risø-data gives an approximate value at this strain rate of ~0.5 ms. This is in good agreement with the observations from the impact tests, considering the damping pad used for those tests.
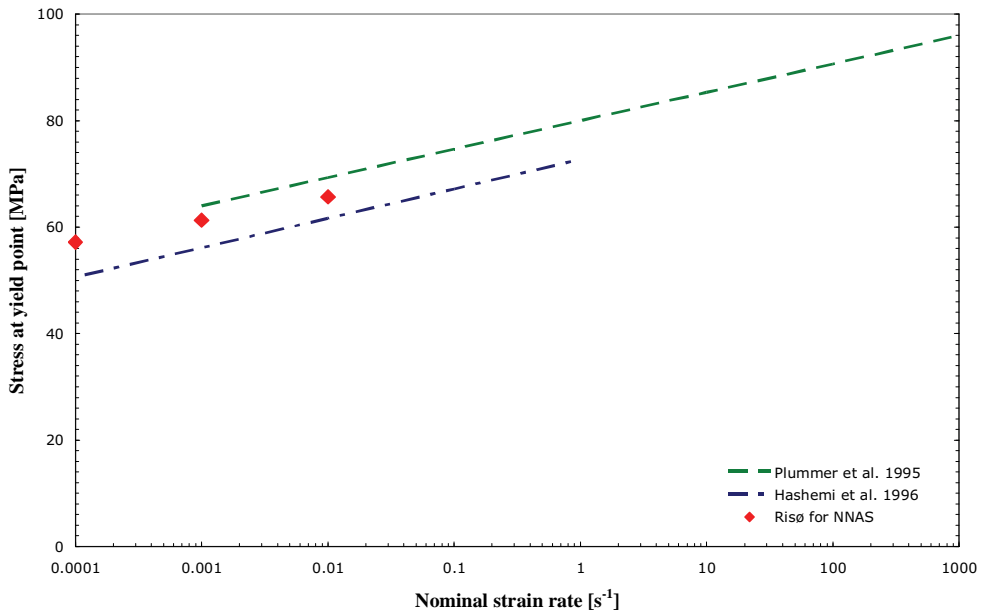
Figure 7.9: Estimation of tensile yield stress at high strain rates. Risø-data are measurements made by Risø National Laboratories, Denmark.

The argumentation described for the extra nanoindentations in chapter 7.2 suggests a dependence of the yield stress on the position of the tensile testing specimen in the blank (A-E). Figure 7.10 shows this dependence for the individual measurements on the TD-specimens. The data show a decreasing yield stress with increasing flow length. The effect is most pronounced for the process condition with thickest δ-layer, i.e. VS&VC, where it constitutes a factor of ~1.1.

Figure 7.3 shows the effect of specimen position for the FD specimens. A tendency towards higher yield stress of the inner specimens suggests a correlation with the cooling rate and/or mould filling pattern.

Taking position "E" as representing the material around the notch in the TD-specimens provides a yield stress estimate of 86-89 MPa for the impact rate loading condition. Position "A" for the FD-specimens results in a similar estimate for this direction (87-89 MPa). A comparison with the minimum yield stress requirement found in chapter 5.8.4 does not alter the conclusion regarding the prevailing stress state, i.e. the plane strain requirement of LEFM is not fulfilled at 1.5 mm thickness.

The data remains to be further analysed.
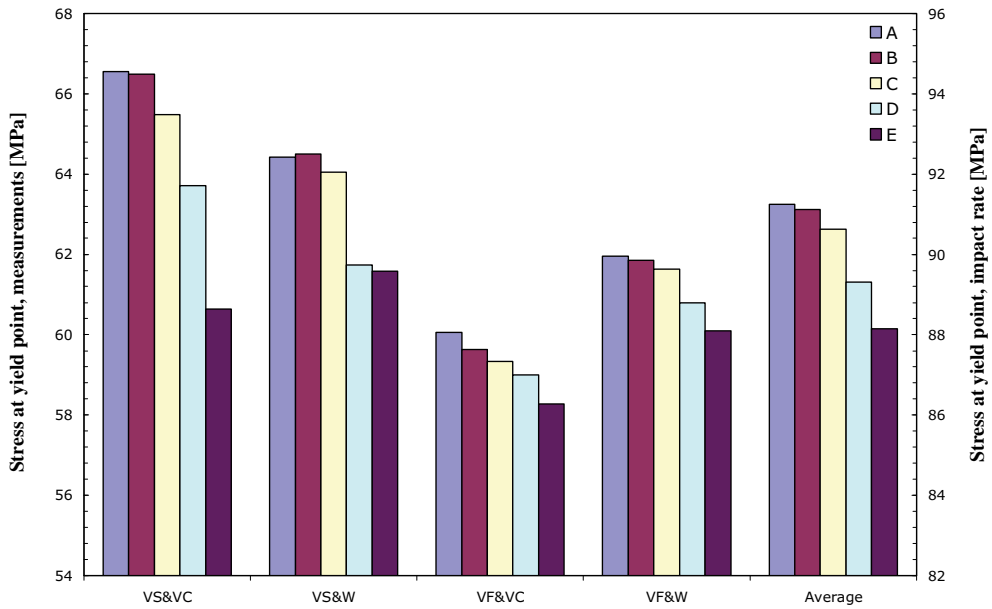
Figure 7.10: Individual yield stress measurements for the TD-specimens.
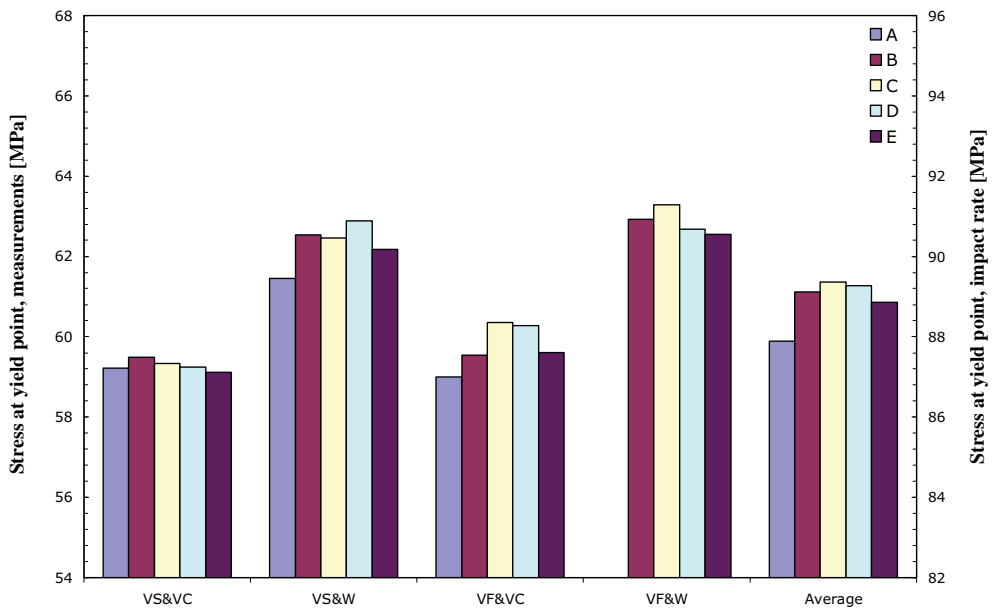
Figure 7.11: Individual yield stress measurements for the FD-specimens. Note that specimen A from the VF&W specimen was accidentally broken during the milling from the test blank.

8.   SUMMARISING CHAPTER

The theme of this project has been experimental investigations of injection moulded POM. The first task was to develop a test specimen geometry that provided for tribological and mechanical testing on material with a relevant microstructure. A modularly-build injection mould was made, which provides test plates with a predominantly unidirectional filling pattern. The construction of the mould was made so as to simulate process conditions in large-scale production and the plates are of a thickness relevant to device components (1.5 mm). Test plates were moulded in five different grades of copolymer POM, using two different mould configurations and varying mould temperature and injection melt flow.

Studies on PDMS and PTFE blended grades showed a significant reduction in coefficient of friction from the admixture of PDMS. PTFE in it self showed no effect, but in combination with PDMS it gave a further significant reduction in friction. The impact tests on these grades revealed neither deterioration in impact toughness from the additives, nor an effect of the varied processing conditions. An effect of the loading direction was found, however, straining the material in the melt flow direction leading to higher impact toughness. Fractography indicated anisotropy of the δ-layer to be the cause.

Anisotropy of this kind was found even more so in the study of pure POM under more extreme process conditions. Polarised light microscopy on microtomed thin sections revealed a thick δ-layer promoted by slow injection into a cold mould. A thin but highly birefringent δ-layer resulted from fast injection into a warm mould. WAXS showed a higher accumulated orientation from the former process condition and SAXS revealed lamella thickening in the δ-layer from a high mould temperature.

In this study the use of a moulded-in notch was found to result in pronounced anisotropy and process dependence in the impact properties. These effects were found to be much less when testing according to the standard fracture mechanical procedures, utilising a sharp pre-crack as stress raiser. The moulded-in notch is considered to be a more realistic assessment of the state of the material in real injection moulded components, and this method therefore comes out as the method of choice for investigations of this kind.

The cause of anisotropy in the impact properties was suggested by Schrauwen *et al.* [73] to be the difference in yield stress in the two loading directions. The results found in this project does not directly support this conclusion; the differences in yield stress were found to be rather subtle and, furthermore, not consistently in agreement with the underlying phenomenological explanation.

The effect on impact properties of the process conditions could be explained through two characteristics: The δ-thickness and the birefringence in the skin layer. Slow injection leads to a thick δ-layer, which results in high toughness in the flow direction. Fast injection localises the shear layer and therefore leads to higher maximum orientation and birefringence. High birefringence was found to correlate with high yield stress and therefore a smaller plastic zone, decreasing the toughness. Low mould temperature favours a thick δ-layer, increasing the toughness in the flow direction. High mould temperature reduces the δ-layer thickness and increases the yield stress, both mechanisms leading to lower toughness. Highest toughness in the flow direction was therefore found for slow injection into a cold mould. Most balanced toughness, i.e. highest toughness in the transverse direction, was found from slow injection into a warm mould.

The injection moulded plates were assumed to be homogenous across the plane of the plate. The supplementary investigations clearly showed this not to be the case, and further references found during the last stage of the project also indicates this as not being likely [40;93]. With this realisation in mind, the assessment of anisotropy from using test specimens machined from different positions along the flow path of the moulded blanks clearly adds to the uncertainty of these conclusions.

8.1. Suggested further work

Many ideas to interesting further work within the areas of injection moulding, polymer tribology, impact testing and nanoindentation have arisen during the experimental investigations of this project. Within polymer tribology it would be very interesting to pursue a confirmation or disconfirmation of the proposed hypothesis regarding the interaction between the PDMS and PTFE additives. A study of this kind could take offset in the use of PTFE in combination with different amounts of a known plasticiser for the base material. The mechanisms behind the interaction will most likely be relevant for other tribological systems as well.

Further work into the impact properties of plastics could take offset in a fracture mechanical description of notch testing as proposed by Plati & Williams [55]. Testing on specimens of various notch radii may provide information on both pre-crack and blunt notch behaviour, through an indirect assessment of the strain energy density under the relevant conditions. The suggested approach seem immediately applicable to further comparisons of fracture with and without the δ-layer present at the site of fracture initiation.

One investigation that could help to further strengthen the link between the fracture properties and the characteristics of the δ-layer is an indentation study on exposed cross-sections going through a moulded-in notch. Measurement on the actual material of the notch would ensure that the local microstructure is the one relevant for the impact properties. An investigation of this kind was actually underway during this project, but unfortunate technical circumstances lead to this work not being included in this thesis. It remains however as an obvious continuation of the indentation work of this project.

9. NOMENCLATURE AND DEFINITIONS
9.1. Symbols – Latin letters

a, a_c	crack length, critical value (crack length at initiation of brittle fracture)
A, A_c	area, projected area of contact
b	plate and specimen thickness (cross-sectional width under SENB loading)
$\mathbf{c}$	backbone direction in unit cell
C, C_c	compliance, contact creep compliance
d, d_0	periodic spacing in microstructure, characteristic size of matrix microstructure
D	characteristic size of additive
E, E'	Young's modulus, value under given conditions
E_s, E_i	Young's modulus of specimen and indenter material
E_r	reduced modulus (effective modulus of contact)
E_{IT}	indentation modulus
$f(a/w)$	geometry calibration function (given in e.g. ISO 13586)
F, F_{max}	force (load)
F_Q	defined force at crack growth initiation
G	strain energy release rate
G_c, G_{Ic}	critical strain energy release rate, value under plane strain
h, h_c, h_f, h_{max}	indentation depth, contact depth, final unloading depth, maximum depth
H, H_{IT}, HV	Meyer hardness, indentation hardness, Vickers hardness
I	intensity
J	J-integral
J_c, J_{Ic}	critical J-integral value, value under plane strain
K	stress intensity factor
K_c, K_{Ic}	critical stress intensity factor, value under plane strain
L	support span in 3-point bending
m, n	power law exponent
p	pressure
P, P_{max}	force
q	radial coordinate in reciprocal space
Q	melt flow
r	radial distance in a cylindrical coordinate system
$r1$	distance from hot runner injection point to gate of plate
R	crack growth resistance
S	stiffness
t, t_f	time, time-to-fracture cf. ISO 17281
T_g	glass transition temperature
U	difference between the work by external forces and the elastically bound strain energy; the energy related to fracture initiation
U_e, U_p	elastic and plastic work of indentation
U_{tot}	total energy at fracture initiation
$U_{tot,cor}$	total energy corrected for indentation and damper compression
w	specimen width (cross-sectional height under SENB loading)
W	plate and blank width
Y	geometry function

9.2. Symbols – Greek letters

α	fitting constant
β	parameter accounting for indenter tip non-circularity
δ	thickness of skin, transition and shear layers
ε	indenter geometry function
η	calibration factor
θ	scattering angle
λ	extension ratio
ν	Poisson's ratio
ϕ	azimuthal angle
φ	energy calibration factor (given in e.g. ISO 13586)
ρ	tip radius of the notch
σ	normal stress, value based on
σ_y	uniaxial tensile yield stress (stress at yield point)
ψ	scaling parameter

9.3. Abbreviations

AC	Alternating Current
AFM	Atomic Force Microscope
ASTM	American Society for Testing and Materials
C	Cold (level of nominal mould temperature)
CAD	Computer Aided Design
CCD	Charge-Coupled Device (photo chip in a digital camera)
CoF	Coefficient of Friction
CT	Compact Tension
CT scanner	Computer Tomography
CTOD	Crack Tip Opening Displacement
DENT	Double Edge Notched Tensile geometry
DIC	Digital Image Correlation
DOE	Design of Experiment
DSC	Differential Scanning Calorimetry
DSI	Depth-Sensing Indentation
EDX	Energy-Dispersive X-ray analysis
ESC	Environmental Stress Cracking
ESIS	European Structural Integrity Society
ECT	Energy Correction Test
F	Fast (level of injection melt flow)
FD	Flow Direction (direction parallel to melt flow)
FE	Finite Element
GPC	Gel Permeation Chromatography
HDPE	High-Density poly(ethylene)
ISO	International Standardisation Organisation
LEFM	Linear Elastic Fracture Mechanics
LOM	Light Optical Microscopy
LSR	Liquid Silicone Rubber
MB	Master Batch
MFP	Molecular Force Probe

MFR	Melt Flow Rate
MVR	Melt Volume Rate
NNAS	Novo Nordisk A/S
PA	poly(amide)
PBT	poly(butylenetherephtalate)
PC	poly(carbonate)
PDMS	poly(dimethylsiloxane)
PETE	poly(ethylenetherephthalate) homopolymer
PLM	Polarised Light Microscopy
POM	poly(oxymethylene), polyacetal
POM-C	poly()
POM neat	Ticona Hostaform C9021 with laser additive
POM pure	Ticona Hostaform C9021
PTFE	poly(tetrafluoroethylene)
S	Slow (level of injection melt flow)
SEM	Scanning Electron Microscopy
SENB	Single-Edge Notched Beam geometry
SENT	Single Edge Notched Tensile geometry
TD	Transverse Direction (transverse to melt flow)
THF	Tetrahydrofuran
VC	Very Cold (level of nominal mould temperature)
VF	Very Fast (level of injection melt flow)
VS	Very Slow (level of injection melt flow)
W	Warm (level of nominal mould temperature)
WAXS	Wide Angle X-ray Scattering

10. REFERENCES

[1] Viana, J. C., Cunha, A. M., and Billon, N., The tensile behaviour of an injection-moulded propylene-ethylene copolymer: The effect of the local thermomechanical processing conditions, Polymer International 43 (1997) 159-166.

[2] Viana, J. C., Cunha, A. M., and Billon, N., Prediction of the tensile impact behavior of injection molded samples from quasi-static data, Polymer Engineering and Science 39 (1999) 1463-1472.

[3] Viana, J. C., Cunha, A. M., and Billon, N., The effect of the skin thickness and spherulite size on the mechanical properties of injection mouldings, Journal of Materials Science 36 (2001) 4411-4418.

[4] Fischer-Cripps, A. C., Nanoindentation, Springer, 2004.

[5] Whelan, A., Injection moulding materials, Applied Science Publishers, Essex, 1982.

[6] Whelan, A. and Goff, J., Quality moulding, Applied Market Information, 1996.

[7] Viana, J. C., Cunha, A. M., and Billon, N., The thermomechanical environment and the microstructure of an injection moulded polypropylene copolymer, Polymer 43 (2002) 4185-4196.

[8] Viana, J. C., Billon, N., and Cunha, A. M., The thermomechanical environment and the mechanical properties of injection moldings, Polymer Engineering and Science 44 (2004) 1522-1533.

[9] Viana, J. C., The local thermomechanical conditions and the fracture behavior of an injection-molded poly(oxymethylene), Polymer Engineering and Science 46 (2006) 181-187.

[10] Ruby, T., Herslund, T. J., and Sivebaek, I. M. New TriboTester for Polymeric Materials. NordTrib 2006. NT2006-13-52 . 2006.
Ref Type: Conference Proceeding

[11] Delaunay, D., Le Bot, P., Fulchiron, R., Luye, J. F., and Regnier, G., Nature of contact between polymer and mold in injection molding. Part I: Influence of a non-perfect thermal contact, Polymer Engineering and Science 40 (2000) 1682-1691.

[12] Delaunay, D., Le Bot, P., Fulchiron, R., Luye, J. F., and Regnier, G., Nature of contact between polymer and mold in injection molding. Part II: Influence of mold deflection on pressure history and shrinkage, Polymer Engineering and Science 40 (2000) 1692-1700.

[13] Apichartpattanasiri, S., Hay, J. N., and Kukureka, S. N., A study of the tribological behaviour of polyamide 66 with varying injection-moulding parameters, Wear 250 (2001) 1557-1566.

[14] Benabdallah, H., Friction and wear of blended polyoxymethylene sliding against coated steel plates, Wear 254 (2003) 1239-1246.

[15]   Benabdallah, H. S. and Wei, J. J., Effects of lubricants on the friction and wear properties of PTFE and POM, Journal of Tribology-Transactions of the Asme 127 (2005) 766-775.

[16]   Benabdallah, S. H., The Running-in and Steady-State Coefficient of Friction of Some Engineering Thermoplastics, Polymer Engineering and Science 33 (1993) 70-74.

[17]   Benabdallah, S. M. H. and Yelle, H., Static and Quasi-Dynamic Coefficient of Friction of 3 Engineering Thermoplastics - Uhmwpe, Pa-66, Pom, Journal of Materials Science 26 (1991) 2445-2450.

[18]   BONGIOVA.G and Clerico, M., Understanding Plastic Wear - Studies of Friction Between Acetal and Polypropylene Resins and Steel Provide Insight Into Effects of Applied Load Temperature and Exposure on Wear of Plastic Materials, Modern Plastics 44 (1967) 126-&.

[19]   Briscoe, B. J. and Tabor, D., Friction and Wear of Polymers - Role of Mechanical-Properties, British Polymer Journal 10 (1978) 74-78.

[20]   Franklin, S. E. and de Kraker, A., Investigation of counterface surface topography effects on the wear and transfer behaviour of a POM-20% PTFE composite, Wear 255 (2003) 766-773.

[21]   Jeng, M. C., Fung, C. P., and Li, T. C., The study on the tribological properties of fiber-reinforced PBT composites for various injection molding process parameters, Wear 252 (2002) 934-945.

[22]   Long, C. G. and Hua, M. Y., Study on POM composites modified by Ekonol and lubricant, Journal of Thermoplastic Composite Materials 18 (2005) 381-391.

[23]   Mergler, Y. J., Schaake, R. P., and in't Veld, A. J. H., Material transfer of POM in sliding contact, Wear 256 (2004) 294-301.

[24]   Odiowei, S. and Schipper, D. J., Tribological Behavior of Unfilled and Composite Polyoxymethylene, Wear 148 (1991) 363-376.

[25]   Pooley, C. M. and Tabor, D., Friction and Molecular Structure - Behavior of Some Thermoplastics, Proceedings of the Royal Society of London Series A-Mathematical and Physical Sciences 329 (1972) 251-&.

[26]   Samyn, P. and De Baets, P., Friction and wear of acetal: A matter of scale, Wear 259 (2005) 697-702.

[27]   Wang, J., Hu, X. G., Tian, M., and Stengler, R., Study on mechanical and tribological property of nanometer ZrO2-filled polyoxymethylene composites, Polymer-Plastics Technology and Engineering 46 (2007) 469-473.

[28]   Jain, V. K. and Bahadur, S., Material Transfer in Polymer-Polymer Sliding, Wear 46 (1978) 177-188.

[29]   Erhard, G., Sliding Friction Behavior of Polymer Polymer Material Combinations, Wear 84 (1983) 167-181.

[30] Czichos, H., Influence of Adhesive and Abrasive Mechanisms on the Tribological Behavior of Thermoplastic Polymers, Wear 88 (1983) 27-43.

[31] Yamada, Y., Investigation of transfer phenomenon by X-ray photoelectron spectroscopy and tribological properties of polymers sliding against polymers, Wear 210 (1997) 59-66.

[32] Hu, X. G., Tribological behaviour of modified polyacetal against MC nylon without lubrication, Tribology Letters 5 (1998) 313-317.

[33] Yamaguchi, Y., Tribology of Plastic Materials – Their Characteristics and Applications to Sliding Components, Elsevier, 1990.

[34] Böhme, E., Failure Analysis using Microscopic Techniques, DuPont Engineering Polymers, 2001.

[35] Bowman, J., The Structure and Mechanical-Properties of An Injection-Molded Acetal Co-Polymer, Journal of Materials Science 16 (1981) 1151-1166.

[36] Wright, D. G. M., Dunk, R., Bouvart, D., and Autran, M., The Effect of Crystallinity on the Properties of Injection Molded Polypropylene and Polyacetal, Polymer 29 (1988) 793-796.

[37] KargerKocsis, J., Varga, J., and Ehrenstein, G. W., Comparison of the fracture and failure behavior of injection-molded alpha- and beta-polypropylene in high-speed three-point bending tests, Journal of Applied Polymer Science 64 (1997) 2057-2066.

[38] Cunha, A. M. and Pouzada, A. S.,The Impact Behaviour of Polypropylene and the Injection-Moulding Conditions in J.G.Williams, A.Pavan (Eds.), Impact and Dynamic Fracture of Polymers and Composites, Mechanical Engineering Publications, London, 1995, pp. 315-325.

[39] Brostow, W., Performance of Plastics, Hanser, 2001.

[40] Schrauwen, B. A. G., Von Breemen, L. C. A., Spoelstra, A. B., Govaert, L. E., Peters, G. W. M., and Meijer, H. E. H., Structure, deformation, and failure of flow-oriented semicrystalline polymers, Macromolecules 37 (2004) 8618-8633.

[41] Delly, J. G. The Michel-Lévy Interference Color Chart. 2003.
Ref Type: Internet Communication

[42] Lam, K. L., bu Bakar, A., Ishak, Z. A. M., and Karger-Kocsis, J., Amorphous copolyester/polyoxymethylene blends: Thermal, mechanical and morphological properties, Kautschuk Gummi Kunststoffe 57 (2004) 570-+.

[43] Plummer, C. J. G. and Kausch, H. H., A Dsc Investigation of the Crystallization Kinetics of Polyoxymethylene, Polymer Bulletin 32 (1994) 117-124.

[44] Kawaguchi, K., Mechanical properties and transparency of injection-molded polyacetal with branched and linear structure: Influence of crystalline morphology, Journal of Applied Polymer Science 100 (2006) 3382-3392.

[45] Somani, R. H., Yang, L., Hsiao, B. S., Sun, T., Pogodina, N. V., and Lustiger, A., Shear-induced molecular orientation and crystallization in isotactic polypropylene: Effects of the deformation rate and strain, Macromolecules 38 (2005) 1244-1255.

[46] Sakurai, S., Aida, S., Okamoto, S., Ono, T., Imaizumi, K., and Nomura, S., Preferential orientation of lamellar microdomains induced by uniaxial stretching of cross-linked polystyrene-block-polybutadiene-block-polystyrene triblock copolymer, Macromolecules 34 (2001) 3672-3678.

[47] Zhu, P. W. and Edward, G., Morphological distribution of injection-moulded isotactic polypropylene: a study of synchrotron small angle X-ray scattering, Polymer 45 (2004) 2603-2613.

[48] Hashemi, S. and Williams, J. G., Fracture from Inherent Flaws in Polymers, Journal of Materials Science 20 (1985) 4202-4208.

[49] Plummer, C. J. G., Beguelin, P., and Kausch, H. H., The Temperature and Strain-Rate Dependence of Mechanical-Properties in Polyoxymethylene, Polymer Engineering and Science 35 (1995) 1300-1312.

[50] Brostow, W. and Corneliussen, R. D., Failure of Plastics, Hanser Publishers, 1986.

[51] Hashemi, S., Gilbride, M. T., and Hodgkinson, J., Mechanical property relationships in glass-filled polyoxymethylene, Journal of Materials Science 31 (1996) 5017-5025.

[52] Moore, D. R., Pavan, A., and Williams, J. G., Fracture Mechanics Testing Methods for Polymers, Adhesives and Composites, Elsevier Science Ltd., 2001.

[53] Williams, J. G., Fracture Mechanics of Polymers, Polymer Engineering and Science 17 (1977) 144-149.

[54] Williams, J. G., Hale, G. E., and Ramsteiner, F.,Elastic-Plastic Fracture Mechanics in D.R.Moore, A.Pavan, J.G.Williams (Eds.), Fracture Mechanics Testing Methods for Polymers Adhesives and Composites, Elsevier, 2001, pp. 119-195.

[55] Plati, E. and Williams, J. G., Determination of Fracture Parameters for Polymers in Impact, Polymer Engineering and Science 15 (1975) 470-477.

[56] Rice, J. R., Paris, P. C., and Merkle, J. G.,Some further results of J-integral analysis and estimates ASTM Special Technical Publication no. 536, ASTM, Philadelphia, 1973, pp. 231-245.

[57] Pukanszky, B., Maurer, F. H. J., and Boode, J. W., Impact testing of polypropylene blends and composites, Polymer Engineering and Science 35 (1995) 1962-1971.

[58] Han, Y. C., Lach, R., and Grellmann, W., The Charpy impact fracture behaviour in ABS materials, Angewandte Makromolekulare Chemie 270 (1999) 13-21.

[59] Fasce, L. A., Pettarin, V., Seltzer, R., and Frontini, P. M., Evaluation of impact fracture toughness of polymeric materials by means of the J-integral approach, Polymer Engineering and Science 43 (2003) 1081-1095.

[60] Sumpter, J. D. G. and Turner, C. E., Applicability of J to Elastic-Plastic Materials, International Journal of Fracture 9 (1973) 320-321.

[61] Andreassen, E. Impact fracture mechanics testing of plastic materials for injection moulding. Laursen, J. L. 2008.
Ref Type: Personal Communication

[62] Hashemi, S., Din, K. J., and Low, P., Fracture behavior of glass bead-filled poly(oxymethylene) injection moldings, Polymer Engineering and Science 36 (1996) 1807-1820.

[63] Hashemi, S., Elmes, P., and Sandford, S., Hybrid effects on mechanical properties of polyoxymethylene, Polymer Engineering and Science 37 (1997) 45-58.

[64] Chang, F. C. and Yang, M. Y., Mechanical Fracture-Behavior of Polyacetal and Thermoplastic Polyurethane Elastomer Toughened Polyacetal, Polymer Engineering and Science 30 (1990) 543-552.

[65] Kumar, G., Neelakantan, N. R., and Subramanian, N., Polyacetal and Thermoplastic Polyurethane Elastomer Toughened Polyacetal - Crystallinity and Fracture-Mechanics, Journal of Materials Science 30 (1995) 1480-1486.

[66] Lam, K. L., Bakar, A. A., and Ishak, Z. A. M., Effects of compatibilizer and testing speed on the mechanical and morphology behaviors of co-continuous amorphous copolyester-polyoxymethylene blends, Polymer Engineering and Science 45 (2005) 710-719.

[67] Lazzeri, A., Marchetti, A., and Levita, G., Fatigue and fracture in polyacetal resins, Fatigue & Fracture of Engineering Materials & Structures 20 (1997) 1207-1216.

[68] Mehrabzadeh, M. and Rezaie, D., Impact modification of polyacetal by thermoplastic elastomer polyurethane, Journal of Applied Polymer Science 84 (2002) 2573-2582.

[69] Uthaman, R. N., Pandurangan, A., and Majeed, S. S. M. A., Mechanical, thermal, and morphological characteristics of compatibilized and dynamically vulcanized polyoxymethylene/ethylene propylene diene terpolymer blends, Polymer Engineering and Science 47 (2007) 934-942.

[70] Uthaman, R. N., Pandurangan, A., and Majeed, S. S. M. A., Blends of polyacetal and ethylene-octene elastomer: Mechanical, dynamic mechanical and morphological properties, Journal of Polymer Research 14 (2007) 441-447.

[71] Kawaguchi, K. and Tajima, Y., Interfacial reaction and its influence on phase morphology and impact properties of modified-polyacetal/thermoplastic polyurethane blends, Journal of Applied Polymer Science 100 (2006) 4375-4382.

[72] Karger-Kocsis, J., Moos, E., Mudra, I., and Varga, J., Effects of molecular weight on the perforation impact behavior of injection-molded plaques of alpha- and beta-phase isotactic polypropylenes, Journal of Macromolecular Science-Physics B38 (1999) 647-662.

[73] Schrauwen, B. A. G., Govaert, L. E., Peters, G. W. M., and Meijer, H. E. H., The influence of flow-induced crystallization on the impact toughness of high-density polyethylene, Macromolecular Symposia 185 (2002) 89-102.

[74] Chiang, W. Y. and Lo, M. S., Cooling and Annealing Properties of Copolymer-Type Polyacetals and Its Crystallization Behavior, Journal of Applied Polymer Science 34 (1987) 1997-2023.

[75] Karger-Kocsis, J., Toward understanding the morphology-related crack initiation and propagation behavior in polypropylene systems as assessed by the essential work of fracture approach, Journal of Macromolecular Science-Physics B38 (1999) 635-646.

[76] Akay, M. and Barkley, D., Pitfalls in the Evaluation of Impact Fracture of Polymer-Based Materials, Polymer Testing 7 (1987) 391-404.

[77] Ezrin, M., Plastics Failure Guide, Hanser Publishers, 1996.

[78] Moalli, J., Plastics Failure - Analysis and Prevention, Plastic Design Library, 2001.

[79] Pavan, A.,Determination of Fracture Toughness (GIc and KIc) at Moderately High Loading Rates in D.R.Moore, A.Pavan, J.G.Williams (Eds.), Fracture Mechanics Testing Methods for Polymers Adhesives and Composites, Elsevier, 2001, pp. 27-58.

[80] Bezeredi, A., Voros, G., and Pukanszky, B., Mechanical damping in instrumented impact testing, Journal of Materials Science 32 (1997) 6601-6608.

[81] VanLandingham, M. R., Villarrubia, J. S., Guthrie, W. F., and Meyers, G. F., Nanoindentation of polymers: An overview, Macromolecular Symposia 167 (2001) 15-43.

[82] Mencik, J., Determination of mechanical properties by instrumented indentation, Meccanica 42 (2007) 19-29.

[83] Oliver, W. C. and Pharr, G. M., An Improved Technique for Determining Hardness and Elastic-Modulus Using Load and Displacement Sensing Indentation Experiments, Journal of Materials Research 7 (1992) 1564-1583.

[84] Feng, G. and Ngan, A. H. W., Effects of creep and thermal drift on modulus measurement using depth-sensing indentation, Journal of Materials Research 17 (2002) 660-668.

[85] Tweedie, C. A. and Van Vliet, K. J., Contact creep compliance of viscoelastic materials via nanoindentation, Journal of Materials Research 21 (2006) 1576-1589.

[86] Fischer-Cripps, A. C., A simple phenomenological approach to nanoindentation creep, Materials Science and Engineering A-Structural Materials Properties Microstructure and Processing 385 (2004) 74-82.

[87] Lach, R., Gyurova, L. A., and Grellmann, W., Application of indentation fracture mechanics approach for determination of fracture toughness of brittle polymer systems, Polymer Testing 26 (2007) 51-59.

[88] Laugier, M. T., New Formula for Indentation Toughness in Ceramics, Journal of Materials Science Letters 6 (1987) 355-356.

[89] Remond, Y. and Vedrines, M., Measurement of local elastic properties of injection moulded polymer structures by analysis of flexural resonant frequencies. Applications in POM, PA66, filled PA 66, Polymer Testing 23 (2004) 267-274.

[90] Pistor, C. and Friedrich, K., Scratch and indentation tests on polyoxymethylene (POM), Journal of Applied Polymer Science 66 (1997) 1985-1996.

[91] Automation Creations, Inc. MatWab - Ticona Hostaform C 9021 Acetal Copolymer. 2008. 12-11-0080.
Ref Type: Internet Communication

[92] Tweedie, C. A., Constantinides, G., Lehman, K. E., Brill, D. J., Blackman, G. S., and Van Vliet, K. J., Enhanced stiffness of amorphous polymer surfaces under confinement of localized contact loads, Advanced Materials 19 (2007) 2540-+.

[93] Gotham, K. V. and Scrutton, I. N., Effect of Molecular-Orientation on Fracture Toughness of Thermoplastics, Polymer 19 (1978) 341-347.

11. APPENDICES

11.1. Test blank and injection mould design

A list of potential areas of application of a test plate within material and process characterisation in Device R&D was made prior to the design of the test plate and mould:

    I. Yield behaviour
   II. Impact performance
  III. Notch sensitivity
  IV. Fracture mechanical characterisation
   V. ESC resistance
  VI. Distribution of additives
 VII. Tribological properties
VIII. Shrinkage and warpage
  IX. Tendency of a grade to form mould deposits
   X. Weld line strength, evaluated by II or IV
  XI. Effect of vacuum evacuation of the mould cavity on X.
 XII. Effect of underflow during weld line formation on X.
XIII. Characterisation of anisotropy due to molecular orientation, evaluated by II - V, VII and VIII.
XIV. Influence of surface finish (roughness, topography, coatings) on V, VII and IX.
 XV. Influence of processing conditions on I - XIV.

It was furthermore of interest for the injection mould to provide process data for benchmarking of different injection moulding simulations tools.

The procured solution provides for test blanks of the seven configurations given below:

Configuration	Description of test plate/cavity
1	$60 \times 60 \times 1.5$ mm^3 plate with polished surfaces
2	$60 \times 60 \times 1.5$ mm^3 plate with one side polished and one side spark eroded.
3	$60 \times 60 \times 1.5$ mm^3 plate with polished surfaces and moulded-in notches on two side edges
4	$60 \times 60 \times 1.5$ mm^3 plate with polished surfaces and a central weld line
5	$60 \times 60 \times 6$ mm^3 plate with polished surfaces
6	$60 \times 60 \times 1.5$ mm^3 plate with polished surfaces, one side with an etched grid
7	$60 \times 6 \times 1.5$ mm^3 strip with polished surfaces

The mould is modularly build as a mould base with interchangeable inserts; three inserts in each mould half. An overview image from the CAD model is shown below. The hot runner system (Husky Injection Moulding Systems, Canada) is equipped with 1.5 mm needle-valve nozzles with pneumatic actuation. This is the standard solution used in large-scale production moulds at NNAS and thus constitutes a realistic runner system for the test specimen mould. The hot runner solution is implemented as two separate hot halves: a one drop edition and a two drop edition. The latter is used for configuration 4, where a central weld line is created by gating from two opposing side edges of the plate. Configuration 2 features two surface roughnesses, one mould side insert being polished with diamond paste 7 μm, the other spark eroded to Charmille 30. This configuration was used in some preliminary investigations of the influence of surface roughness on frictional

properties, but have not been used in the studies reported in this thesis. All other configurations have polished cavities of the same grade, i.e. polished with diamond paste 7 μm. R_a and R_z values for the polished surfaces were measured to be 9 and 90 nm, respectively (ISO 4287). Configuration 3 contains a moulded-in notch in both the end edge and one of the side edges. These are used as stress concentrators in some of the impact tests in the Impact & Indentation Study. Configuration 5 yields 6 mm thick plates and was intended for fracture mechanical characterisations of grades that require high thickness to be characterised under plane strain conditions (described in chapter 5.4). Configuration 6 was made for use in investigations of post-moulding shrinkage and warpage, based on optical measurements of the reproduced grid etched into the insert. These studies are not a part of this project. Configuration 7 yields a thin strip of 1.5×6 mm cross-section, rather than a plate blank. The configuration was made to provide impact testing specimens moulded with very high shear rates. The strip geometry of this configuration, however, only allows for evaluation of mechanical properties of the material loaded in the flow direction, and thus not of the extent of anisotropy.

Only configurations 1 and 3 have been used for the studies reported in this thesis.

The mould has been prepared for vacuum evacuation of the cavity. This feature is of great relevance in weld line studies, where the technique may be used to obtain stronger butt welds (weld lines with head-on collision of melt fronts) by reduction of the stress concentration of the notch caused by the weld line. In the two drop hot half the valves may be controlled separately to facilitate e.g. experiments with underflow during weld line formation, another technique used for weld line strength optimisation. Figure 11.1 shows a short-shot from the qualification of the weld-line configuration (4).
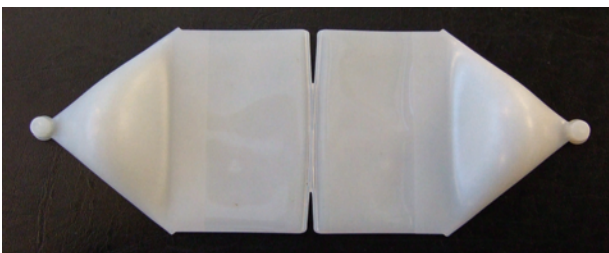
Figure 11.1: Short shot of PA moulding in configuration 4, showing that the desired flow front during weld line formation is obtained.

Inserts in the test blank mould

Fixed mould half

A2A1/A2A2

V

A1A1/A1A2/A1B1

I

III

IV

B1A1

II

A1B1

XIV

XI

XIII

XII

VIII

B1A1

VII

IX/X

VI

A2A1/A2A2

Moving mould half

Explode State:Default Explode
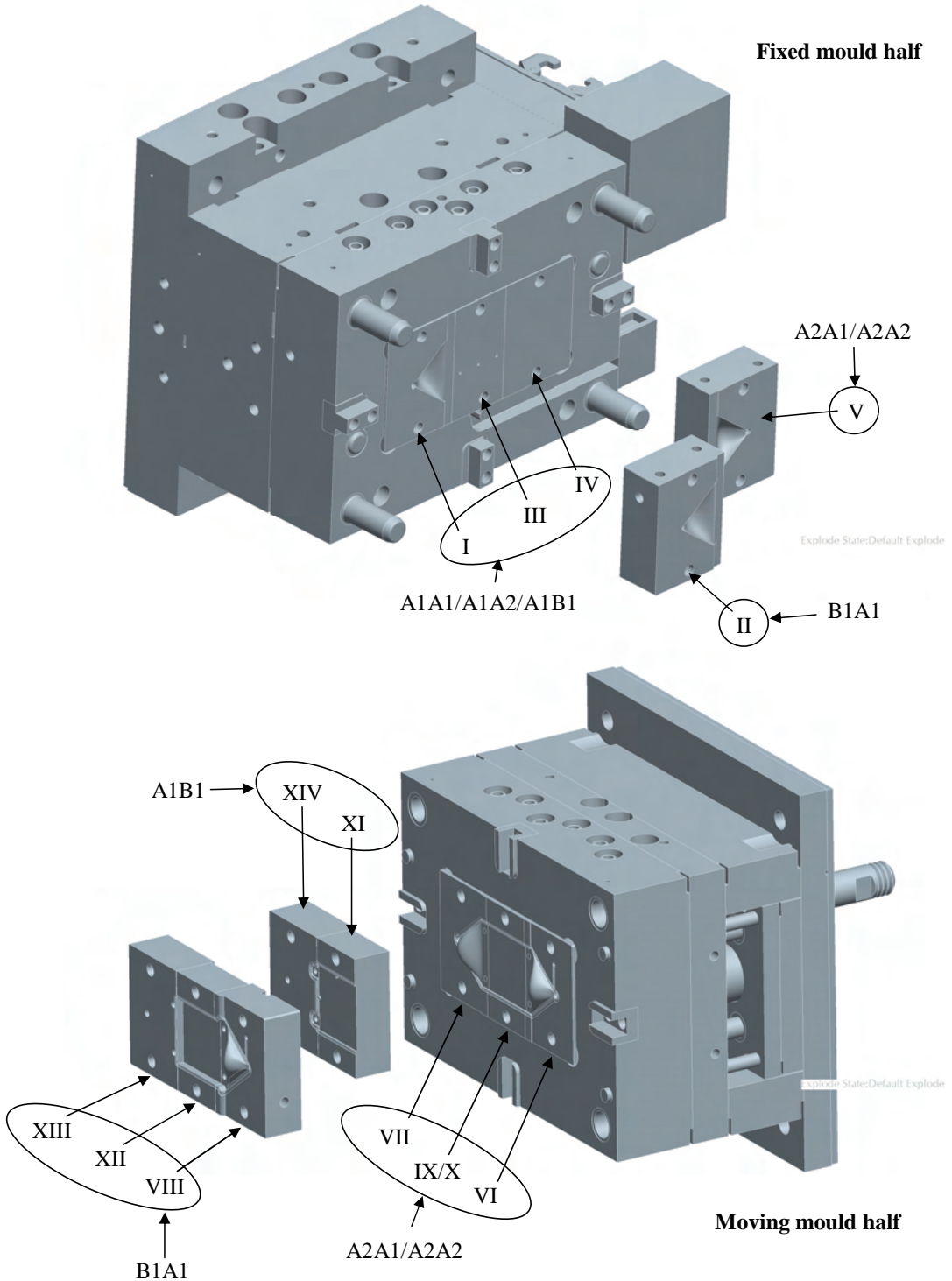
The numbers and names refer to the designations used for this mould internally in NNAS

11.2. Impact testing setup

At the time when the project was commenced Device R&D at NNAS was in possession of two spindle-driven and one servo-hydraulic tensile testing machine. The latter, which was found potentially suited for applying impact rates of loading, has a maximum sampling rate of 5 kHz. With the requirement in ISO17281 of a minimum of 200 data points up to fracture initiation, and an estimated minimum time-to-fracture of 0.5 ms [79], the sampling rate requirement was estimated to be >400 kHz and the equipment in possession was therefore deemed insufficient. Within the first half year of the project a spare falling weight impact tester became available from another part of the organisation (earlier used for QC on cartridge glass). With the following data this apparatus was found suited for the impact tests being planned:

Vendor: Instron
Model: Dynatup Minitower
Type: Falling weight
Instrumentation: 2.4 kN piezoelectric force transducer (lowest force range up to 140 N)
                      15.5 kN strain gauge force transducer (not applicable to high rate impact)
                      450 N piezoelectric force transducer (bought for Impact & Indentation Study)
Max. impact velocity: 3 m/s
Impact energy range: 0.7-18.1 J
Data sampling: 13 bit, up to 4.1 MHz
Sampling trigger: Adjustable optoswitch or force
Software: Instron Impulse ver. 2.2.1

Figure 11.2: Falling weight impact tester at NNAS. Close-up shown in Figure 11.3.
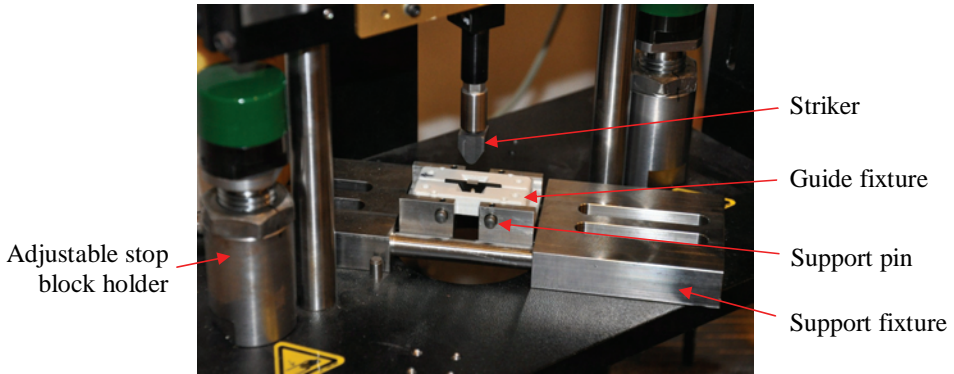
Figure 11.3: Close-up of impact tester with SENB specimen positioned in guide fixture.

Support rigs and fixtures for SENB impact testing was procured for the apparatus. These accessories include the following:

- Adjustable stop block holder
- Adjustable support fixture with replaceable support pins (Ø6 mm)
- Wedge striker for piezo transducer (R3 mm) with ScrewLock HeliCoil mount
- Specimen placer for 1.5 mm thick specimens, standing or lying flat
- Guide fixture for 1.5 mm thick SENB specimens
- Energy Correction Test support fixture for specimen thickness 4-6 mm
- Energy Correction Test support fixture for specimen thickness 1.5 mm
- Razor blade holder used for making pre-cracks
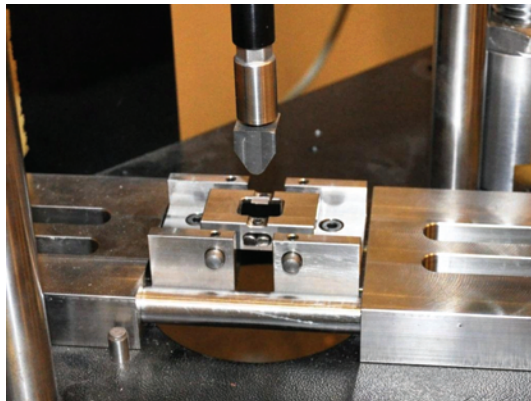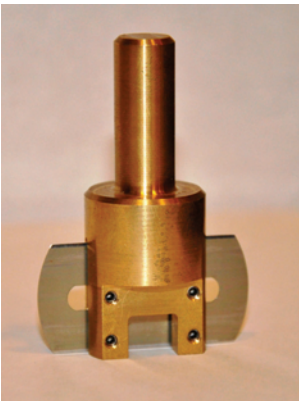
Figure 11.4: Razor blade holder (left) and ECT support fixture (right).

A machine drawing for the SENB specimens including GPS tolerances (Geometric Product Specification) was made for the external machining of specimens for the Additives & Impact Study and is shown below.

A   B

28±0.5 Ⓔ

14±0.1 Ⓔ

6±0.1 Ⓔ

▽ C

▱ 0.01

∥ 0.05 C

Detail D

1.5 +0.05 -0.10 Ⓔ

A

B

⊥ 0.1 B

A

▽ C

⊥ 0.1 B

∥ 0.05 C

2±0.1

90°

90°

90°

R0.25

3.9/3/2.1

∥ 0.05 C

B

A-A
10:1

25

10:1
Detail D
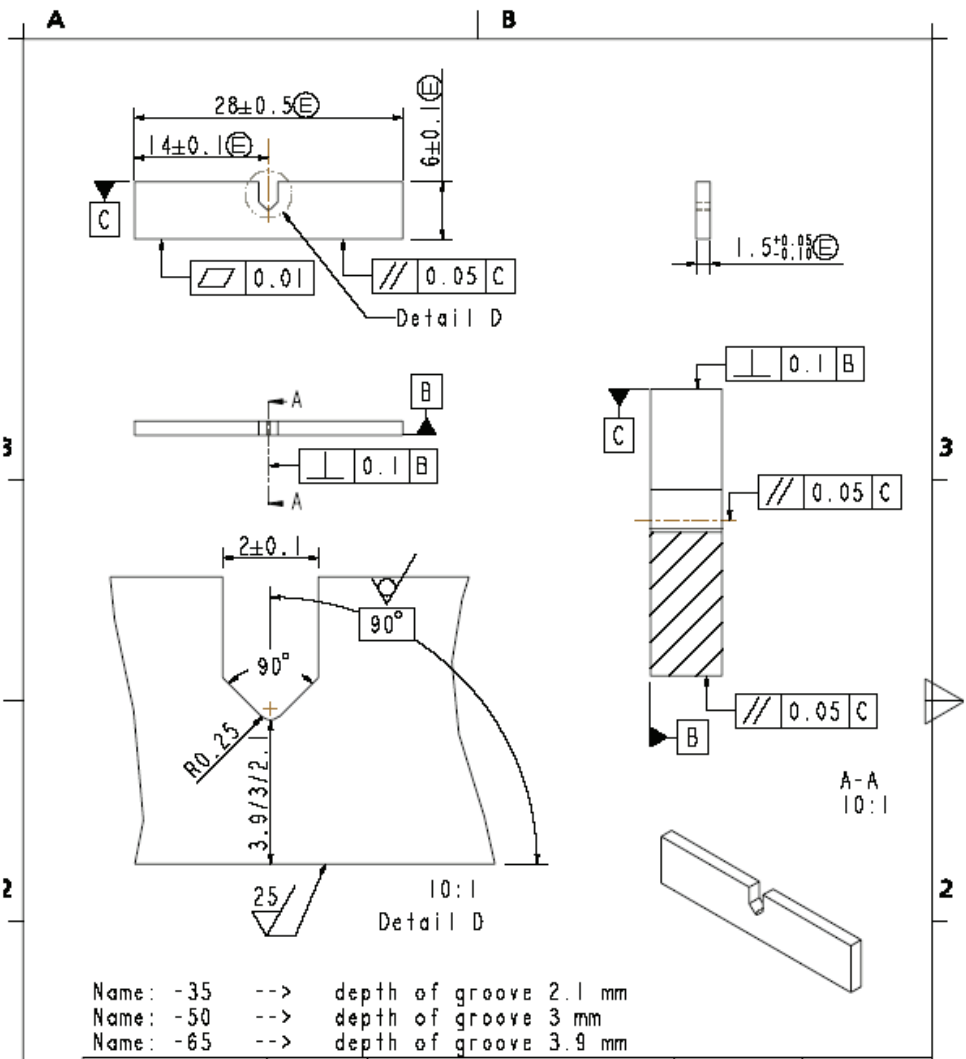
Name: -35 --> depth of groove 2.1 mm
Name: -50 --> depth of groove 3 mm
Name: -65 --> depth of groove 3.9 mm

A4

mm

2:1

23 degrees C, 50 % RH, conditioned

Plastic

09-Jul-07 JLLL

IDENTIFICATION   1/1

AXAX-XX

novo nordisk
Novo Nordisk A/S
Device R&D
Brennum Park
DK-3400 Hillerød
Tel.:+45 444448888

AXAX-XA

Fracture mechanical test specimen

AXAX-XX_NT1

131

11.3. Injection moulding tables

The injection moulding tables from the Impact & Indentation Study are shown in the following (tables from the Additives & Impact Study were not recorded electronically and were therefore unfortunately not available when this appendix was written).

INJECTION MOULDING TABLE – VS&VC

Operator:	*JLLL*	**Place:**	*NNAS DK HI 20H*	**Date and time:**	*2008-07-03 12:30*
Geometry/mould#:			*Test specimen /*		
Mould configuration:			*A1A1*		
Cavity#:		*N/A*	**Specimen numbers:**		

Machine data				
Manufacturer	*Husky*	Model	*S90 SR18/22*	
Internal machine ID	*SP 15*	Closing force [tonnes/kN]		*90 /*
Screw diameter [mm]	*18*	Conversion factor, hydr.-melt		*14.27*

Material data				
Generic type	*POM-C*	Manufacturer	*Ticona*	
Trade name and grade	*Hostaform C9021*	Lot no.	*0000287887*	
Masterbatch type and percentage	*-*			
Other additives and percentages	*None (nature)*			
Drying time and temperature	*-*			

Machine settings (nominal values unless otherwise stated)

Plastification phase – stage A and stage B		nozzle	zone 1	zone 2	zone 3	zone 4	hopper
cylinder temperatures [°C]		*200*	*200*	*195*	*185*	*175*	*50*
melt temperature, measured [°C]							
screw speed until pos. [rpm]	n_A	*212*		n_B		*180*	
position [mm]	s_A	*46*		s_B		*54*	
back pressure, specific [bar]	p_A	*40*		p_B		*40*	
decompr. before/after, [mm] @ [mm/s]		*- @ -*		*/*		*- @ -*	

Injection phase – stage A, B, C... (from right to left)								
max. spec. pressure [bar]	p_1	*1416*						
velocity profile [mm/s]	v_1	*4 / 13 / 12 / 11 / 9 / 8 / 7 / 5 / 4*						
profile positions (vel. until) [mm]	s_1	*4.2 / 48.7/ 50.6/ 51.4/ 51.9/ 52.4/ 52.8/ 53.2/ 54*						
switch over position [mm]	s_{so}	*3.0*						
fill time [s]	t_1	*4.67*						

Holding phase – stage A, B, C... (from right to left)							
spec. pressure profile [bar]	p_2	*800 / 925 / 1200 / / / / /*					
profile times (pres. duration) [s]	t_2	*4.0 / 0.10 / 0.05 / / / / /*					
cushion, measured [mm]	s_2	*4.8*					

Cooling phase	
cooling time, set value [s]	*6.5*
cooling time, realized [s]	

Mould tempering – positions as by mould drawing	inlet	manifold	nozzle 1	nozzle 2	nozzle 3	nozzle 4
hot runner temperatures [°C]	*200*	*200*	*200*			
mould tempering medium	*Water*					
inlet pressure of medium [bar]	*/ / / / / /*					
temperature, fixed/moving part [°C]	*25 / 25*					
mould temperature, measured [°C]	*/ / / / / /*					
Cycle time, measured [s]	*18.93*					

Notes	Kistler data file: *20080703_003*

INJECTION MOULDING TABLE – VS&W

Operator:	*JLLL*	Place:	*NNAS DK HI 20H*	Date and time:	*2008-07-03 10:40*
Geometry/mould#:			*Test specimen /*		
Mould configuration:			*A1A1*		
Cavity#:		*N/A*	Specimen numbers:		

Machine data

Manufacturer	*Husky*	Model	*S90 SR18/22*	
Internal machine ID	*SP 15*	Closing force [tonnes/kN]		*90 /*
Screw diameter [mm]	*18*	Conversion factor, hydr.-melt		*14.27*

Material data

Generic type	*POM-C*	Manufacturer	*Ticona*
Trade name and grade	*Hostaform C9021*	Lot no.	*0000287887*
Masterbatch type and percentage		*-*	
Other additives and percentages		*None (nature)*	
Drying time and temperature		*-*	

Machine settings (nominal values unless otherwise stated)

Plastification phase – stage A and stage B		nozzle	zone 1	zone 2	zone 3	zone 4	hopper
cylinder temperatures [°C]		*200*	*200*	*195*	*185*	*175*	*50*
melt temperature, measured [°C]							
screw speed until pos. [rpm]	n_A	*212*		n_B	*180*		
position [mm]	s_A	*46*		s_B	*54*		
back pressure, specific [bar]	p_A	*40*		p_B	*40*		
decompr. before/after, [mm] @ [mm/s]		*- @ -*		/	*- @ -*		

Injection phase – stage A, B, C... (from right to left)			
max. spec. pressure [bar]	p_1	*1027*	
velocity profile [mm/s]	v_1	*4 / 13 / 12 / 11 / 9 / 8 / 7 / 5 / 4*	
profile positions (vel. until) [mm]	s_1	*8.3 / 48.7/ 50.6/ 51.4/ 51.9/ 52.4/ 52.8/ 53.2/ 54*	
switch over position [mm]	s_{so}	*7.4*	
fill time [s]	t_1	*4.28*	

Holding phase – stage A, B, C... (from right to left)		
spec. pressure profile [bar]	p_2	*800 / 825 / 900 / / / / / /*
profile times (pres. duration) [s]	t_2	*8.0 / 0.10 / 0.05 / / / / / /*
cushion, measured [mm]	s_2	*4.9*

Cooling phase	
cooling time, set value [s]	*6.5*
cooling time, realized [s]	

Mould tempering – positions as by mould drawing	inlet	manifold	nozzle 1	nozzle 2	nozzle 3	nozzle 4
hot runner temperatures [°C]	*200*	*200*	*200*			
mould tempering medium		*Water*				
inlet pressure of medium [bar]	/	/	/ / / / /			
temperature, fixed/moving part [°C]		*90 / 90*				
mould temperature, measured [°C]		/ / / / / / /				

Cycle time, measured [s]	*22.54*

Notes   Kistler data file: *20080703_002*

INJECTION MOULDING TABLE – VF&VC

Operator:	JLLL	Place:	NNAS DK HI 20H	Date and time:		2008-07-03 13:00
Geometry/mould#:			Test specimen /			
Mould configuration:			A1A1			
Cavity#:		N/A	Specimen numbers:			

Machine data					
Manufacturer	Husky		Model	S90 SR18/22	
Internal machine ID	SP 15		Closing force [tonnes/kN]		90 /
Screw diameter [mm]	18		Conversion factor, hydr.-melt		14.27

Material data				
Generic type	POM-C		Manufacturer	Ticona
Trade name and grade	Hostaform C9021		Lot no.	0000287887
Masterbatch type and percentage		-		
Other additives and percentages		None (nature)		
Drying time and temperature		-		

Machine settings (nominal values unless otherwise stated)

Plastification phase – stage A and stage B		nozzle	zone 1	zone 2	zone 3	zone 4	hopper
cylinder temperatures [°C]		200	200	195	185	175	50
melt temperature, measured [°C]							
screw speed until pos. [rpm]	n_A	212		n_B		180	
position [mm]	s_A	46		s_B		54	
back pressure, specific [bar]	p_A	40		p_B		40	
decompr. before/after, [mm] @ [mm/s]		- @ -		/		- @ -	

Injection phase – stage A, B, C... (from right to left)							
max. spec. pressure [bar]	p_1	1838					
velocity profile [mm/s]	v_1	20 / 66 / 61 / 54 / 47 / 40 / 33 / 26 / 20					
profile positions (vel. until) [mm]	s_1	8.5 / 48.7 / 50.6 / 51.4 / 51.9 / 52.4 / 52.8 / 53.2 / 54					
switch over position [mm]	s_{so}	7.0					
fill time [s]	t_1	0.92					

Holding phase – stage A, B, C... (from right to left)							
spec. pressure profile [bar]	p_2	800 / 950 / 1400 / / / / /					
profile times (pres. duration) [s]	t_2	4.0 / 0.10 / 0.05 / / / / /					
cushion, measured [mm]	s_2						

Cooling phase	
cooling time, set value [s]	6.5
cooling time, realized [s]	

Mould tempering – positions as by mould drawing	inlet	manifold	nozzle 1	nozzle 2	nozzle 3	nozzle 4
hot runner temperatures [°C]	200	200	200			
mould tempering medium			Water			
inlet pressure of medium [bar]		/ / / / / / /				
temperature, fixed/moving part [°C]			90 / 90			
mould temperature, measured [°C]		/ / / / / / /				

Cycle time, measured [s]	15.17

Notes	Kistler data file: 20080703_004

INJECTION MOULDING TABLE – VF&W

Operator:	*JLLL*	Place:	*NNAS DK HI 20H*	Date and time:	*2008-07-03 10:30*
Geometry/mould#:			*Test specimen /*		
Mould configuration:			*A1A1*		
Cavity#:		*N/A*	Specimen numbers:		

Machine data				
Manufacturer	*Husky*		Model	*S90 SR18/22*
Internal machine ID	*SP 15*		Closing force [tonnes/kN]	*90 /*
Screw diameter [mm]	*18*		Conversion factor, hydr.-melt	*14.27*

Material data			
Generic type	*POM-C*	Manufacturer	*Ticona*
Trade name and grade	*Hostaform C9021*	Lot no.	*0000287887*
Masterbatch type and percentage	-		
Other additives and percentages	*None (nature)*		
Drying time and temperature	-		

Machine settings (nominal values unless otherwise stated)						
Plastification phase – stage A and stage B	nozzle	zone 1	zone 2	zone 3	zone 4	hopper
cylinder temperatures [°C]	*200*	*200*	*195*	*185*	*175*	*50*
melt temperature, measured [°C]						
screw speed until pos. [rpm]	n_A	*212*	n_B		*180*	
position [mm]	s_A	*46*	s_B		*54*	
back pressure, specific [bar]	p_A	*40*	p_B		*40*	
decompr. before/after, [mm] @ [mm/s]		- @ -		/	- @ -	
Injection phase – stage A, B, C... (from right to left)						
max. spec. pressure [bar]	p_1	*1738*				
velocity profile [mm/s]	v_1	*20 / 66 / 61 / 54 / 47 / 40 / 33 / 26 / 20*				
profile positions (vel. until) [mm]	s_1	*9.3 / 48.7/ 50.6/ 51.4/ 51.9/ 52.4/ 52.8/ 53.2/ 54*				
switch over position [mm]	s_{so}	*7.9*				
fill time [s]	t_1	*0.91*				
Holding phase – stage A, B, C... (from right to left)						
spec. pressure profile [bar]	p_2	*800 / 950 / 1400 / / / / /*				
profile times (pres. duration) [s]	t_2	*8.0 / 0.10 / 0.05 / / / / /*				
cushion, measured [mm]	s_2	*5.1*				
Cooling phase						
cooling time, set value [s]	*6.5*					
cooling time, realized [s]						
Mould tempering – positions as by mould drawing	inlet	manifold	nozzle 1	nozzle 2	nozzle 3	nozzle 4
hot runner temperatures [°C]	*200*	*200*	*200*			
mould tempering medium			*Water*			
inlet pressure of medium [bar]	/	/	/	/	/	/
temperature, fixed/moving part [°C]			*90 / 90*			
mould temperature, measured [°C]	/	/	/	/	/	/
Cycle time, measured [s]	*19.19*					

Notes   Kistler data file: *20080703_001*